Lead-free ferroelectric thin films elaborated by modified sol-gel routes

Claudette Mansour

THÈSE

Pour obtenir le grade de

DOCTEUR DE L'UNIVERSITE GRENOBLE ALPES

Spécialité : **PHYSIQUE DES MATERIAUX**

Arrêté ministériel : 25 mai 2016

Présentée par

Claudette MANSOUR

Thèse dirigée par **Christine REVENANT, Ingénieur-chercheur, CEA/IRIG/MEM/NRS** et
Encadrée par **Mohammed BENWADIH, Ingénieur-chercheur, CEA/LITEN/DTNM/LCO**

préparée au sein du **Laboratoire d'Innovation pour les Technologies des Energies Nouvelles (LITEN-CEA)**
dans **l'École Doctorale Physique**

Couches minces ferroélectriques sans plomb élaborées par des méthodes sol-gel modifiées

Lead-free ferroelectric thin films elaborated by modified sol-gel routes

Thèse soutenue publiquement le **18 mai 2021,**
devant le jury composé de :

Monsieur Philippe BELLEVILLE
Directeur de recherche, CEA le Ripault, Rapporteur
Monsieur Emmanuel DEFAY
Ingénieur-chercheur, LIST, Rapporteur
Monsieur Alain GIBAUD
Professeur émérite, Université de Maine, Examinateur
Madame Maryline GUILLOUX-VIRY
Professeur, Université de Rennes, Examinatrice
Monsieur Michel LANGLET
Directeur de recherche, LMGP, Examinateur
Monsieur Hubert RENEVIER
Professeur, Grenoble-INP, Président

Acknowledgments

First of all, i would like to give a special thank you to my supervisors Christine Revenant and Mohammed Benwadih for their amazing support throughout these three years of my PhD. It was a real pleasure to work with them, they were always there for me and taught me a lot of things. I gained so much experience in the workplace thanks to them.
I also would like to thank all the members of the LCO and LCH laboratories, including the laboratory head chiefs Audrey Martinent and Christophe Serbutoviez for their beautiful spirits, work ethics and hospitality. A heart warm thank you to my office colleague Laurent who has become a dear friend. It was a delight to share the office with you, thank you for the continuous support and for all the laughs and good times. I also would like to mention some of my colleagues that were especially dear to my heart, Lina, Jean-Marie, Sandra, Jamal, Helga, thank you for making this journey a fun one! I will miss our time together and the interesting conversations in the halls of C4!

Secondly, a big thank you to Olivier Poncelet, who helped me with chemistry related subjects. He was very insightful and an amazing chemist who had so many good ideas to share. I also would like to thank Stéphanie Pouget for her amazing skills in X-ray related matters, she was very helpful with the X-ray diffraction experiments. Also, a thank you to Anass Benayad for the XPS measurements that he conducted in this project, and for the help in analyzing the data. To all the staff on the BM02 beam line at ESRF, thank you for your time and immense help with the GISAXS experiments held in your facility.

Finally and most importantly, I thank my family, although they were far away, they never stopped supporting me and were always there for me, through the good times and the bad ones. Their constant encouragement got me through this challenging journey.
To my friends: Angela, Sarah, Maha, Gloria, Marleine, Rana, Lina, Carine, Christine (forgive me if i forgot anyone), thank you so very much, you are my second family. Thank you for all the splendid moments we spent together these past three years and for all the

support. I am very grateful to have you in my life.
To my special someone: Raed, you have witnessed the last phase of my PhD journey and let me tell you that i wouldn't have done it without you! You were my rock, my shoulder to cry on, my best friend and my sweetheart. Words cannot express how much i am thankful and grateful to have you in my life.

Contents

List of Abbreviations

BST	Barium strontium titanate
CSD	Chemical solution deposition
CVD	Chemical vapor deposition
FOM	Figure of merits
FWHM	Full width at half maximum
GBs	Grain boundaries
GISAXS	Grazing Incidence Small Angle X-ray Scattering
Iso	2-Isopropoxyethanol
MBE	Molecular beam epitaxy
MeOH	Methanol
MFM	Metal-Ferroelectric-Metal
MOD	Metal organic decomposition
NaCl	Sodium chloride
PLD	Pulsed laser deposition
PT	Lead titante
PTFE	Polytetrafluoroethylene
PVD	Physical vapor deposition
PZT	Lead zirconate titanate

RT	Room temperature
SBN	Strontium barium niobate
SCLC	Space-Charge Limited Conduction
TGA	Thermogravimetric analysis
TTB	Tetragonal tungsten bronze

Introduction générale

Les ferroélectriques ne sont pas de nouveaux matériaux, ils sont connus depuis le début du vingtième siècle. Avec le besoin actuel de miniaturisation, les couches minces ferroélectriques suscitent l'intérêt pour leurs diverses applications dans les appareils électroniques. Le développement des couches minces ferroélectriques a commencé à la fin des années soixante, l'intérêt de l'utilisation de ces couches a été déclenché par les progrès faits dans le domaine des dispositifs intégrés du Si pour les mémoires non volatils [1–3]. Au début des années quatre-vingt, la tentative de réalisation de mémoires ferroélectriques fonctionnelles a été bloquée par les difficultés rencontrées dans l'élaboration des matériaux ferroélectriques. Plus tard, l'intérêt pour ces matériaux a été ravivé grâce aux efforts et aux progrès réalisés dans les oxydes ferroélectriques. De nos jours, des couches minces ferroélectriques sont utilisés pour plusieurs applications, principalement dans les mémoires, les microsystèmes et les composants électriques à haute fréquence [4]. La Figure (1) montre les différents domaines d'application qui utilisent des films minces ferroélectriques.

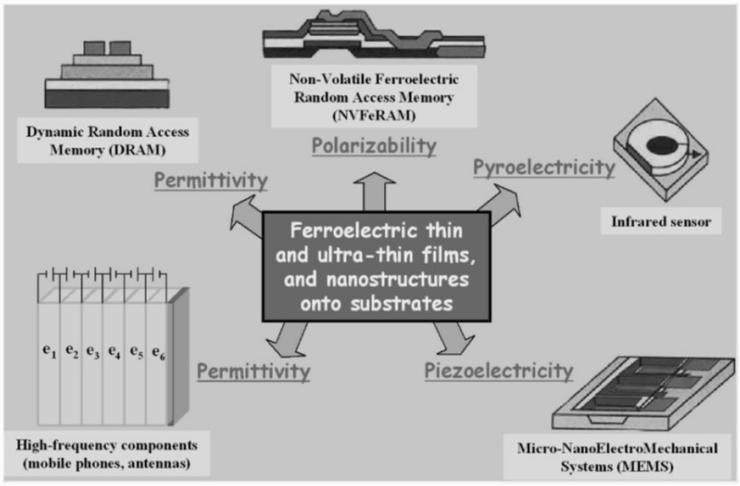

Figure 1: Les différentes applications des films minces ferroélectriques supportés sur des substrats. Le schéma est tiré de Pardo et al. [5].

Un grand nombre d'études ont été menées sur les matériaux ferroélectriques à base de plomb dans les dernières années. Ils restent les plus efficaces parmi les autres matériaux ferroélectriques connus.
Cependant, compte tenu de la toxicité du plomb et de ses composés, la législation adoptée par l'Union européenne limite l'utilisation de ces matériaux. Ainsi, est-il nécessaire de développer une recherche sur des matériaux sans plomb respectueux de l'environnement [6–8]. Parmi ces matériaux, le niobate de baryum strontium et le titanate de baryum strontium sont de bons candidats qui présentent des propriétés ferroélectriques et pyroélectriques exceptionnelles.
Les recherches sur les matériaux ferroélectriques en couche mince et leur traitement sont essentielles pour comprendre la physique qui régit le système et pour améliorer la fonctionnalité de ceux-ci. Ces dernières années, les processus basés sur des solutions ont intéressé le secteur industriel pour plusieurs raisons :

- La facilité de dépôt sur des substrats de formes et de tailles géométriques différentes.
- Le contrôle de la stoechiométrie du composé final jugé crucial pour la formation de phase dans les matériaux ferroélectriques.
- Le faible coût du processus à base de solution chimique et sa simplicité.

Objectif de la thèse

Dans cette thèse, nous nous intéressons à l'exploration de matériaux ferroélectriques sans plomb élaborés par des voies chimiques comme les méhodes de Metal Organic Decomposition (MOD) et du sol gel modifié. Le but est d'adresser une nouvelle génération des matériaux ferroélectriques plus performante en vue de les intégrer un jour sur un support flexible.
Les mécanismes derrière la formation des couches minces ne sont pas entièrement compris à ce jour. Il est de la plus haute importance de comprendre les mécanismes qui conduisent à la formation de films afin d'adapter la morphologie, la microstructure et les propriétés des films. Cette thèse se focalise sur:

- L'influence de la chimie des solutions sur la morphologie des couches minces.
- Les aspects physiques de la formation du film de l'état liquide jusqu'à l'état final du film.

- L'influence des paramètres de traitement tels que les conditions de dépôt et la température de recuit sur la micro- et nanostructure des couches minces.
- Les effets de dilution sur les propriétés ferroélectriques des couches minces.

Les trois années de thèse se sont déroulées au sein du Commissariat à l'Energie Atomique et aux Energies Alternative (CEA) à Grenoble, France. La thèse a été menée au Laboratoire des Composants Organiques (LCO) du Département des Technologies des Nouveaux Matériaux (DTNM) à l'institut du Laboratoire d'Innovation des Technologies pour les Energies Nouvelles (LITEN). La plateforme d'impression PICTIC du CEA LITEN est utilisée pour les travaux expérimentaux de la thèse. Cette plateforme est essentiellement dédiée aux technologies d'électronique flexible utilisant des encres liquides et des solutions telles que les polymères de polyfluorure de vinylidène (PVDF). Ce travail s'est déroulé en étroite collaboration avec l'équipe des Nanostructures et Rayonnement Synchrotron (NRS) au sein du laboratoire de Modélisation et Exploration des Matériaux (MEM) de l'Institut Interdisciplinaire de Recherche de Grenoble (IRIG).

Aperçu du manuscrit de la thèse

Le manuscrit de la thèse est divisé en 5 chapitres :

Le chapitre 1 comprend la bibliographie du phénomène et des matériaux ferroélectriques. Il comprend une approche théorique sur la ferroélectricité à travers des équations thermodynamiques décrivant le phénomène ferroélectrique. Des caractéristiques ferroélectriques importantes sont examinées tout au long du chapitre. Des matériaux ferroélectriques inorganiques sans plomb sont utilisés dans ce projet, notamment le titanate de baryum strontium. En particulier, le titanate de baryum strontium élaboré par voie chimique présente une grande richesse de morphologie et de nanostructure possibles.

Le chapitre 2 présente les méthodes utilisées dans l'élaboration et la caractérisation des films minces capacitifs. Le traitement des couches minces est discuté d'une manière complète tout au long du chapitre, de la synthèse de solution à la formation de condensateurs. Des difficultés technologiques telles que le mouillage, la fissuration du film et l'interdiffusion entre l'électrode métallique et le film sont rencontrés lors du traitement des films. Des solutions globales sont mises en place pour résoudre ces problèmes. Enfin, les différentes techniques utilisées pour étudier les propriétés morphologiques, structurelles et électriques sont présentées.

Le chapitre 3 explore la chimie des carboxylates pour la synthèse des couches minces diélectriques d'oxydes métalliques. Cette approche est simple et insensible à l'humidité, ce qui rend la synthèse de solution accessible sous air. L'objectif est de parvenir à une solution stable permettant de préparer des films minces fonctionnels. Le niobate de baryum strontium, un matériau ferroélectrique, est élaboré dans notre laboratoire par la voie des carboxylates. La formation des carbonates a présenté un vrai défi dans la formation des couches minces de niobate de baryum strontium. Une solution commerciale de titanate de baryum strontium (BST) à partir de précurseurs à base de carboxylates métalliques est choisi pour effectuer une étude appropriée de la formation de couches minces.

Le chapitre 4 dévoile les mécanismes régissant la formation de couches minces de BST à partir de l'état liquide au film final solide. Des études *in situ* et *ex situ* par rayons X sont menées pour suivre l'évolution morphologique des couches minces en fonction de la température. La formation de pores et de particules à des températures de recuit basses puis élevées sont discutées. Un modèle analytique décrivant la création de couches minces à l'échelle nanométrique est établi. Enfin, l'optimisation des conditions de dépôt et de recuit nous a permis de réaliser un condensateur ferroélectrique fonctionnel.

Le chapitre 5 étudie l'effet de dilution de solutions de précurseurs sur la morphologie et les propriétés électriques des couches minces BST. La nanostructure et la morphologie des films colonnaires évoluent avec le taux de dilution des solutions. L'évolution des tailles de grains et de la rugosité de surface est expliquée par le même modèle qu'au chapitre 4 basé sur les phénomènes de convection et de diffusion. Les effets de la dilution sur les propriétés diélectriques, la densité de courant et les propriétés ferroélectriques sont présentés.

General introduction

Ferroelectrics are not new materials by any stretch of imagination. They have been known since the early 20^{th} century. With the current trend of miniaturization, ferroelectric thin films arouse interest for their wide range of applications in electronic devices. The development of ferroelectric thin films started in the late sixties, the interest in using ferroelectric thin films was triggered by the progress in integrated Si devices for non volatile memories [1–3]. In the early eighties, the attempt to make practical ferroelectric memories was blocked by the difficulties encountered in the processing of the ferroelectric materials. Later on, the interest in those materials has been revived due to the efforts and advances made in ferroelectric oxide materials. Nowadays, ferroelectric films are used in several applications mainly in memories, microsystems and high frequency electrical components [4]. Fig. (1) summarizes the different application fields that utilizes ferroelectric thin films.

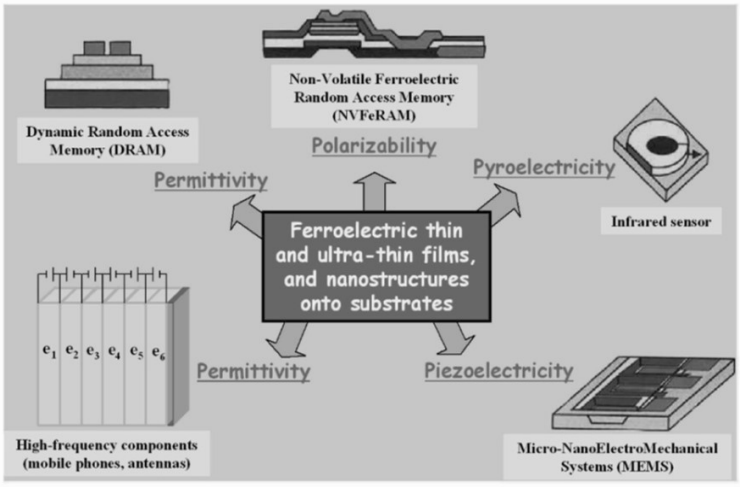

Figure 1: Applications of ferroelectrics supported onto substrates. Schematic taken from Pardo et al. [5].

A big amount of studies have been conducted on lead based ferroelectric materials in

the past years. They remain the most efficient among other known perovskite ferroelectric materials.
However, considering the toxicity of lead and its compounds, a legislation passed by the European Union limits the use of these materials. Hence, there is new research performed on environmental friendly lead-free material [6–8]. Among those materials, strontium barium niobate and barium strontium titanate are good candidates that show exceptional ferroelectric and pyroelectric properties.
Investigations on ferroelectric thin film materials and their processing are essential to understand the governing physics in the system and to enhance the functionality of those materials in different applications. In recent years, solution based processes have interested the industrial sector for a plethora of reasons:

- The ease of deposition on substrates with different geometrical shapes and sizes.
- The control of stoichiometry of the final compound that is deemed crucial for the phase formation in the ferroelectric materials.
- The cost effective processing of the solution based routes and its simplicity.

Aim of the thesis

In the current thesis project, we are interested in exploring lead-free ferroelectric materials processed by chemical routes such as Metal Organic Deposition (MOD) Metal Organic Deposition and modified sol gel techniques. The aim is to address a new generation of more efficient ferroelectric materials that could be integrated in the future on flexible substrates. The mechanisms lying behind thin film formation are not fully understood to this day. It is of utter importance to understand the governing mechanisms that drive the formation of films in order to tailor the morphology, the micro-, nanostructure and properties of the films. This is crucial for the assessment of thin films from a practical point of view. This thesis project will mainly focus on:

- The importance of solution chemistry on the morphology of thin films.
- The physical aspects of film formation from the liquid state up to the film state.
- The influence of the processing parameters such as deposition and annealing temperature on the nanostructure of thin films.
- The dilution effects on the ferroelectric properties of thin films.

The three years of thesis took place in the French Alternative Energies and Atomic Energy Commission or CEA research center in Grenoble, France. The thesis project was conducted at the Organic Composite Laboratory (LCO) in the Department of the Technologies of Novel Materials (DTNM) at the Laboratory of Innovation for the Technologies of the Novel Energies and the Nanomaterials (LITEN). PICTIC printing platform at CEA LITEN is used for the experimental work of the thesis. This platform is essentially dedicated for flexible elecronic technologies using liquid inks and solutions such as polyvinylidene fluoride (PVDF) polymers. This work was in close partnership with the Nanostructures and Synchrotron Radiation (NRS) team within the Modelling and Exploration of Materials (MEM) laboratory at the Interdisciplinary Research Institute of Grenoble (IRIG).

Thesis manuscript outline:

The thesis manuscript is divided into 5 chapters:

Chapter 1 consists of a state of the art of the ferroelectric phenomenon and ferroelectric materials. It includes a theoretical approach on ferroelectricity through thermodynamic equations describing the ferroelectric phenomenon. Important ferroelectric characteristics are considered throughout the chapter. Inorganic lead free ferroelectric materials are of interest in this project notably barium strontium titanate. In particular, chemical solution is a method of choice due to the possibility of tailoring the film morphology and nanostructure.

Chapter 2 introduces the methods used in the elaboration and characterization of thin film capacitors. The processing of thin films is discussed exhaustively throughout the chapter from solution synthesis to capacitor formation. Technological difficulties such as wetting, film cracking and metal electrode/film inter-diffusion are encountered during the processing of films and comprehensive strategies are put into place to solve them. At last, the different characterization techniques used to assess the morphological, structural and electrical properties are presented.

Chapter 3 explores the the carboxylate chemistry for dielectric metal oxides thin films synthesis. This approach is simple and moisture insensitive which makes solution synthesis accessible under air ambient atmosphere. The aim is to achieve a stable solution that allows us to prepare functional thin films. Strontium barium niobate, a promising

ferroelectric material, is elaborated in our laboratory using the carboxylate route. Several challenges are met, in particular, the formation of carbonates. A commercial solution of barium strontium titanate (BST) from metal carboxylate precursors is chosen to lead a proper study on thin film formation.

Chapter 4 unravels the mechanisms governing BST thin film formation from the liquid state to the final film. *In situ* and *ex situ* X-ray assisted studies on the morphology evolution of thin films as a function of temperature are conducted. Pore and particle formation at low and high annealing temperatures are discussed. An analytical model describing thin film formation at the nanoscale is established. Finally, optimization of the deposition and annealing conditions has led to a functional ferroelectric capacitor.

Chapter 5 investigates the precursor solution dilution effect on the morphological and electrical properties of BST thin films. The nanostructure of the columnar films evolved with dilution increase. Grain size and surface roughness evolution are explained by the same model as in chapter 4 based on convection and diffusion phenomena. Dilution effects on the dielectric, current density and ferroelectric properties are presented.

References

[1] Francombe, M. *Thin Solid Films* **13**(2), 413–433 (1972).

[2] Chapman, D. *Journal of applied physics* **40**(6), 2381–2385 (1969).

[3] Sharma, B., Vogel, S., and Prentky, P. *Ferroelectrics* **5**(1), 69–75 (1973).

[4] Setter, N., Damjanovic, D., Eng, L., Fox, G., Gevorgian, S., Hong, S., Kingon, A., Kohlstedt, H., Park, N. Y., Stephenson, G. B., Stolitchnov, I., Taganstev, A. K., Taylor, D. V., Yamada, T., and Streiffer, S. *Journal of Applied Physics* **100**(5), 051606 (2006).

[5] Pardo, L. and Ricote, J., editors. *Multifunctional polycrystalline ferroelectric materials: processing and properties*. Number 140. (2011).

[6] Panda, P. K. *Journal of Materials Science* **44**(19), 5049–5062 (2009).

[7] Kumari, P. *Advanced Materials Letters* **6**(6), 453–484 (2015).

[8] Shrout, T. R. and Zhang, S. J. *Journal of Electroceramics* **19**(1), 113–126 (2007).

Chapter 1

Ferroelectricity versus structure

1.1 Historical background

Pyroelectricity is one of the oldest properties of solid materials. It is defined as the temperature dependence of spontaneous polarization or electric dipole moment in certain materials. Pyroelectricity was first observed by the greek philosopher Theophrastus in 315 BC, and then the interest in pyroelectricity re-emerged in Europe in the nineteenth century [1, 2]. The first known pyroelectric crystals showed no ferroelectricity, i.e. the absence of switchable polarization in the presence of an applied electric field. The history of ferroelectricity began in the middle of the 17^{th} century when a french chemist Elie Seignette created the "sel polychreste" known today as the Rochelle salt. After nearly 250 years, Joseph Valasek discovered the dielectric properties of the salt leading to the concept of ferroelectricity [3]. Valasek observed a peculiar dielectric behavior in the Rochelle salt, it resembles ferromagnetism in that there was a hysteresis effect in the field-polarization curve. One of the greatest breakthroughs was the discovery of ferroelectricity in $BaTiO_3$ (1945) [4] which became the most investigated ferroelectric material with a perovskite structure ABO_3. It was only logical to proceed with the research on materials with perovskite structure with the oxygen octahedral building blocks BO_6 at the origin of ferroelectricity. Hence, came the discovery of new ferroelectric materials such as $KNbO_3$ and $KTaO_3$ (1949), $LiNbO_3$ and $LiTaO_3$ (1949), $PbTiO_3$ (1950) [5].

1.2 Classification of materials

The symmetry of materials whether it is a crystal, a thin film, or a polycrystalline, affects its properties. Based on symmetry elements of crystals, there are 230 space groups, divided into 32 point groups, which are subdivisions of 7 crystal systems (triclinic, monoclinic, orthorhombic, tetragonal, rhombohedral, hexagonal, and cubic). Among these 32 crystal classes, 11 are centrosymmetric containing an inversion center, that do not exhibit any polar properties. The remaining 21 noncentrosymmetric point groups have polar properties with the exception of the cubic point group 432. These 20 point groups are often called piezoelectric point groups. Piezoelectricity results from the coupling of mechanical stress and electrical energy in the material. Among these piezoelectric point groups, 10 groups have a unique polar axis and may exhibit a spontaneous polarization vector P_S in the absence of an external electric field, this is referred to as the pyroelectric effect. Pyroelectric crystalline materials belong to 10 polar point groups: 1, 2, m, 2mm, 4, 4mm, 3, 3m, 6, and 6mm. On the other hand, polycrystalline and ceramics materials can't be described by the same discrete symmetry elements as crystals. It is more complex to describe the orientation of grains within a ceramic material, their structures belong to a textural or basic point groups. In this case, the symmetry axis is of an infinite order with an ∞ symbol, meaning that the material can be rotated by any angle around this infinity axis without changing its properties. Ceramics with randomly oriented grains have a spherical symmetry $\infty\infty$m which is centrosymmetric and does not exhibit any piezoelectric effects even if each grain orientation belongs to a polar point group. If the ceramic is ferroelectric, the polarization of each grain can be oriented by an external electric field in the direction of the field. The polarized ceramic possesses a cone symmetry ∞m displaying both piezoelectric and pyroelectric effects[6–8].

Fig. 1.1 shows a general representation of dielectric materials classification. Ferroelectrics form a subgroup of pyroelectrics that are a subgroup of piezoelectrics. The main characteristic of a ferroelectric material is having a spontaneous polarization that can be reversed by an applied electric field.
In summation, the symmetry of the materials plays an important role in defining their properties; ferroelectrics are a subclass of pyroelectrics and piezoelecrics. They are an important class of materials that exhibit better pyroelectric and piezoelectric properties than nonferroelectrics.

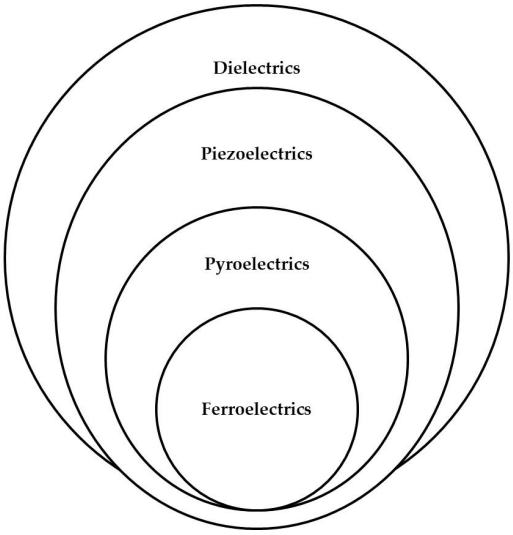

Figure 1.1: Diagram of dielectric material classes

1.3 Theory of ferroelectricity

An introduction is given on the important parameters used to describe the ferroelectricity phenomenon. The theoretical approach is described using thermodynamic concepts, which are the building blocks for the theory of thermodynamics in ferroelectrics. Moreover, the ferroelectric phenomenon is described with specific details on the phase transitions in ferroelectric materials and a main focus on the second-order(continuous) phase transition.

1.3.1 Important parameters

Let us introduce some important dielectric parameters that are going to be used in the thermodynamic relations later on in this section [6, 7].

Dipole moment

A dipole moment is a measure of the separation of two opposite electrical charges in a molecule or an atom. The magnitude of the dipole moment vector μ is equal to the

electric charge q multiplied by the distance d between the charges and the direction is from negative charge to positive charge.

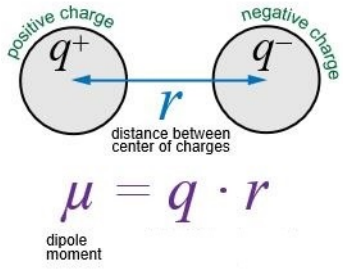

Figure 1.2: Electric dipole moment

Electric Polarization

In polar dielectric materials, dipole moments are present in molecules or atoms because the centers of positive and negative charges do not coincide. The summation of these electric dipole moments per unit volume of the material gives the electric polarization $\boldsymbol{P}$.

$$\boldsymbol{P} = \frac{\sum_{i}^{n} \mu}{V} \tag{1.1}$$

where V is the volume of the material.

Electric displacement and dielectric constant

Upon the application of an external electric field on the dielectric material, the expression of the polarization $\boldsymbol{P_i}$ induced in the insulating material by an electric field vector $\boldsymbol{E_j}$ is given by:

$$\boldsymbol{P_i} = \chi_{ij} \boldsymbol{E_j} \tag{1.2}$$

χ_{ij} is the dielectric susceptibility of the material.
The electric displacement $\boldsymbol{D}$ developed inside the material due to the application of the electric field E is written as follows:

$$\boldsymbol{D_i} = \varepsilon_0 \boldsymbol{E_i} + \boldsymbol{P_i} \tag{1.3}$$

ϵ_0 = 8.854$\times 10^{-12}$ F.m^{-1} is the permittivity of free space, another expression of $\boldsymbol{D}$ can be written using Eq.(1.2) and (1.3):

$$\boldsymbol{D_i} = \varepsilon_0 \boldsymbol{E_i} + \chi_{ij} \boldsymbol{E_j} = \varepsilon_{ij} \boldsymbol{E_j} \tag{1.4}$$

where ε_{ij} = ε_0 δ_{ij} + χ_{ij} is the dielectric permittivity of the material with

δ_{ij}= $\begin{cases} 1, \text{if i=j} \\ 0, \text{if i} \neq \text{j} \end{cases}$ $\varepsilon_0\ \delta_{ij} << \chi_{ij}$ in most ferroelectric materials so $\varepsilon_{ij} \approx \chi_{ij}$.

The relative dielectric permittivity ζ_{ij}, also known as the dielectric constant of the material is more often used than the dielectric permittivity.

$$\zeta_{ij} = \varepsilon_{ij}/\varepsilon_0 \tag{1.5}$$

The dielectric permittivity ε_{ij} and the relative dielectric permittivity ζ_{ij} are second rank tensors.

1.3.2 Thermodynamic approach

The coupling of the thermal, elastic and electrical effects is introduced using the thermodynamic approach to define the pyroelectric and ferroelectric effects. Let us assume that the thermal, elastic and dielectric behavior of a homogeneous dielectric material can be described by six parameters: temperature *T*, entropy *S*, stress *X*, strain *x*, electric field *E* and electric displacement *D*.
According to the first and second laws of thermodynamics, assuming that the change in the internal energy *U* of a dielectric is reversible, d*U* is given by Eq.(1.6) as:

$$dU = TdS + Xdx + EdD \tag{1.6}$$

In most experimental situations, the temperature *T*, stress *X* and electric field *E* are most likely to be manipulated. For that reason, it is more convenient to switch the independent

variables[1] from *(S,x,D)* to *(T,X,E)*. This change in the set of variables will affect the thermodynamic potential of the internal energy *U*, by adding the terms *-TS - Xx -ED* to *U*. A new thermodynamic potential is defined as :

$$G = U - TS - Xx - ED \tag{1.7}$$

It is known as the Gibbs free energy , the differential form of *G* together with the Eq.(1.6) gives the following:

$$dG = -SdT - xdX - DdE \tag{1.8}$$

From Eq.(1.8) we can obtain the following terms:

$$S = -\left(\frac{\partial G}{\partial T}\right)_{X,E} \qquad x = -\left(\frac{\partial G}{\partial X}\right)_{T,E} \qquad D = -\left(\frac{\partial G}{\partial E}\right)_{T,X} \tag{1.9}$$

The differential form of these equations can be written as:

$$dS = \left(\frac{\partial S}{\partial T}\right)_{X,E} dT + \left(\frac{\partial S}{\partial X}\right)_{T,E} dX + \left(\frac{\partial S}{\partial E}\right)_{T,X} dE \tag{1.10}$$

$$dx = \left(\frac{\partial x}{\partial T}\right)_{X,E} dT + \left(\frac{\partial x}{\partial X}\right)_{T,E} dX + \left(\frac{\partial x}{\partial E}\right)_{T,X} dE \tag{1.11}$$

$$dD = \left(\frac{\partial D}{\partial T}\right)_{X,E} dT + \left(\frac{\partial D}{\partial X}\right)_{T,E} dX + \left(\frac{\partial D}{\partial E}\right)_{T,X} dE \tag{1.12}$$

The coefficients in the equations (1.10) to (1.12) have physical interpretation for the different coupled effects. We can note the most important coefficients, those relating strain *x* to stress *X* (elastic compliance), strain *x* to electric field *E* (piezoelectric coefficient), electric displacement *D* to temperature *T* (pyroelectric coefficient), electric displacement *D* to electric field *E* (dielectric constant or permittivity) and strain *x* to temperature *T* (thermal expansion coefficient).

[1] variables related to the bulk properties of the material unlike dependent variables which take into account the material properties and dimensions.

1.3.3 Ferroelectric phenomenon

Ferroelectrics are dielectrics which are polar materials that posses a spontaneous polarization vector P_S, existing inherently in the material without the application of an external electric field. The distinct characteristic of a ferroelectric material is the ability of the P_S to switch between at least two equilibrium orientations in the presence of an applied electric field. These materials go through a structural phase transition from a high temperature phase (paraelectric non-polar phase) to a lower temperature phase (ferroelectric polar phase). Phase transitions are based on the change of the symmetry inside the material, for example, the most common transition is from cubic to tetragonal symmetry. The transition temperature is called the Curie temperature T_C. Fig.(1.3) (a) shows how the dielectric permittivity drops above T_C. It follows the Curie-Weiss law:

$$\varepsilon = \varepsilon_0 + \frac{C}{T - T_C}. \tag{1.13}$$

C is the Curie constant.
The phase transitions could be of the first or second order, the order is determined by the discontinuity in the partial derivatives of the Gibbs free energy of the ferroelectric. First order transitions are discontinuous, while second order transitions are continuous. In the case of ferroelectric phase transitions, the independent parameters are often chosen to be *(D, X, T)* and by choosing this set, the corresponding free energy is the elastic Gibbs energy G_1, which can be obtained like the Gibbs free energy from the internal energy *U* (see section 1.3.2). The detailed thermodynamic calculations are found elsewhere [5, 6].

Ferroelectric domains

In an ideal ferroelectric crystal, it is assumed that the spontaneous polarization is uniformly aligned throughout the entire crystal along the same direction. However, this is not true for real ferroelectrics, where imperfections and inhomogeneities are present in the structure, thus near those defects, the spontaneous polarization may differ from the perfect crystal. The start of spontaneous polarization at the transition temperature leads to surface charges which in their turn, create an electric field called the depolarization field E_D. The depolarizing fields arise from the nonhomogeneous distribution of spontaneous polarization in the crystals (grains in ceramics and thin films) oppositely to the direction of the $\boldsymbol{P_S}$. The energy associated with that field is given by:

$$W_E = \frac{1}{2}\int_V \boldsymbol{D}.\boldsymbol{E}\, dV. \tag{1.14}$$

When cooling from the paraelectric phase to the ferroelectric phase, different regions with uniformly oriented spontaneous polarization in different directions form. These regions are known as ferroelectric domains. They form in order to minimize the electrostatic energy *W* of the depolarizing field and the elastic energy attached to the mechanical constraints to which the ferroelectric material is subjected to during the phase transition. The boundaries separating domains are referred to as domain walls associated with a domain wall energy W_w depending on the domain geometry, if the domains have oppositely oriented polarization, the separation is called 180° walls and those who separate domains with mutually perpendicular polarization are called 90° walls as shown in Fig.(1.3) (b).

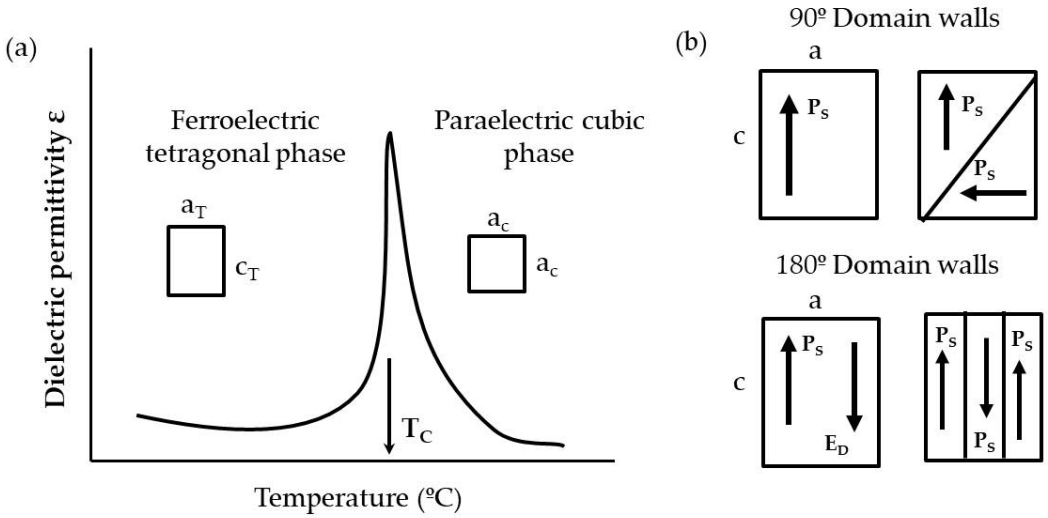

Figure 1.3: Illustration of (a): Ferroelectric- paraelectric phase transition from tetragonal to cubic symmetry and (b): 90° and 180° domain walls formation in a ferroelectric material with tetragonal symmetry.

The geometry of the domain is affected by several factors including crystal symmetry, defects, the magnitude of mechanical stress, dielectric and elastic compliances, in addition to sample preparation and geometry. If the width of a domain approaches the thickness of a domain wall, ferroelectricity may cease to exist because it is no longer possible to compensate the depolarizing field in the crystal.
In summation, the ferroelectric splits into domains to minimize the electrostatic energy associated with the depolarizing field, also it occurs due to mechanical stresses. The energy of domain walls can alter the ability of the ferroelectric domains to minimize the

depolarizing energy due to domain width [5, 6].

Polarization reversal

The most distinguished characteristic of ferroelectrics is that the spontaneous polarization can be reversed with an applied electric field. A ferroelectric hysteresis loop will occur when the domains of the ferroelectric material switch. Fig.(1.4) shows a typical ferroelectric hysteresis loop. At low electric field, polarization switching does not occur, the field is not strong enough to reorient the domains, thus the ferroelectric behaves like an ordinary dielectric. As the electric field increases, the polarization increases in a non-linear fashion with a curvature. Once all the domains are aligned, the polarization reaches a saturation point. Some domains start to back switch when the electric field is decreased and the value of the polarization at zero field is called the remanent polarization P_r. The field necessary to bring the polarization to zero is called the coercive field E_c. The spontaneous polarization is equal to the saturation value of the polarization extrapolated to zero field as shown in Fig.(1.4).
The coercive field, spontaneous and remanent polarization and shape of the loop can be affected by many factors including the film thickness, the presence of charged defects, mechanical stresses, preparation conditions and thermal treatment.

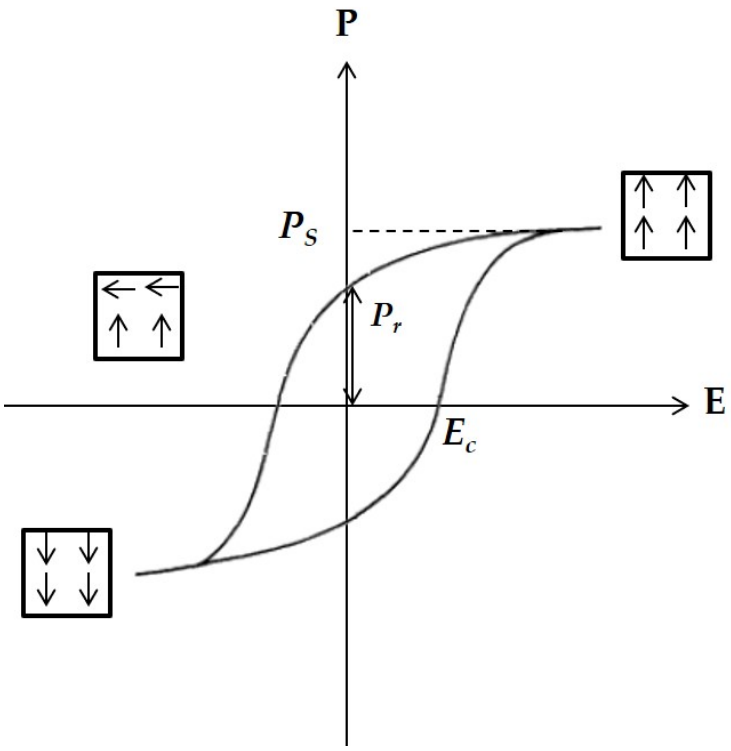

Figure 1.4: Polarization-field *P-E* hysteresis loop of a ferroelectric material.

Charge-voltage response in true ferroelectrics

As mentioned previously, the *P-E* loop is a plot of the charge or polarization as a function of the electric field *E* at a certain frequency. The charge and polarization responses are assumed to be equal for high relative permittivity materials. The understanding of the *P-E* measurement significance is made easier with some linear devices examples. For an ideal capacitor, the curve is a straight line whose gradient is proportional to the capacitance (Fig.5.26 (a)). This is because the current leads the voltage by 90°, hence, the charge in an ideal capacitor is in phase with the voltage. In the case of an ideal resistor, the current and voltage are in phase and so the *P-E* loop becomes a circle. Fig.5.26 (b) shows the circular *P-E* loop with the center at the origin. When combining these two components in parallel, a lossy capacitor (Fig.5.26 (c)) is obtained where the area within the loop is proportional to the loss tangent of the device, and the slope proportional to the capacitance. Loss can be due to dielectric hysteresis or leakage current or both. Fig.5.26 (d) shows the *P-E* loop of a true non-linear ferroelectric. These loops are usually centered around zero and for both the lossy capacitor and the ferroelectric they cross the y axis at a non-zero value. In the ferroelectric case, this crossing point provided a measure of the remnant

polarization. For the lossy capacitor the non-zero crossing point does not indicate any remanence. Caution must be exercised in interpreting the crossing point on the charge (polarization) axis as ferroelectric remanence, particularly where there may be leakage currents or the ferroelectric behavior is not clearly established. There are many examples where lossy dielectric loops have been incorrectly presented as evidence of ferroelectric behavior [9–11].

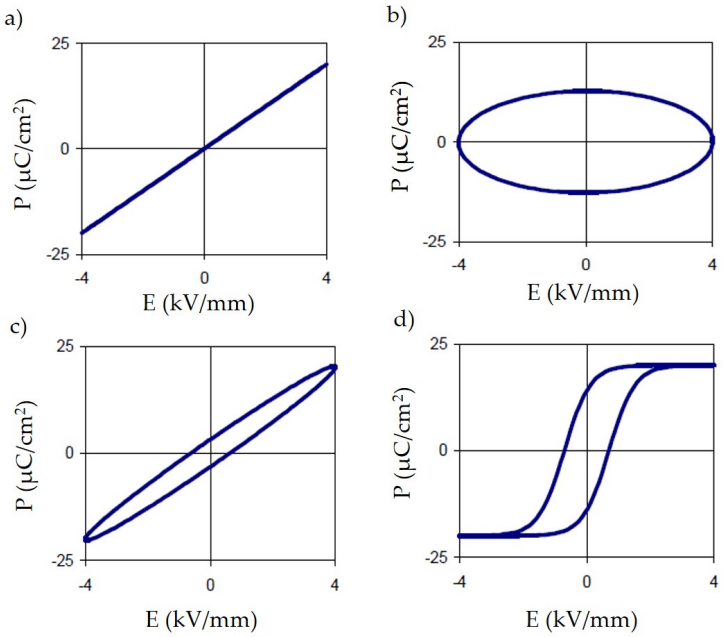

Figure 1.5: Schematic *P-E* response (in arbitrary units) of (a) linear capacitor, (b) linear resistor, (c) lossy capacitor and (d) non-linear ferroelectric.

Dielectric breakdown mechanisms

There are three basic mechanisms by which an insulating material breaks down under the application of an electric field : intrinsic breakdown, thermal breakdown and discharge breakdown. During real breakdown, all of these may occur in combination and, perhaps in the case of sintered ceramics, will be dominated by residual porosity or surface asperities, rather than characteristic properties of the bulk material. Porosity has been shown to be the key factor to initiate breakdown in most common ceramics. The dependence of the size and thickness can be explained by the fact that the electric field has a smaller chance of finding a critical defect at which breakdown may be initiated in thinner material. The mechanism by which the material then breaks down is open to debate but may include the idea of the propagation of a charge 'streamer' (in a similar manner to

that described for lightening) progressing from pore to pore via conventional conduction routes. The permittivity of the sample has been shown to play a role in the breakdown phenomenon, but this has not been satisfactorily developed. Breakdown may be caused by longer term effects such as gradual reduction in resisitivity at a continuous applied high stress, as well as environmental effects such as moisture, temperature, electrochemical reactions between electrodes and the material, and structural effects such as sharp and point discontinuities which might have the effect of amplifying the electric stress in certain regions. Field emission injection of electrons from the electrodes can cause avalanche ionisation and subsequent breakdown [12, 13]. Other causes of breakdown can be related to the presence of carbonate species and organic residue from the precursor solution such as Na^+, Cl^-, F^- and OH^-. Those species act like mobile ions which can also be the origin of leakage current. Intrinsic defects, microscopic cracks, metallic impurities and dust particle on the surface of the thin film samples can also lead to electrical breakdown.

Poling of ferroelectrics

Ferroelectric grains in ceramics and polycrystalline films split into multiple domains and that is due to the mechanical and electrical boundary conditions at each grain. In polycrystalline ferroelectric materials, the spontaneous polarization is often randomly distributed resulting in zero net polarization. Therefore, the material may not exhibit pyroelectric or piezoelectric properties. These materials can be brought to a polar state by applying a strong electric field usually at elevated temperatures. The process is called poling, it is a electrical treatment that can orient the domains in the grains in the direction of the electric field. Kohli et al [14] studied the effects of hot poling and pulse cycling on the configuration of domains in (111) and (110) oriented PZT 15/85 thin films. Domain pinning due to field cycling at low ac fields was observed, while depinning of domains occurs at high ac fields. These phenomena are compatible with a migration of defects to the interface due to hot poling, and a redistribution of domain walls and defects throughout the volume during field cycling.
Poling is a complicated process and there is not a singular rule that applies to all ferroelectric materials. In fact, it depends on several factors such as the symmetry of the ferroelectric, the domains orientation, defects present in the material and the nature of the electrodes.

1.4 Ferroelectric materials

In recent years, ferroelectric materials have been of great interest due to their unique properties that render them useful for many modern applications. There are various families of materials that exhibit ferroelectric properties having different structures and characteristics. In the following section, some of the important materials are considered.

1.4.1 Single crystals

Triglycine Sulfate (TGS) crystal family is a well known ferroelectric material usually used in single crystal form for infrared pyroelectric detectors. The crystals are usually grown by the temperature lowering or solution evaporation methods. The crystal has a monoclinic symmetry below curie temperature (T_C = 49 °C). The single crystals of TGS provide the highest voltage response but due to difficulties with water solubility and humidity, their applications are limited and they cannot be used in single element detectors. Some modifications to the basic crystal structure of TGS can enhance their performance, for example, doping with cations such as Lithium (Li), zinc (Zn) and copper (Cu), in addition to substituting the glycine group with L-alanine that can introduce an internal bias field to give poled LaTGS crystals with stabilized spontaneous polarization. This is because of the additional ethyl group in alanine molecules that prevent the rotation of the molecules inside the lattice which results in poled single-domain crystal. Other single crystal materials may include Lithium tantalate ($LiTaO_3$) and lithium niobate ($LiNbO_3$) that are usually grown from Czochralski method. $LiTaO_3$ has low losses, hence a favorable F_D so it is suited for single element detectors. In addition, strontium barium niobate $Sr_xBa_{1-x}NbO_6$ single crystals are also fabricated by the Czochralski method. Although single crystal-type materials are promising candidates for pyroelectric applications, they are limited by the expensive growth techniques and the difficulty of managing to obtain big size products [15, 16].

1.4.2 Polymers

Polyvinylidene fluoride (PVDF) based ferroelectric polymers and its copolymers are known as piezoelectric polymers. They exhibit pyroelectric properties, although the pyroelectric coefficient and figure of merits (FOM) [2] are lower than other materials particularly oxides, because of their high dielectric loss [17].
Gupta et al.[18] reviewed the nature and origin of pyroelectricity in PVDF, its copolymer vinylidene fluoride-trifluoroethylene (VDF-TrFE) and their composites (polymer-ceramic). The polymer-ceramic composites have attracted much attention due to the enhancement of the ferroelectricity in such system [19–21].
The commercial availability of these polymer materials in thin sections (down to micrometers), makes them attractive for low cost detectors. In addition, the fact that they have low permittivities render them best suited for large area detectors rather than the small area detectors required for thermal imaging [22].

1.4.3 Ceramics

Ceramics play an important role in pyrolelectric applications, they can offer numerous advantages over other crystalline materials such as relatively cheap manufacturing on large areas using metal oxides processes such as sol gel, electrical reliability, robust mechanical and chemical properties. They posses high Curie temperature, making them functional at high temperatures. It is also possible to modify ceramic properties by introducing dopants to control certain parameters such as dielectric constant and loss, the curie temperature T_C and the mechanical properties [22].
Most ceramics have a perovskite structure with a general formula of ABO_3, which is a large family of oxygen octahedral ferroelectrics. Further details about this particular structure is given in later sections. Ceramic materials such as lead titanate (PT)[15], $PbZr_{1-x}Ti_xO_3$ (PZT) [23, 24], barium titanate $BaTiO_3$ [16, 25] and barium strontium titanate (**BST**) [26, 27] are considered the most common perovskite ceramics.
Many attempts have been made to stabilize and modify the material properties of lead based ceramics by introducing dopants such as Mn , Niobium Nb [28], rare earths, Ca and La [15].
Similarly for $BaTiO_3$ based ceramics which present low pyroelectric coefficient at room

[2] Figures of merit (**FOMs**) are considered an important criteria to asses the material performance

temperature (RT) ion substitutions have been made to enhance their pyroelectric performances. The most effective ion substitutions are Ca^{+2}, Sr^{+2} in A site and Zr^{+4} in B site [16].

1.4.4 Thin films

Thin film properties differ from bulk materials in their microstructure as well as the substrate effects on thin films. These effects are mainly the growth phenomena on the surface of the bottom electrode, the strain induced by the bulk substrate in the cooling process of the deposition and the thermal expansion mismatch between the thin film and the substrate. In addition, the nucleation and texture of the thin films are also influenced by the chemical nature, the lattice and microstructure of the substrate. Hence, the growth of the pyroelectric materials in thin film form is very complex since it depends in a major part on the underlying substrate[29].
On the other hand, thin films are technologically desirable in order to avoid complex processing of bulk materials. The processing of bulk materials is exhaustive and expensive, and it is more convenient to directly deposit the material in thin film form onto a substrate [30]. There are many deposition techniques employed for ferroelectric thin film fabrication such as chemical solution deposition (CSD) particularly sol-gel routes or metal organic deposition (MOD), sputtering, ion beam deposition and pulsed laser deposition (PLD) [31, 32]. The main challenge is to achieve similar properties as for bulk ceramics and even enhance the FOMs. One example is epitaxial PT thin films that showed a higher FOM than their ceramic counterpart [33]. Lead-based materials are up to now the favourable choice for pyroelectric thin films, and the most advanced work on silicon substrate is achieved with PZT films with Zr ratio ranging from 15 to 30 % [29].

1.4.5 Applications

Ferroelectric materials, especially polycrystalline ceramics, are very promising for a variety of applications such as:

- High permittivity capacitors.

- Ferroelectric memories.
- Pyroelectric sensors.
- Piezoelectric and electrostrictive transducers.
- Electrooptic devices.

For capacitor dielectrics, the peak dielectric constant around T_C is utilized, while for memory applications, the material must be ferroelectric at RT. A large temperature dependence of the spontaneous polarization below T_C is sought for pyroelectric sensors. The converse pyroelectric effect is the electrocaloric effect (electric field generates the temperature decrease), which is becoming a hot research topic in this energy-saving age. Piezoelectric materials are used as sensors and actuators, where the T_C should be much above RT. Pressure and acceleration sensors are now commercially available in addition to conventional piezo-vibrators. Precision positioners and pulse drive linear motors have already been installed in precision lathe machines, semiconductor manufacturing apparatuses, and office equipment. Recently, enthusiastic development is found in ultrasonic motors, aiming at electromagnetic, noise-free, and very compact motor applications. In parallel to the new energy source programs, piezoelectric energy harvesting systems have become popular. Waste mechanical energy such as noise vibration, wind, and human walking can be converted into electrical energy and can be used directly for signal transmission or to charge up batteries for portable electronics. Electro-optic materials will become key components in displays and optical communication systems in the future [34–36].

1.5 Lead free thin film materials

Although lead-based materials show exceptional performances in piezoelectric and pyroelectric applications, the utilization of lead-free materials is of arising interest nowadays due to the hazardous lead-containing substances and the environmental concerns of their toxicity. Hence, the development of lead-free materials has become inevitable [16, 37–39].

1.5.1 Barium strontium titanate thin films

1.5.1.1 Perovskite structure

Barium strontium titanate (BST) has a perovskite type structure. The general formula of a perovskite is ABX_3 where A and B are cations and X is an anion, in most cases, X is an oxygen O. The A cations reside on the corner of the unit cell, while B cations sit in the center and anions occupy the face-center sites of the cube. In the case of BST, Ba and Sr occupy the A sites, Ti the B-sites and O the face-center of the cubic unit cell (Fig. 1.6). The ideal cubic structure has B cations in 6-fold coordination surrounded by an octahedron of anions (BO_6) and the A cations sit in a 12-fold coordinate sites [40].

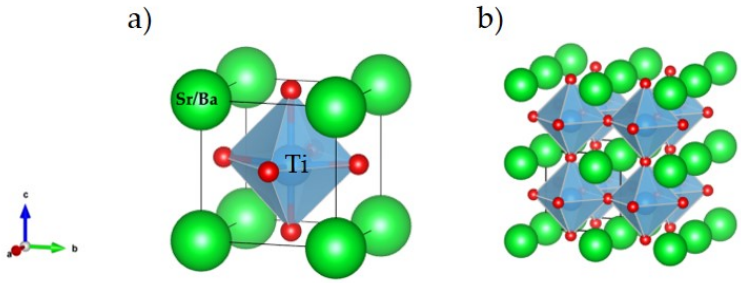

Figure 1.6: Scheme showing the perovskite structure of cubic $Ba_xSr_{1-x}TiO_3$. (a) one unit cell (b) global view of several unit cells.

Perovskite oxides are an important class of ferroelectrics with properties that are attractive to technological applications. This is due to a feature of the perovskite structure, the linear chains made of corner-shared $(BO_6)_n$ octahedra that occur in all three dimensions. In Barium titanate based materials such as BST, TiO_6 local bonding units are the origin of the polarity in the material. The possible movement of Ti in this configuration is depicted Fig.(1.7).

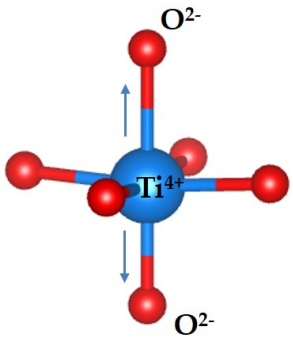

Figure 1.7: Ti atom movement in the TiO_6 octahedra.

Frenkel et al.[41] have found that in quasi-amorphous $BaTiO_3$, the TiO_6 octahedra is distorted and the Ti-off center displacement occurs in the [111] direction of the TiO_6 octahedra.

1.5.1.2 Composition dependent T_C

The phase transition temperature of barium strontium titanate $Ba_xSr_{1-x}TiO_3$ with $0 \leq x \leq 1$ depends on the Sr content. T_C can be tailored by varying the Sr concentration [42–45]. The ferroelectric to paraelectric transition temperature, marked by the peak in dielectric permittivity, varies by changing the Ba/Sr ratio from 0 to 1 in temperature interval from 0 to 390 K. Changes in the dielectric behavior and lattice parameters of BST films have been reported with x values [46]. Compositions in the paraelectric phase ($x \leq 0.5$) exhibit high dielectric tunability and low dielectric losses at microwave frequencies [47–51]. The composition $Ba_{0.7}Sr_{0.3}TiO_3$ with a T_C at RT is ferroelectric and exhibits a high technological interest due to its high permittivity k at RT. This composition has applications in high k capacitors [52–54].

1.5.1.3 Microstructure of CSD processed BST thin films

According to [54, 55], the microstructure of BST thin films can be tailored by adjusting the CSD parameters such as the precursor solution chemistry, heat treatments and solution concentration. For instance, the decomposition behavior of the precursors will determine the phase formation in the thin films. The different heat treatments play a role

in defining the grain morphology and orientation in the films. If a single step annealing is adapted (crystallization after each deposited layer), the morphology and the orientation of the grains will depend on the solution concentration. When lowering the solution concentration, the morphology changed from a grainy structure to columnar grained and induced more oriented grains [56, 57]. In addition, the microstructure has a major influence on the properties of the thin films. For example, Hoffmann et al. [55, 58] studied the temperature dependence of the dielectric permittivity for different morphologies of CSD processed BST (fine grained, grainy and columnar) with the same thickness. The dielectric values increased when the morphology evolved from grainy to columnar grained.

1.5.2 Strontium barium niobate

1.5.2.1 Structure and Curie temperature

Strontium barium niobate $Sr_xBa_{1-x}Nb_2O_6$ (SBN) crystallizes in the region $0.25 < x < 0.75$ with the tetragonal tungsten bronze (TTB) structure presented in Fig. (1.8). Five NbO_6 octahedra are arranged on a circle providing three types of interstitial sites: trigonal sites are vacant, tetragonal (A1) and pentagonal (A2) sites are partially occupied (5/6) by the divalent Sr and Ba atoms, and partially vacant (1/6) for reasons of electroneutrality [59, 60].

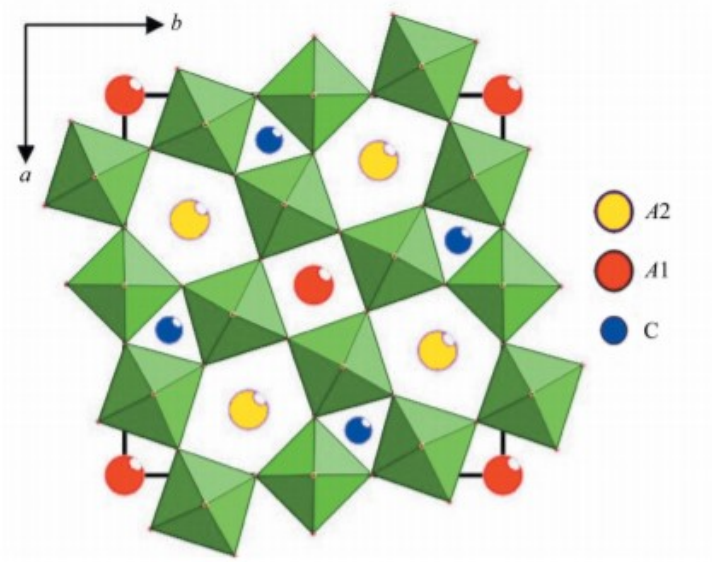

Figure 1.8: c-axis view of the strontium barium niobate tetragonal tungsten bronze structure (TTB). A1 and A2 sites are partially occupied by Sr and Ba atoms respectively (5/6) and partially vacant (1/6). The structure is taken from [61].

The dimensions of the cell decrease with Sr content increase due to the smaller radius of Sr atoms. The variation in lattice parameters and chemical composition alters the T_C of the ferroelectric crystal, which decreases with the increasing Sr/Ba ratio [62].
Ferroelectric, dielectric and optical properties of SBN are very sensitive to Sr/Ba ratio change. With the increasing Sr content, the pyroelectric coefficient is enhanced [63].

1.5.2.2 Dielectric properties of SBN thin films

Glass et al. [63] investigated the dielectric properties of SBN crystals as functions of temperature, frequency, dc electric field and Sr content. The first paper on the ferroelectric properties of SBN thin films was reported by Antsigin et al. [64], they found similar properties as for SBN crystals. Since that time, several papers have been published about the dielectric properties of SBN thin films that were prepared by different techniques. The results varied from one report to another. In the work of Glass, the dielectric permittivity deduced from the capacitance of a crystalline SBN disk sandwiched between two electrodes varied strongly depending on the nature of the electrodes, the thickness of the sample and its degree of polarity. In thin film measurements, the effect of interfaces on the measured dielectric permittivity is enhanced. This is most likely, one of the reasons for the scattering of reported results. The second reason resides in the method used to record

a Polarization-Electric field *(P-E)* hysteresis loop, which integrates the current intensity induced by voltage variation in the circuit. The dielectric loss current is also integrated and may contribute to form the observed hysteresis loop [60].

1.6 Conclusion

In this chapter, a concise representation of the history and phenomenology of ferroelectricity was presented. A brief theoretical and thermodynamic approach on the ferroelectric phenomenon was introduced which included important ferroelectric characteristics such as polarization reversal among others. The mechanisms involved in the electrical breakdown of dielectrics that will influence the poling process were discussed. In addition, the variety of ferroelectric materials were presented in this chapter, with emphasis on lead free inorganic thin film materials such as BST and SBN thin films.
The content of the following chapters will focus on the study of chemical solution derived SBN and BST thin films. The methods employed for the elaboration of the thin films and the influence of the processing conditions on the properties of the thin films are represented.

References

[1] Lang, S. B. *Ferroelectrics* **7**(1), 231–234 (1974).

[2] Lang, S. B. *Physics Today* **58**(8), 31–36 (2005).

[3] Busch, G. *Ferroelectrics* **74**(1), 267–284 (1987).

[4] Wul, B. *Nature* **157**(3998), 808–808 (1946).

[5] Lines, M. E. and Glass, A. M. *Principles and applications of ferroelectrics and related materials*. (2001).

[6] Damjanovic, D. *Reports on Progress in Physics* **61**(9), 1267–1324 (1998).

[7] Batra, A. K. and Aggarwal, M. D. *Pyroelectric materials: infrared detectors, particle accelerators and energy harvesters*. (2013).

[8] Whatmore, R. In *Springer Handbook of Electronic and Photonic Materials,* Kasap, S. and Capper, P., editors, Springer Handbooks, 1–1. Cham (2017).

[9] In *Piezoelectric Ceramics,* JAFFE, B., COOK, W. R., and JAFFE, H., editors, iii. (1971).

[10] Hall, D., Cain, M., Stewart, M., National Physical Lab., T. U. K. C. f. M. M., and Technology;. In *Minutes of the NPL CAM7 IAG Meeting*, (1998).

[11] Scott, J. F. *Journal of Physics: Condensed Matter* **20**(2), 021001 (2007).

[12] Wolak, M. A., Pan, M.-J., Wan, A., Shirk, J. S., Mackey, M., Hiltner, A., Baer, E., and Flandin, L. *Applied Physics Letters* **92**(11), 113301 (2008).

[13] Zheng, D., Swingler, J., and Weaver, P. *Sensors and Actuators A: Physical* **158**(1), 106–111 (2010).

[14] Kohli, M. and Muralt, P. *Ferroelectrics* **225**(1), 155–162 (1999).

[15] Aggarwal, M., Batra, A., Guggilla, P., Edwards, M., Penn, B., and Currie Jr, J. (2010).

[16] He, H., Lu, X., Hanc, E., Chen, C., Zhang, H., and Lu, L. *Journal of Materials Chemistry C* **8**(5), 1494–1516 (2020).

[17] Whatmore, R. W., Osbond, P. C., and Shorrocks, N. M. *Ferroelectrics* **76**(1), 351–367 (1987).

[18] Das-gupta, D. K. *Ferroelectrics* **118**(1), 165–189 (1991).

[19] Dash, S., Choudhary, R. N. P., and Goswami, M. N. *Journal of Alloys and Compounds* **715**, 29–36 (2017).

[20] Pradhan, S. K., Kumar, A., Sinha, A. N., Kour, P., Pandey, R., Kumar, P., and Kar, M. *Ferroelectrics* **516**(1), 18–27 (2017).

[21] Dietze, M. and Es-Souni, M. *Functional Composites and Structures* **1**(3), 035005 (2019).

[22] Whatmore, R. W. *Ferroelectrics* **118**(1), 241–259 (1991).

[23] King, T., Preston, M., Murphy, B., and Cannell, D. *Precision Engineering* **12**(3), 131–136 (1990).

[24] Panda, P. K. and Sahoo, B. *Ferroelectrics* **474**(1), 128–143 (2015).

[25] Lang, S. B., Rice, L. H., and Shaw, S. A. *Journal of Applied Physics* **40**(11), 4335–4340 (1969).

[26] Yoo, J., Gao, W., and Yoon, K. *Journal of materials science* **34**(21), 5361–5369 (1999).

[27] Mao, C., Cao, S., Yan, S., Yao, C., Cao, F., Wang, G., Dong, X., Hu, X., and Yang, C. *Applied Physics Letters* **102**(24), 242911 (2013).

[28] Shaw, C., Gupta, S., Stringfellow, S., Navarro, A., Alcock, J., and Whatmore, R. *Journal of the European Ceramic Society* **22**(13), 2123–2132 (2002).

[29] Muralt, P. *Journal of Micromechanics and Microengineering* **10**(2), 136–146 (2000).

[30] Whatmore, R. W. *Journal of Electroceramics* **13**(1-3), 139–147 (2004).

[31] Auciello, O., Kingon, A., and Krupanidhi, S. *MRS Bulletin* **21**(6), 25–30 (1996).

[32] Tuttle, B. and Schwartz, R. *MRS Bulletin* **21**(6), 49–54 (1996).

[33] Iijima, K., Tomita, Y., Takayama, R., and Ueda, I. *Journal of Applied Physics* **60**(1), 361–367 (1986).

[34] Uchino, K. *Piezoelectric Actuators and Ultrasonic Motors*. (1996).

[35] Martin, L. W. and Rappe, A. M. *Nature Reviews Materials* **2**(2), 16087 (2016).

[36] Uchino, K. *Ferroelectric devices*. CRC press, (2018).

[37] Shrout, T. R. and Zhang, S. J. *Journal of Electroceramics* **19**(1), 113–126 (2007).

[38] Takenaka, T. and Nagata, H. *Journal of the European Ceramic Society* **25**(12), 2693–2700 (2005).

[39] Damjanovic, D., Klein, N., Li, J., and Porokhonskyy, V. *Functional Materials Letters* **03**(01), 5–13 (2010).

[40] Saal, J., Andelm, J., Nothwang, W. D., and Cole, M. W. *Integrated Ferroelectrics* **101**(1), 142–151 (2008).

[41] Frenkel, A. I., Feldman, Y., Lyahovitskaya, V., Wachtel, E., and Lubomirsky, I. *Physical Review B* **71**(2), 024116 (2005).

[42] Zhou, L., Vilarinho, P., and Baptista, J. *Journal of the European Ceramic Society* **19**(11), 2015–2020 (1999).

[43] Liu, G., Wolfman, J., Autret-Lambert, C., Sakai, J., Roger, S., Gervais, M., and Gervais, F. *Journal of Applied Physics* **108**(11), 114108 (2010).

[44] Qiu, J., Liu, G., Sakai, J., Gervais, F., and Wolfman, J. *Journal of Applied Physics* **110**(6), 064114 (2011).

[45] Adikary, S. U. and Chan, H. L. W. *Journal of Materials Science* **39**(21), 6523–6528 (2004).

[46] Lin, Y., Lee, J.-S., Wang, H., Li, Y., Foltyn, S. R., Jia, Q. X., Collis, G. E., Burrell, A. K., and McCleskey, T. M. *Applied Physics Letters* **85**(21), 5007–5009 (2004).

[47] Lancaster, M. J., Powell, J., and Porch, A. *Superconductor Science and Technology* **11**(11), 1323–1334 (1998).

[48] Bao, P., Jackson, T. J., Wang, X., and Lancaster, M. J. *Journal of Physics D: Applied Physics* **41**(6), 063001 (2008).

[49] Tagantsev, A., Sherman, V., Astafiev, K., Venkatesh, J., and Setter, N. *Journal of Electroceramics* **11**(1/2), 5–66 (2003).

[50] Zhu, X., Zhu, J., Zhou, S., Liu, Z., Ming, N., Lu, S., Chan, H. L.-W., and Choy, C.-L. *Journal of Electronic Materials* **32**(10), 1125–1134 (2003).

[51] Pecnik, T., Glinek, S., Kmet, B., and Malic, B. *Revue Roumaine de Chimie* **63**(5-6), 393–400 (2018).

[52] O'neill, D., Catalan, G., Porras, F., Bowman, R., and Gregg, J. *Journal of Materials Science: Materials in Electronics* **9**(3), 199–205 (1998).

[53] Tseng, T.-Y. *Ferroelectrics* **232**(1), 1–13 (1999).

[54] Schneller, T., Waser, R., Kosec, M., and Payne, D., editors. *Chemical Solution Deposition of Functional Oxide Thin Films*. Vienna, (2013).

[55] Hoffmann, S. and Waser, R. *Journal of the European Ceramic Society* **19**(6-7), 1339–1343 (1999).

[56] Hoffmann, S., Hasenkox, U., Waser, R., Jia, C. L., and Urban, K. *MRS Proceedings* **474**, 9 (1997).

[57] Jia, C. L., Urban, K., Hoffmann, S., and Waser, R. *Journal of Materials Research* **13**(8), 2206–2217 (1998).

[58] Hoffmann, S. and Waser, R. *Le Journal de Physique IV* **8**(PR9), Pr9–221 (1998).

[59] Jamieson, P. B., Abrahams, S. C., and Bernstein, J. L. *The Journal of Chemical Physics* **48**(11), 5048–5057 (1968).

[60] Cuniot-Ponsard, M. In *Ferroelectrics - Material Aspects,* Lallart, M., editor. (2011).

[61] Podlozhenov, S., Graetsch, H. A., Schneider, J., Ulex, M., Wöhlecke, M., and Betzler, K. *Acta Crystallographica Section B Structural Science* **62**(6), 960–965 (2006).

[62] Ballman, A. A. and Brown, H. *Journal of Crystal Growth* **1**(5), 311–314 (1967).

[63] Glass, A. M. *Journal of Applied Physics* **40**(12), 4699–4713 (1969).

[64] Antsigin, V., Egorov, V., Kostsov, E., Malinovsky, V., and Sterelyukhina, L. *Ferroelectrics* **63**(1), 235–242 (1985).

Chapter 2

Thin film capacitor elaboration and characterization methods

2.1 Introduction

The second chapter of this thesis aims to discuss the different aspects of thin film capacitor elaboration and characterization. It is divided into three main sections: the first one is dedicated to describe the elaboration of the thin films.
In particular, chemical solution deposition methods, the processing of the perovskite thin films and the experimental work done on the formation of inorganic thin films are covered. In the second section, the technological aspects of a functional thin film capacitor are presented. Then, the last section covers the different characterization techniques employed to study the morphology, structure and electrical properties of the thin films.

2.2 Elaboration of thin films

The use of thin films has been known for a long period of time by mankind since the first tin glazed coating for decoration [1]. Nowadays, thin films are becoming very essential to various areas of research and technology, in many fields of studies and applications. In the following section, various thin film deposition methods are discussed with an emphasis on the chemical solution derived techniques for inorganic thin film elaboration.

2.2.1 Thin film deposition methods

The need to elaborate good quality thin films is skyrocketing. The deposition process of thin films is very important in order to get high quality thin films that demonstrate durability, functionality and sustainability. The deposition processes allow the control of the microstructure, the physical and structural properties of the films.
Physical and chemical deposition methods are two major techniques that are used for the elaboration of thin films.

- **Physical deposition techniques:**

They are also called physical vapour deposition (PVD) methods since they involve direct deposition from the vapour phase. Physical deposition methods are mainly based on vacuum evaporation at high vacuum (HV) or ultra high vaccum (UHV). The physical deposition techniques can be divided into sections: (i) evaporation techniques that include methods like vacuum evaporation (VE), molecular beam epitaxy (MBE) and pulsed laser deposition (PLD) ; (ii) sputtering techniques including direct current sputtering (DC sputtering) and radio frequency sputtering (RF sputtering) [2]. These techniques require very specific conditions and are held under controlled atmospheres to obtain high quality thin films. Although physical deposition methods are very effective and yield good quality thin films, they can be very costly [1].

- **Chemical solution deposition (CSD) :**

CSD methods have attracted the attention of many companies interested in the development of functional thin films. Thus, this method became the fabrication method of choice when cost considerations predominate. The most common chemical solution deposition techniques include the sol-gel route, chemical vapor deposition (CVD) , electrodeposition, etc. The fabrication of the thin films by this approach consists of the following steps [3]:

- Synthesis of the precursor solution by a chemical route.
- Deposition of the final solution by spin-coating or dip coating.
- Heat treatment at low temperature for drying and pyrolysis of organic species.
- Thermal annealing at higher temperatures for densification and crystallization of the films into the desired oxide phase.

In this work, we are interested in the preparation of perovskite metal oxide thin films using chemical approaches. Among the potential routes, sol gel and Metal organic decomposition (MOD) methods are employed in the elaboration of ferroelectric perovskite metal oxides.

2.2.2 Sol gel based method

Sol gel processing is one of the well established approaches among CSD processes to prepare oxide thin films. It has potential control over the textural and surface properties of the materials. One of the most technologically important aspects of sol gel processing is that compared to conventional thin film formation processes such as CVD, evaporation or sputtering, sol-gel requires less equipment and is potentially less expensive. With this method, one can precisely control the microstructure of the deposited films such as the pore size, pore volume and surface area [4]. It also allows solution deposition on larger scales and even on flexible substrates.
A sol is a colloidal suspension of solid particles in a liquid. This sol can be used to generate many forms of materials including organic and inorganic metal oxides. In the processing of perovskite films, the solvent, 2-methoxyethanol($CH_3OCH_2CH_2OH$), has been greatly used. There are several metal compounds that can be used as starting reagents, typically metal alkoxides $M(OR)_x$, where M is a metal and R is an alkyl group. The routes using 2-methoxyethanol are considered sol-gel processes because the key reactions leading to the formation of the precursor species are hydrolysis and condensation of the alkoxide reagent, in which metal-oxide-metal (M-O-M) bonds are created [5, 6].
With metal alkoxides, the reactions are:

Hydrolysis:

$$M(OR)_x + H_2O \rightarrow M(OR)_{x-1}\,(OH) + ROH$$

Condensation:

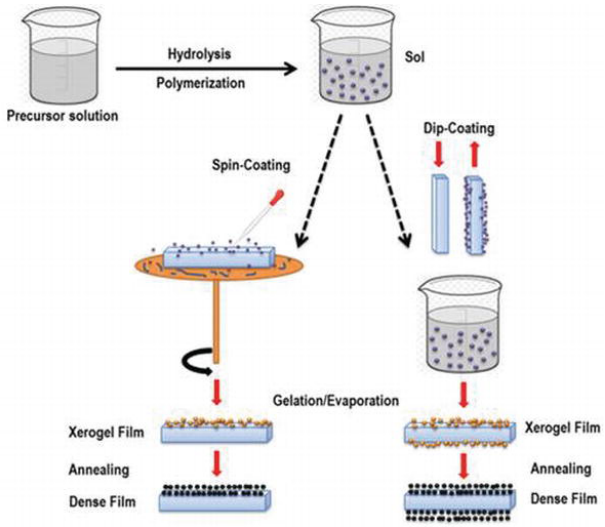

Figure 2.1: Scheme of Sol gel process from Mahmood et al.[8].

alcohol elimination:

$$2M(OR)_{x-1}(OH) \rightarrow M_2O(OR)_{2x-3}(OH) + ROH$$

water elimination:

$$2M(OR)_{x-1}(OH) \rightarrow M_2O(OR)_{2x-2} + H_2O$$

Initially, the corresponding metal precursor goes through rapid hydrolysis to produce the metal hydroxide solution as shown in the reaction above, followed by immediate condensation which leads to the formation of M-O-M bonds. The final compound is usually a xerogel depending on the drying conditions as depicted in Fig.(2.1).
Metal alkoxides are immensely used in the formation of perovskite metal oxides, but due to their polar M-O bond, non-stabilized alkoxides are very sensitive toward hydrolysis and if hydrolysis is extensive, precipitation of hydroxide or oxide/hydroxide species may occur.

2.2.3 MOD method

MOD utilizes carboxylate routes that do not undergo important condensation reactions during solution preparation or film deposition. Metal carboxylates are salts of carboxylic acids (R-COOH), R represents an alkyl group such as methyl CH_3, for example,

CH_3 COOH is the acetic acid and acetate is the salt. These carboxylates are chemically stable against water and oxygen, and in the ferroelectric thin films processing, they are used as precursors for the lower valent ionic cations including Pb^{+2}, Ba^{+2} and Sr^{+2} [7]. The MOD approach is straightforward, it basically consists of dissolving the metallo-organic compounds usually carboxylates in a common solvent and blending the solutions to obtain the desired stoichiometry. The starting compounds are water insensitive, hence, the precursor species existing in the solution maintain a resemblance to the starting molecules. Combining this aspect with the use of non-interacting solvents allows characterizing the solution as a simple mixture of the starting compounds. This route has been used for various ferroelectirc materials, as well as for the preparation of perovskite films suitable for magnetoresistive applications and for high-temperature superconductors [3, 5].

2.2.3.1 Solution coating techniques

Solutions are usually deposited by spin or dip coating techniques. Brinker et al. and Scriven et al.[9–11] described in detail the dip coating process. In this section, spin coating is presented in more details since it was used in this work.
Bornside et al.[12] divide the spin coating process into four stages: **deposition, spin up, spin off and evaporation**. The fourth stage may occur during the other three stages unless there are precautions to delay the evaporation. Fig.(5.22) illustrates the four stages of the spin batch process.
In the first stage, Fig.(5.22) (a), an excess of liquid solution is deposited onto the substrate using mostly pipettes. The amount of liquid is far more than the required coating to be produced. Fig.(5.22)(b) depicts the spin up stage when the rotating speed progressively increases. The liquid flows radially in an outward motion due to the centrifugal forces that drives this movement. In the third stage, Fig.(5.22) (c), the liquid now covers the entire substrate and flows radially to the perimeter when the substrate is rotating at a full speed of several thousand revolutions per minute (rpm). Edge effects are often observed because the fluid flows uniformly outward. Droplets are formed at the edge to be flung off. In the final stage, Fig.(5.22) (d), evaporation takes over completely and becomes the primary mechanism of thinning of the coating.
The advantage of the spin coating is that the film thickness tends to become uniform during spin-off. The key to the uniformity of the thickness is the balance between the two

governing forces: the rotation-induced centrifugal force, which drives radially outward flow and the resisting viscous force, which acts radially inward retaining the film on the flat substrate. The thickness of an uniformly thick film during spin-off is described by [11]:

$$h(t) = \frac{h_0}{\sqrt{1 + 4\,\rho\,\omega^2\,h_0^2\,t\,/3\,\nu}} \tag{2.1}$$

here h_0 is the initial thickness, t is the time, ω is the angular velocity, ρ the fluid density, and ν the total viscosity. According to Scriven et al. [11], in most cases, the films tend to become uniform in the spin-off stage regardless of its profile when it was deposited. The spinning process creates a stable forced convection in the vapor above the substrate that causes the mass transfer coefficient k to be uniform [13]. Thus, making the evaporation rate uniform as well. A spun film arrives at his final thickness by evaporation after the film becomes so thin that his flow stops.

For a Newtonian fluid, Emslie et al.[14] showed that the governing phenomena for the uniformity of the fluid is the centrifugal force. Using computations, they calculated the time needed to obtain a uniform film with a given thickness at a given angular velocity and viscosity. Later on, Meyerhofer et al.[15] presented a model showing that the thickness of a film prepared by spin coating is dependent on the spin speed v, the initial viscosity ν_0 and the evaporation rate e. The final thickness of the film can be expressed as:

$$h_f \propto (\frac{\nu_0\,e}{v^2})^{1/3} \tag{2.2}$$

The work of Bornside et al. [12] and Sahu et al.[16] also contributed in modeling the spin coating process.

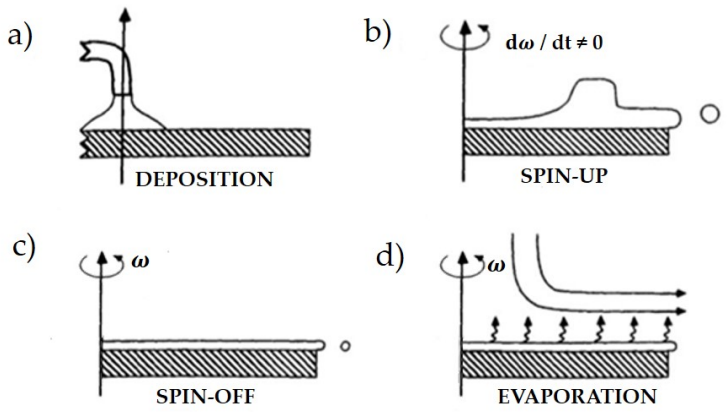

Figure 2.2: Stages of spin coating process adapted from Bornside et al. [12].

2.2.4 Processing of solution based perovskite thin films

The spike of interest in the fabrication of perovskite thin films has risen due to their attractive properties in various application fields. The chemical solution deposited perovskite thin films have been particularly studied in the past twenty to thirty years [17, 18]. The lead containing materials such as lead zirconate titanate (PZT) are very well documented. Schwartz et al.[19] examined the different aspects that influence the elaboration of solution derived perovskite thin films. The microstructure of perovskite thin films usually depends on the substrate nature, the solution chemistry, and the thermal processing.

2.2.4.1 Solution chemistry effects

Schwartz [3] discussed the effects of precursor chemistry on the decomposition pathway. Three main routes were investigated for the precursor preparation that include sol-gel, chelate and metal organic deposition (MOD) synthesis processes. The PZT system has been extensively studied for those three routes [20–22]. These studies focused on the decomposition behavior of the precursor for the MOD, sol gel and chelate routes. The pyrolysis conditions leading to homogeneous amorphous phases that are necessary for obtaining good crystalline films were discussed. Besides from the solution chemistry,

ambient atmosphere used during pyrolysis and crystallization can affect not only residual carbon content in the films but also the nature of intermediate phases. Heating rate and pyrolysis temperature have also an impact. Many techniques can be used to study the decomposition behavior such as fourier-transform infrared spectroscopy (FTIR), thermogravimetric analysis (TGA) and differential thermal analysis (DTA).

2.2.4.2 Heat treatment

For CSD fabricated thin films, thermal annealing used for crystallization has a major impact on the properties of the films. The conventional thermal annealing is commonly used for the formation of ferroelectric perovskite thin films, it allows crystallization at high temperatures (700-800°C) in an adapted furnace with a slow heating rate for several hours. The conventional heating yields a homogeneous crystallization in the bulk of in the film. The main inconveniences of this method is the long exposure times of the samples to high temperatures that could cause interdiffusion between the substrate and the film causing the formation of detrimental dead layers at the interfaces. In addition, undesired intermediate phases (pyrochlore, fluorite) can form using this type of annealing [3, 23].

Thermal annealing approaches

In CSD, two approaches for thermal processing of thin films are given : ***the single step process*** and ***the two-step process*** [3, 23].
The first approach consists of directly annealing the thin films at high temperatures, without going through an intermediate step at lower temperatures. This process, is usually performed using rapid thermal annealing (RTA), enhances the densification of the films by delaying the onset of the crystallization [27].
The second approach and the most utilized one is the two-step annealing process. In this method, the as-deposited thin film goes through a pyrolysis step before the crystallization at higher temperatures. The thin films are basically placed on a hot plate at temperatures ranging from 200°C to 400°C for a couple of minutes in order to remove organic species. In general, this is considered as the prefered approach for thin film thermal processing as it lowers the chance of cracking and blistering of the films. This also allows the transition from amorphous to quasi-amorphous films prior to the crystallization at higher temperatures reaching 700-800°C.

2.2.5 Technological process of thin film formation

This section is an overview on the fabrication environement of the films and an exploration of the equipments used during the process of thin film preparation. The exact experimental details for the preparation of the inorganic thin films will be given in the following chapters for the materials used.

2.2.5.1 Equipments and materials

The solution preparation and thin film deposition is conducted in a clean room environment to avoid any contamination from dust particles in the air. Such contamination can lead to the degradation of the films by dust streaks. The spin coater used to deposit the solutions is the SUSS MicroTec RC 8, operating under an extraction system. This system can eliminate any odors or toxic vapours emanating from the sol-gel chemical solutions. The spin coater scheme is displayed in appendix A.1. The annealing of the deposited thin films is performed using a hot plate under a hood in the clean room (see appendix A.2).
The substrate chosen for the deposition of the thin films was $Pt/TiO_2/SiO_2/Si$. The electrode thin film thicknesses were Pt (100 nm), TiO_2 (10 nm), silicon oxide SiO_2 (500 nm) and silicon wafer (725 μm). The 200 mm wafer was cut into small 2 cm $\times$ 2 cm squares. The electrode and the adhesion layer choice is discussed later in section (2.3.2). The platinum coated silicon substrate is presented in appendix A.3.

Prior to the solution deposition, the substrates were cleaned using an acetone solution in an ultrasonic bath cleaner for 3 min. The square substrate was placed on a circular spin chuck that suits the size of the substrate as shown in Fig.(2.3). The substrate must be settled in the middle of the spin chuck to make sure that the latter will be held by the vacuum of the spin coater. A couple of spin tests are done prior to the solution deposition to ensure that the substrate is fixed to the spin chuck and does not fall off during spin up.

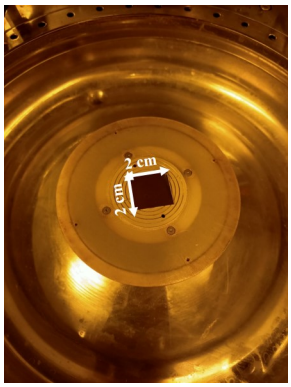

Figure 2.3: Substrate placed on the circular spin chuck prior to the solution deposition.

2.2.5.2 Thin film deposition

The solutions were filtered with a 0.2 μm polytetrafluoroethylene (PTFE) membrane filter prior to the deposition on the substrate. The sol-gel solution was deposited using a clean glass syringe to avoid the solution contamination. Once the solution is on the substrate, it should spread evenly and wet the surface of the substrate. The spin speed plays an important role in defining the final thickness of the films as mentionned earlier in section (2.2.3.1). The spin speed used in this work ranged from 1000 to 4000 rpm.

2.2.5.3 Film annealing process

In the earlier sections, it was mentioned that the heat treatment process is considered as a very important step in shaping the microstructure of the films and controlling the way the films crystallize. In the frame of this work, the two-step process has been utilized to accomplish the crystallization of the films. The pyrolysis step is performed by placing the films on a hot plate with temperatures ranging from 130°C to 450°C depending on the material decomposition profile. The pyrolysis process could last from 5 to 10 minutes for solvent evaporation and elimination of organic species. The films were then crystallized in a furnace at 700°C in air at ambient conditions. We explored different heat rates for high temperature annealing. The effect of long and short heat rates on the microstructure of the films is discussed later on in the following chapters.

2.2.5.4 Technological difficulties and solutions

During thin film deposition and thermal treatment, several technological issues arose. The two major difficulties encountered are listed below:

- Dewetting of the thin film caused by a larger surface energy of the solution compared to that of the substrate surface [28].
- Thin film cracking related to film thickness and thermal treatment process.

One solution to the dewetting problem was to perform a surface treatment on the substrate surface. Plasma CHF_3 and CHF_3/O_2 was conducted on the surface of the substrate. The CHF_3 treatment render the surface hydrophobic, for that matter the mixture of CHF_3 and O_2 was used to render it more hydrophilic.
Thin film cracking was observed in thick films. Fig.(2.4) shows the microscopic cracks at the surface of the deposited film.

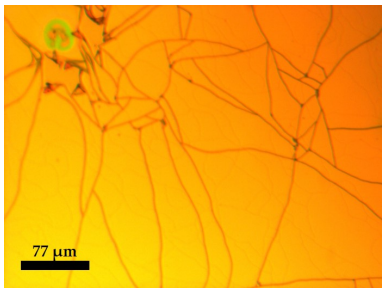

Figure 2.4: Optical microscope photo showing the microcracks of a barium strontium titanate solution deposited on a silicon substrate via spin coating at 1000 rpm and after a heat treatment at 600°C

The final thickness of the film is proportional to $v^{-2/3}$ as discussed in the previous section (2.2.3.1). The dependence of film thickness on the spin velocity is also shown in the spin curve in Fig.(2.5). In the region where the spin velocity is inferior to 1000 rpm, the theoretical thickness has a rather large value. It was also observed experimentally that for films spun between 300 and 1000 rpm, the thickness is significant and films exhibit cracking after thermal heating.

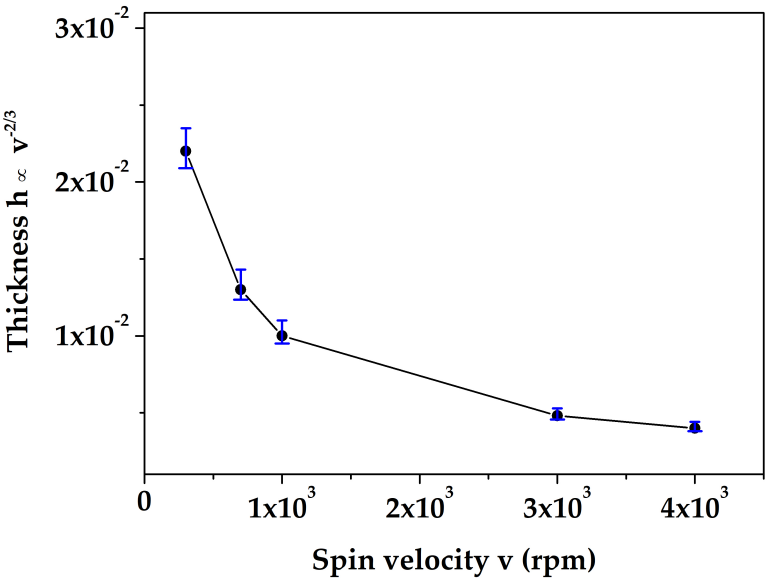

Figure 2.5: Spin curve showing the variation of the film thickness as a function of spin velocity.

Kozuka et al.[29] investigated stress and crack formation in alkoxide derived silica and titania films deposited on silica based substrates. They discussed stress formation in the various stages of thermal treatment. In the heating up and isothermal annealing stages, intrinsic stresses are formed in the film. Meanwhile, in the cooling down stage, a tensile stress occurs due to the mismatch of thermal expansion coefficient between the deposited film and the substrate. The study on the titania films showed that cracks form in the heating up stage at temperatures between 100°C and 400°C. The cracking onset temperature depends on the film thickness and heating rate. They found that thicker films began cracking at low heating temperatures ($\sim$ 100°C for SiO_2 films) and ($\sim$ 300°C for TiO_2). Thus, there is clearly a thickness dependence for crack formation in thin films. According to Kappert et al. [30], one can estimate theoretically the so-called critical thickness h_c by considering the energy release rate of a steady-state film cracking. Below h_c, the film remains crack-free. In short, film thickness is the main factor to consider when trying to avoid crack formation.
In the case of this study, thin film cracking was reduced using thinner deposited films. This was possible by increasing the spin velocity.

2.3 Functional ferroelectric thin film capacitors

In this section, a description of the ferroelectric thin film capacitor is presented. In addition, the electrode choice for the Metal-ferroelectric-metal (M-F-M) configuration is discussed as well.

2.3.1 Thin film capacitors

In the context of this work, the ferroelectric thin films are used in capacitor form. Herein, a brief introduction on capacitors and their characteristics is presented.
A capacitor is defined as an electrical component that can store energy in electrical form (electric field). It consists of parallel plates separated by a dielectric material. In Fig.(2.6), a typical parallel plate capacitor connected to a voltage source is shown, the positive and negative charges accumulate at each side of the plates, as the electrons migrate from the positive charge plate toward the negative plate, a current is created in the circuit and energy is stored inside the capacitor. Capacitance **C** is defined as the ability to store a charge q and is given by:

$$C = \frac{q}{V} \tag{2.3}$$

where V is the voltage and the unit of the capacitance is Farad (F).

As shown in Fig. (2.6), the plates of a parallel plate capacitor are separated by a dielectric of thickness d. Let us consider E and D the electric field and flux density between the plates.

$$E = \frac{V}{d} \qquad \text{and} \quad D = \frac{q}{A} \quad \text{with} \qquad D = \varepsilon E \tag{2.4}$$

where A is the area of the dielectric and ε the permittivity of the dielectric material. From Eq.(2.4), one can write:

$$E = \frac{q}{\varepsilon A}$$

that yields

$$\frac{q}{V} = \frac{\varepsilon A}{d} \tag{2.5}$$

that gives

$$C = \frac{q}{V} = \frac{\varepsilon A}{d}$$

$$\boxed{C = \frac{\varepsilon_0 \varepsilon_r A}{d}} \tag{2.6}$$

where ε_0 is the permittivity of vacuum (8.854×10^{-12} F/m) and ε_r is the relative permittivity of the dielectric material.

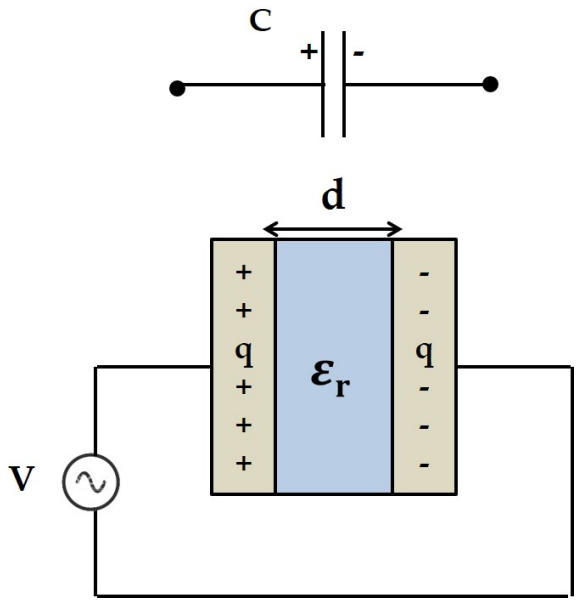

Figure 2.6: Parallel plate capacitor

2.3.2 Electrode choice

Electrode materials play an important role in determining the performance of the ferroelectric thin films, in particular the bottom electrode that acts as a buffer layer between the dielectric and the substrate [31]. The integration of ferroelectric thin films in devices

requires stabilized electrodes deposited on silicon substrates. The main concern is the bottom electrode thermal stability at high temperatures [32].

2.3.2.1 Experimental work

In the context of this work, several electrode materials have been tested. Table (2.1) summarizes the different top and bottom electrodes and their electrical performance. The

Bottom electrodes	Top electrodes	Performance
ITO/TiO_2	Au	very poor
ITO/TiO_2	Al	poor
Pt/Ti	Au	very poor
Pt/Ti	Al	very poor
Pt/Ti	Cr	poor
Pt/Ti	Ti	good
Pt/Cr	Au	very poor
Pt/Cr	Al	poor
Pt/Cr	Ti	poor
Pt/Cr	Cr	good

Table 2.1: Electrode materials and their electrical performance.

first attempts were conducted on silicon wafers with ITO as the conducting electrode. The electrical performance of this system was very poor. ITO was not stable and it oxidized at high temperatures. ITO was replaced with platinum Pt. Pt has a relatively high work function (5.12-5.93 eV) and chemical inertness in high temperature oxidizing atmosphere. Hence, Pt electrodes are suitable for ferroelectric devices [33]. One of the issues encountered while using Pt is the poor adhesion to silicon and silicon oxides.
This problem is solved by using an adhesion layer, with a typical thickness of 10-20 nm. Several adhesion layers were tested for the stabilization of Pt thin films in temperature [34]. A typical choice of adhesion layers was chromium (Cr) and titanium (Ti). As shown in table (2.1), Pt/Ti and Pt/Cr were tested and demonstrated good electrical performances when Ti and Cr top electrodes were employed respectively. However, electrical instabilities were still occurring once higher voltages were applied.
The studies conducted on the Pt/Ti system revealed the formation of TiO_x in the grain boundaries of the Pt, leading to the presence of hillocks on the surface of the Pt films [26, 35–38]. An alternative solution to this problem is to use a more stabilized layer of

TiO_2, to prevent diffusion in the Pt films. Ti diffuses faster than TiO_2 in Pt films during the annealing process.The oxidation of the Ti incorporates oxygen into the Pt layer causing volume expansion of Pt leading to the increase of the residual stress in Pt films.

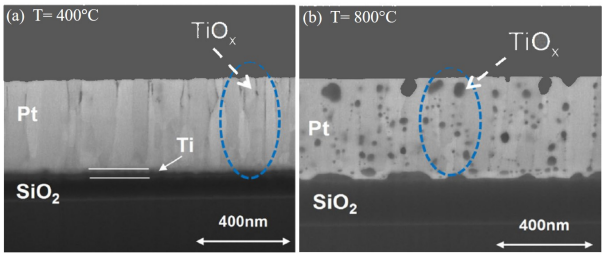

Figure 2.7: SEM figures showing the diffusion of Ti in Pt/Ti films at (a) 400°C and (b) 800°C; adapted from [34]

Fig.2.7 shows the degradation of the Pt films with the increase of the annealing temperature due to the diffusion of Ti which leads to the formation of oxide precipitates in the grain boundaries of Pt films. Fig.(2.7) (b) shows that the Ti layer has completely disappeared at 800°C, Ti has completely transformed into titanium oxides.

In light of what was reported in the literature, the study was limited to the Pt/Ti(TiO_2) electrodes. 20 nm of Ti and TiO_2 were deposited by evaporation on SiO_2 (3μm)/Si (725μm). The adhesion layers were not annealed after their deposition.
200 nm Pt was deposited by electron beam evaporation at a rate of 0.5 nm/s at RT under a vacuum of 10^{-6} mbar. Prior to the Pt deposition, an etching step was employed at 250V for 60s, in order to clean the surface of the adhesion layers and to enhance the adherence of the Pt films.
Final thermal annealing was performed on the film stack Pt/Ti(TiO_2)/SiO_2/Si at 600°C for one hour. The surface morphology of the Pt/Ti films before and after annealing at 600°C is shown in Fig.(2.8). The surface roughness of the Pt films after thermal annealing increases due to the formation of hillocks. Fig.(2.9) also showed the surface morphology of the Pt/TiO_2 films at RT and after annealing at 600°C. The surface roughness of the films increased remarkably at 600°C. Fig.(2.9) (b) presented a delaminated region of the Pt film, the cause of this delamination is not entirely clear but may be attributed to the oxidation of the amorphous TiO_2 films underneath.

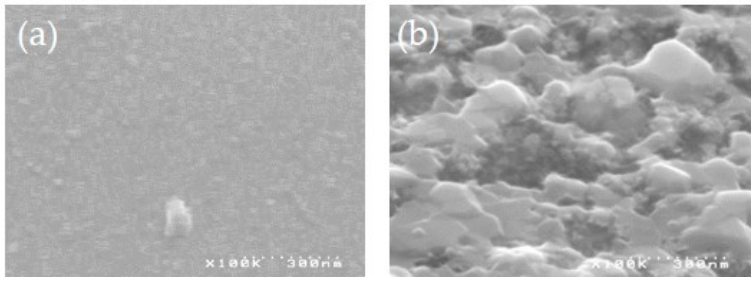

Figure 2.8: SEM images of (a) Pt/Ti electrodes before thermal annealing, and (b) Pt/Ti electrodes after thermal annealing at 600°C for 1 hour.

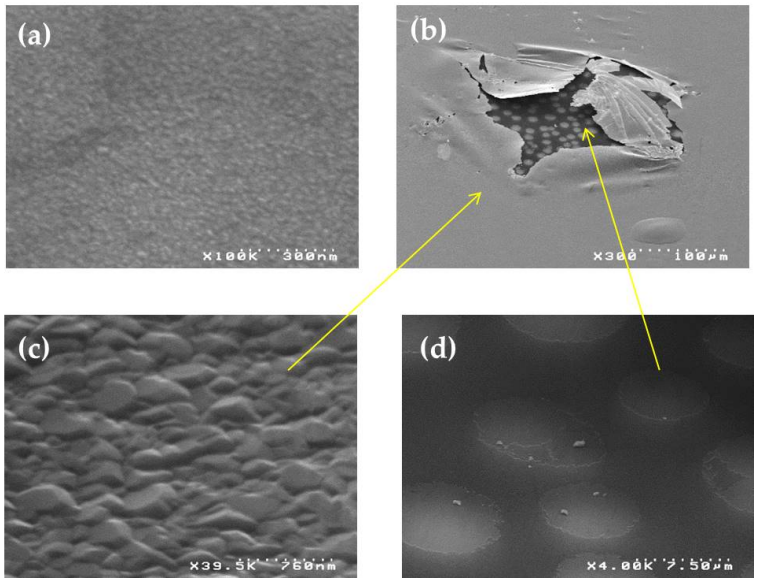

Figure 2.9: SEM images of (a) Pt/TiO_2 electrode at RT, (b),(c) and (d) Pt/TiO_2 after thermal treatment at 600°C for 1 hour.

After acknowledging the problems with the Pt bottom electrode, a stable system of $Pt/TiO_2/SiO_2/Si$ was employed. The main difference is in the intermediate thermal treatment of the Ti underlayer. The annealing of this layer under oxygen atmosphere contributed in transforming the Ti into stable TiO_2. In addition, the sputtering of the Pt films at a relatively high temperature of 450°C helped decreasing the residual stress in the films.

2.3.2.2 Top electrode deposition

A top electrode deposition is required to form a M-F-M configuration. Pt thin films were deposited using electron beam evaporation through a metallic shadow mask with circular patterns with different diameters as shown in the Fig.2.10. The evaporator MEB550 from PLASSYS was used to make the deposition operating with an electron gun at 10 kW. The films were evaporated at 0.5 nm/s to yield a thickness of 200 nm. Prior to the deposition, an etch with a step at 250 V for 60s was employed to eliminate any contamination on the surface of the dielectric film.

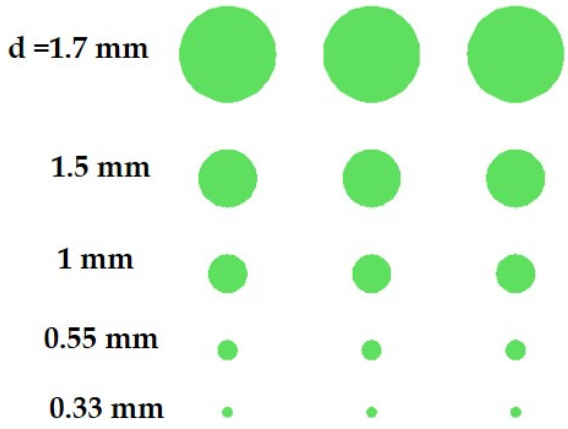

Figure 2.10: Designed shadow mask patterns.

2.4 Characterization techniques of thin films

The methods used for the thin film study are described in this section. It is divided into three subsections according to the nature of the characterization methods. In the first subsection, the morphological and structural techniques are presented: scanning electron microscopy (SEM), atomic force microscopy (AFM) and grazing incidence small angle x-ray scattering (GISAXS) were chosen to probe the morphology of the thin films at the nanoscale. X-ray diffraction (XRD) was chosen as a suitable technique to study the structure of the films. The second subsection is dedicated to the physico-chemical characterization technique, namely x-ray photoelectron spectroscopy (XPS) used for determining the composition of thin films. Finally, the last subsection will discuss the techniques used for the electrical characterization of the ferroelectric thin film capacitors.

2.4.1 Morphological and structural characterization

2.4.1.1 SEM

SEM is a very well known and practical method to explore the morphological aspects of materials at the nanoscale, in particular to probe the surface morphology and cross section of thin films. Zhou et al.[39] described in detail the fundamentals of SEM. For our work, the ZEISS LEO 1530 Field emission SEM (FE-SEM) was used to characterize the morphology of the thin films. The LEO 1530 is a high resolution SEM capable of sub-nanometer resolution. It is equipped with three detectors: In-Lens, SE, and BSE, a x/y/z motorized stage and operates at 0.2-30 kV.The optimization of the working parameters is an important step before proceeding to taking the images. For a flat and non-conductive sample, it is preferred to work with low voltage, hence a low working distance (WD). For the thin films in question, the In-Lens detector was used with a WD between 3 and 5 mm and a high voltage of 5 kV.

2.4.1.2 AFM

Atomic force microscopes operate on the principle of surface sensing using a sharp tip. The tip is used to perform a scan across the surface of the sample. There are two primary operating modes: contact mode and tapping mode. The principle of AFM is shown in Fig.(5.2), it consists of a nanoscale tip attached to a cantilever. In contact mode, the cantilever bends when the tip is in contact with the surface of the sample. The bending is detected using a laser diode and a split photodetector indicating an existing tip-sample interaction force. In tapping mode, the cantilever oscillates near its resonance frequency. The resonance curve of the cantilever shifts due to forces between the tip and the sample. If the cantilever is excited at a fixed frequency, the amplitude of the oscillations changes. These changes are detected by a photodiode and the distance between the tip and the sample is altered to maintain a constant amplitude.
The interest of using AFM in this study is to probe the surface morphology including the lateral grain size and the roughness of the thin films.

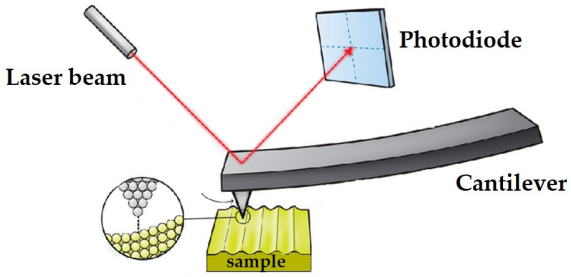

Figure 2.11: Schematic showing the AFM apparatus.

The measurement was performed in tapping mode on the surface of the thin films in the range of 1µm using an AFM from Innova-Bruker.

2.4.1.3 GISAXS

GISAXS is a powerful tool for characterizing thin film morphology. It is complementary to direct microscopy methods used to analyze the surface morphology and lateral spacing of surface structures. Microscopy methods have limitations such as small observable area and the need for vacuum and electrical conductivity. On the other hand, GISAXS can be performed at ambient conditions and allows recording relatively fast images (in the order of seconds or minutes depending on scattering contrast and beam intensity). Thus, GISAXS is an interesting tool to use in investigating film morphology and growth dynamics. The GISAXS geometry is depicted in Fig.(2.12). An x-ray beam with a wave vector $\mathbf{K}_i$ is directed to the thin film sample surface with a very small incident angle α_i with respect to the surface. The sample can be rotated around its normal axis. The x-rays are scattered along $\mathbf{K}_f$ on the plane (2θ, α_f). The scattered x-rays intensity is recorded on a 2D detector at very small angles for the observation of lateral sizes ranging from a few up to hundreds of nanometers [40]. The scattering wave-vector $\mathbf{q}$ is defined by:

$$\boldsymbol{q}_{x,y,z} = \frac{2\Pi}{\lambda}\begin{bmatrix} cos(\alpha_f)cos(\theta_f) - cos(\alpha_i) \\ cos(\alpha_f)sin(\theta_f) \\ sin(\alpha_f) + sin(\alpha_i) \end{bmatrix} \tag{2.7}$$

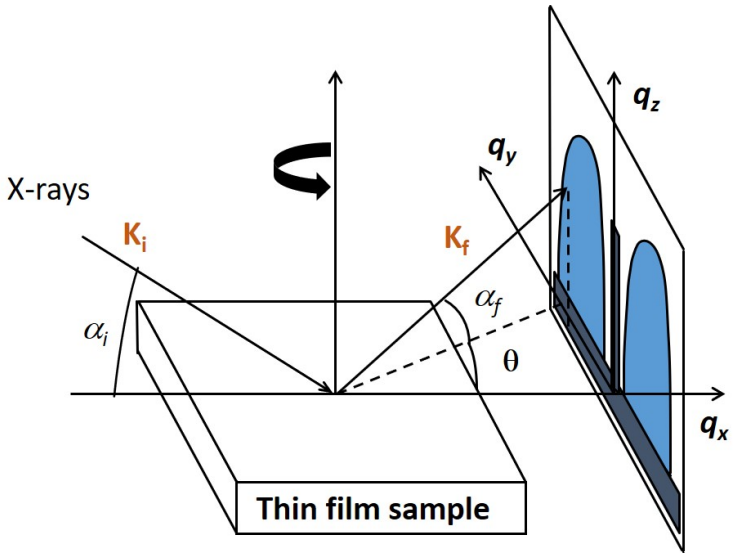

Figure 2.12: GISAXS geometry scheme.

GISAXS measurements were conducted at the European Synchrotron Radiation Facility (ESRF) in Grenoble on the BM02 beamline with an x-ray energy of 16 025 eV and an incident angle of 0.16° [41].

2.4.1.4 XRD

XRD is a powerful technique for studying material structure. The modern diffraction techniques allow us to perform measurements on thin films and ultra-thin films using adapted equipment.

In the case of this work, the phase of the films is crucial in order to get ferroelectric properties. The interest in using this technique was to identify the phases existing in the thin films and calculating the grain size from the peaks of the XRD patterns. In order to achieve that, θ- 2 θ scans were performed.

The measurement set up in Fig.(2.13) consists of a Panalytical Empyrean diffractometer equipped with a cobalt anode($\lambda K\alpha$ = 1.789 Å) and a chi, phi, z sample stage with RX, RY cradles for thin film alignment. It can be used in either diverging beam or parallel beam configuration.

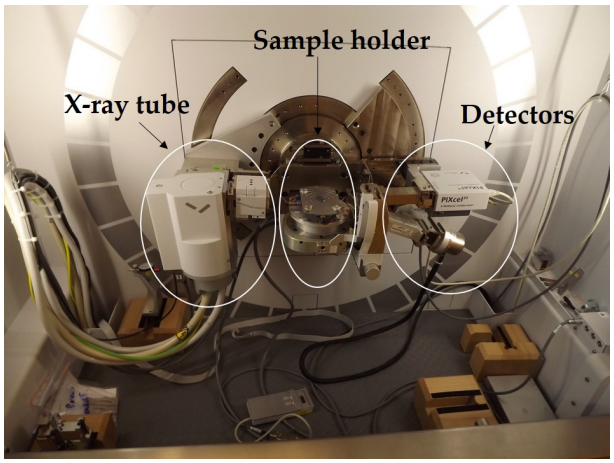

Figure 2.13: Panalytical Empyrean diffractometer.

The parallel geometry consists of a Goebel mirror, long plate collimator and a proportional punctual detector. The diverging geometry consists of divergence and anti-scattering slits, 255×255 pixels detector that can be used in 0 D, 1 D or 2 D modes. The measurements conducted using this diffractometer allow determining the structure, orientation and microstructure (perpendicular and out-of-plane strain and crystallite size) in polycrystalline, textured or epitaxial thin films. It can also be used to perform reflectivity measurements on thin films with thicknesses ranging from a few up to hundreds of nanometers. The pixcel detector was used to perform the XRD measurements on the thin films.

Sample alignment

The sample alignment is an important step to perform accurate measurements. Prior to the θ- 2θ scan, a sample alignment is performed. The incident optics used in the alignment were a 1/32 ° divergence slit, soller slits and a 4 mm mask. The diffracted optics were a parallel plate collimator and a proportional detector with a 0 D receiving slit. The z sample stage was set to zero and the incident angle 2 θ at 0°. A 2 θ scan was performed at z=0 within an angular range of 0.3°, a step of 0.05° and a step time of 0.5s to obtain the maximum peak at the 2 θ origin. A z scan is performed in the range of 3 mm with a step of 0.1 mm and a step time of 0.5s in order to adjust the sample height. A final ω scan is held in the range of 1.5° with a step of 0.05 ° and a step time of 0.5s to make sure that ω is parallel to the sample surface.

XRD measurement and analysis tools

Once the sample alignment is done, we can go through with the θ-2θ scan, the 1/32 ° divergence slit is replaced with a 1/4 ° slit, a proportional 1 D detector is used and an offset of ω = 1° is set to mitigate the Si (100) peaks contribution to the XRD spectra.The XRD analysis was conducted with the HighScore Plus software that allows phase identification, lattice parameters determination and size/strain analysis. The database used for crystalline phase identification was the ICDD PDF-4.

2.4.2 Physico-chemical characterization

XPS

XPS is a surface characterization technique. It can determine elemental composition, stoichiometry, electrical or chemical states and examine surface contamination. The components needed for conducting XPS measurements consist of an X-ray source, an electron analyzer and an electron detector, all maintained under UHV. XPS relies on the photoemission principle shown in Fig.(2.14), stating that when a sample is bombarded with x-rays of a known energy $h\nu$, core electrons are ejected with a kinetic energy E_k that will be measured by the detector. These electrons are called photoelectrons and their binding energy is given as follows:

$$E_k = h\nu - E_b - \phi_{sp}. \tag{2.8}$$

where $h\nu$ is the energy of the incident x-rays, E_b is the binding energy and ϕ_{sp} is the spectrometer work function. The spectrometer work function can be compensated since it is the combined sample and analyzer work function. Hence, Eq.(2.8) becomes:

$$E_k = h\nu - E_b. \tag{2.9}$$

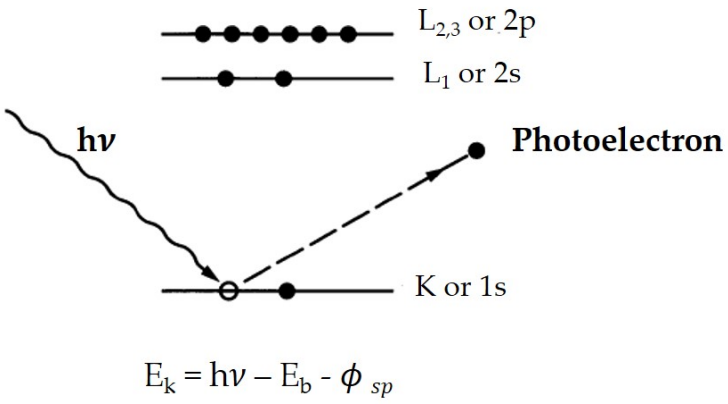

Figure 2.14: Photoemission process in XPS adapted from [42].

An XPS spectrum is plotted by using the intensity of the photoelectrons and their binding energy. The XPS peaks originate from the photoelectrons in the core levels and valence band and are characteristic for each element. Shifts in the XPS spectrum known as chemical shifts are due to binding energy variation. This variation is due to atoms being chemically bonded with different elements. The energy shift can be used to identify different oxidation states of an element [42].
Chemical characterization by XPS was carried out using a Versaprobe II ULVAC-PHI spectrometer. A monochromatic beam (X-ray source Al-Kα =1486.6 eV) of 100 μm of diameter and 97 W of power was focused at the surface of the samples. High-resolution spectral analyses were performed using a pass energy of 23.9 eV which corresponds to a resolution of 0.6 eV. All XPS measurements were carried out in an UHV chamber (7.10 - 10 mbar). The binding energy calibration was performed using Au4f7/2 (83.94 eV), Ag3d5/2 (368.2 eV) and Cu2p3/2 (932.6 eV). The core level binding energies were recorded within an error of ±0.1 eV.

2.4.3 Electrical characterization

The electrical study was conducted in the LCO (Laboratoire des Composants Organiques) laboratory at CEA LITEN. As mentioned in section 2.3.2.2, a M-F-M configuration is prepared to conduct the different electrical measurements on the thin film capacitors.

2.4.3.1 Dielectric measurements

The permittivity of the dielectric capacitor is the parameter that describes the ability of the material to polarize under an applied electric field. A practical way to determine the permittivity or the relative permittivity ϵ_r is the capacitance measurement.

The latter was performed using the Agilent E4980A Precision LCR Meter in the frequency range of 20Hz-2MHz. The full set up images are shown in appendixB.1. The meter usually applies an AC voltage to the capacitor, then it measures the voltage and the current across the capacitor. From the ratio of these two, the meter can determine the impedance Z. In combination with the impedance, the equivalent capacitance and resistance of the capacitor can be displayed.

The meter must assume one of the two circuit models shown in Fig.(2.15).

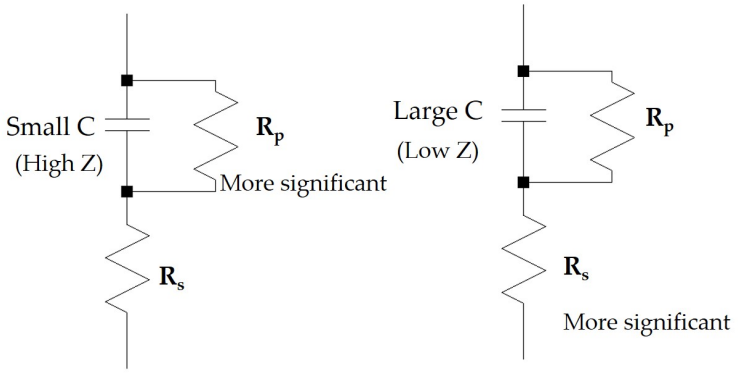

Figure 2.15: LCR circuits for capacitance and resistance measurements.

Small capacitance yields large reactance which implies that the parallel resistance (Rp) is larger than than the series resistance (R_s). The low value of resistance represented by Rs is negligible compared to the capacitive reactance, so the parallel circuit mode (Cp-Rp) should be used. Since the capacitance of the thin film capacitor are typically in the order of the nanoFarads (nF), the Cp-Rp mode is used to measure the parallel capacitance and resistance. For the case of our thin film capacitor, the parallel capacitance and resistance are measured as a function of the varying electric field frequency under an AC voltage, as well as a function of the bias at a given frequency. Both types of measurements allow assessing the relative dielectric constant (permittivity) as well as the dielectric losses inside the device and the polarization switching behavior of the ferroelectric thin films.

2.4.3.2 Current density

Current-voltage is a basic electrical measurement and ammows characterizing the various materials and devices under test. In this work, the current density of the ferroelectric thin film capacitor is investigated to understand the conduction mechanisms within the dielectric material.
The Agilent 4156C precision semiconductor analyzer is used to perform the I-V measurements, the set up is controlled from a PC with the Easy expert software. The same bench top with the sample holder used in the previous dielectric measurements is employed here. The main difference is that the probes are connected to a Source/Measure Unit (SMU). The diagram of the SMU circuit is presented in Fig.(2.16).

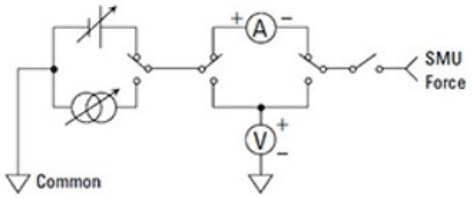

Figure 2.16: Scheme presenting the SMU simplified circuit.

It is an instrument that combines the capabilities of a current source, a voltage source, a current meter, and a voltage meter into a single instrument, it can measure in a much easier and quicker with far better accuracy and performance with less measurement error than the measurement integrating various conventional instruments.

I-V sweep measurements

The current-voltage characteristics of the thin film capacitor is measured by sweeping the voltage from 0 to 5V (sweep 1) and from 5V to 0 (sweep 2) with a step voltage of 0.5V. SMU channels and measurement details are shown in Fig.(2.17).

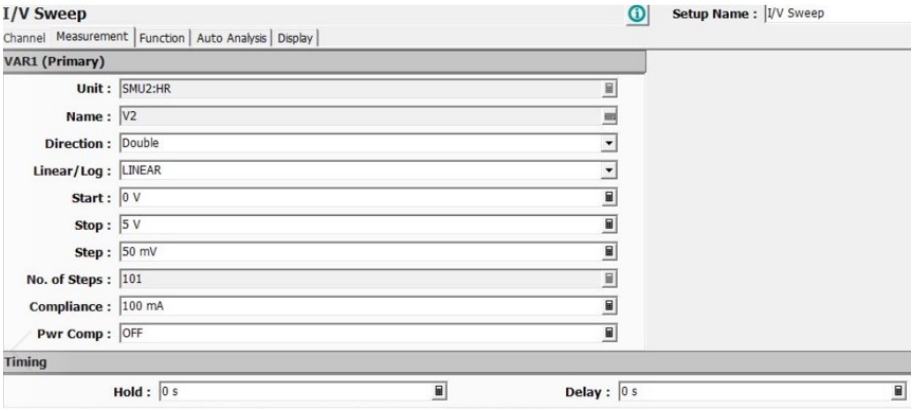

Figure 2.17: I-V sweep set up in Easy expert.

Two SMU channels are needed to perform an I-V sweep: a variant channel (VAR1) and a common channel (constant). The variant channel probe is usually set on the top electrode of the device under test and the common channel on the bottom electrode.
To conclude, a simple I-V measurement gives valuable information about the current density within the thin film capacitor which is an important information to consider for ferroelectric characterization.

2.4.3.3 Ferroelectric measurements

Polarization measurements

The Sawyer-Tower circuit was the original method for measuring ferroelectric hysteresis [43]. It consists of a simple circuit with two capacitors in series that should have the same charge: a ferroelectric capacitor and a standard capacitor. The standard or reference capacitor is chosen to have a larger capacitance than that of the ferroelectric capacitor. Hence, the potential across it is small and does not affect the potential across the ferroelectric capacitor.

The circuit is shown in Fig.(2.18), it consists of a voltage source, a non-linear ferroelectric film capacitor C_F, and a reference capacitor C_{ref}.

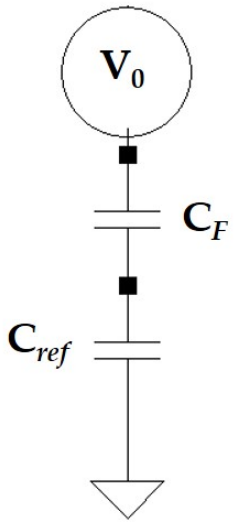

Figure 2.18: Simplified scheme of the Sawyer-Tower circuit.

When applying a voltage to the circuit, it splits into the sum of voltage drops over every circuit components. It can be written as follows:

$$V_0 = V_{C_F} + V_{C_{ref}}.$$

As mentioned above, the reference capacitance is chosen to be much larger than the ferroelectric capacitance so that most of the driving voltage drops on C_F. Since the capacitors are in series in the circuit, their charges are equal $Q_F = Q_{ref}$. So one can write:

$$V_{C_F} C_F = V_{C_{ref}} C_{ref}. \tag{2.10}$$

$$V_{C_{ref}} = \frac{Q_F}{C_{ref}}. \tag{2.11}$$

where $V_{C_{ref}}$ is the voltage drop on the reference capacitance. The polarization of the ferroelectric capacitor is the variation of charge divided by the area of the capacitance:

$$P = \frac{Q_F}{A}. \tag{2.12}$$

One can obtain the hysteresis loop by registering the voltage over C_{ref} versus the field strength which is defined as:

$$E = \frac{V_{C_F}}{d}. \tag{2.13}$$

where d is the thickness of the ferroelectric film.

Measurement set up

The equipment used for performing the polarization-electric field (P-E) hysteresis loop measurements is shown in appendix B.2. Fig.(2.19) shows a ferroelectric thin film capacitor on the test bench with the probes set on the sample. The reference voltage is connected to the bottom electrode and the drive voltage to the top electode of the sample.

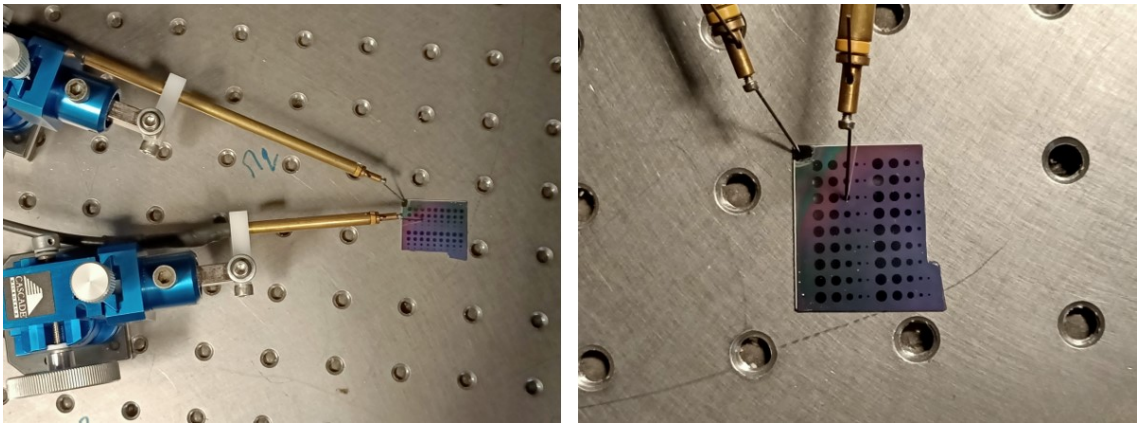

Figure 2.19: Ferroelectric thin film capacitor sample setting on the characterization test bench.

Prior to the actual polarization measurements, the samples were poled under an electric field at RT. Details about the poling process and its optimization are given in chapter five. The measurements were conducted at different electric fields and frequencies.

2.5 Conclusion

In conclusion, this chapter has presented the methods used in the elaboration of thin films. The processing of the solution derived inorganic perovskite thin films were discussed, shedding the light on the importance of the precursor synthesis chemistry and thermal annealing processes. In addition, the* effect of electrodes stability (bottom and top) on the functionality of thin film capacitors has been discussed. Then, the morphology and structure study techniques were shown and finally, the methods for the dielectric and ferroelectric measurements of the thin films were presented.

References

[1] Gould, R. D., Kasap, S., and Ray, A. K. *Thin Films*. Springer International Publishing, (2017).

[2] Jilani, A., Abdel-wahab, M. S., and Hammad, A. H. *Advance Deposition Techniques for Thin Film and Coating*. InTech, (2017).

[3] Schwartz, R. W. *Chemistry of Materials* **9**(11), 2325–2340 (1997).

[4] Brinker, C. J. and Scherer, G. W. *Sol-gel science: the physics and chemistry of sol-gel processing*. Academic press, (2013).

[5] Schwartz, R. W., Schneller, T., and Waser, R. *Comptes Rendus Chimie* **7**(5), 433–461 (2004).

[6] Rao, B. G., Mukherjee, D., and Reddy, B. M. In *Nanostructures for novel therapy*, 1–36. Elsevier (2017).

[7] Schneller, T., Waser, R., Kosec, M., and Payne, D. *Chemical Solution Deposition of Functional Oxide Thin Films*. Springer Vienna, (2013).

[8] Mahmood, A. and Naeem, A. *Recent Applications in Sol-Gel Synthesis* , 169–193 (2017).

[9] Brinker, C. J., Hurd, A. J., Schunk, P. R., Frye, G. C., and Ashley, C. S. *Journal of Non-Crystalline Solids* **147**, 424–436 (1992).

[10] Brinker, C., Hurd, A., Frye, G., Schunk, P., and Ashley, C. *Journal of the ceramic society of Japan* **99**, 862–877 (1991).

[11] Scriven, L. E. *MRS Proceedings* **121**, 717 (1988).

[12] Bornside, D., Macosko, C., and Scriven, L. *Journal of Imaging Science and Technology* **13**(4), 122–130 (1987).

[13] Bornside, D. E., Macosko, C. W., and Scriven, L. E. *Journal of Applied Physics* **66**(11), 5185–5193 (1989).

[14] Emslie, A. G., Bonner, F. T., and Peck, L. G. *Journal of Applied Physics* **29**(5), 858–862 (1958).

[15] Meyerhofer, D. *Journal of Applied Physics* **49**(7), 3993–3997 (1978).

[16] Sahu, N., Parija, B., and Panigrahi, S. *Indian Journal of Physics* **83**(4), 493–502 (2009).

[17] Schwartz, R. W. and Narayanan, M. In *Chemical Solution Deposition of Functional Oxide Thin Films,* Schneller, T., Waser, R., Kosec, M., and Payne, D., editors, 343–382. (2013).

[18] Lefevre, M. J., Speck, J. S., , R. W., Dimos, D., and Lockwood, S. J. *Journal of Materials Research* **11**(8), 2076–2084 (1996).

[19] Schwartz, R. W., Clem, P. G., Voigt, J. A., Byhoff, E. R., Stry, M. V., Headley, T. J., and Missert, N. A. *Journal of the American Ceramic Society* **82**(9), 2359–2367 (1999).

[20] Polli, A. D. and Lange, F. F. *Journal of the American Ceramic Society* **78**(12), 3401–3404 (1995).

[21] Li, S., Condrate Sr, R., and Spriggs, R. *Spectroscopy letters* **21**(9-10), 969–980 (1988).

[22] Klee, M., Eusemann, R., Waser, R., Brand, W., and van Hal, H. *Journal of Applied Physics* **72**(4), 1566–1576 (1992).

[23] Pardo, L. and Ricote, J., editors. *Multifunctional polycrystalline ferroelectric materials: processing and properties*. Number 140 in Springer series in materials science. Springer / Piezo Institute, Dordrecht, (2011).

[24] Pascual, R. and Sayer, M. *J. Appl. Phys.* **70**(4), 6 (1991).

[25] Kumar, C. V. R. V., Sayer, M., Pascual, R., Amm, D. T., Wu, Z., and Swanston, D. M. *Applied Physics Letters* **58**(11), 1161–1163 (1991).

[26] Brooks, K. G., Reaney, I. M., Klissurska, R., Huang, Y., Bursill, L., and Setter, N. *Journal of Materials Research* **9**(10), 2540–2553 (1994).

[27] Keddie, J. L. and Giannelis, E. P. *Journal of the American Ceramic Society* **74**(10), 2669–2671 (1991).

[28] de Gennes, P. G. *Reviews of Modern Physics* **57**(3), 827–863 (1985).

[29] Kozuka, H. *Journal of the Ceramic Society of Japan* **111**(1297), 624–632 (2003).

[30] Kappert, E. J., Pavlenko, D., Malzbender, J., Nijmeijer, A., Benes, N. E., and Tsai, P. A. *Soft Matter* **11**(5), 882–888 (2015).

[31] Ming Shiahu Tsai, Sun, S., and Tseung-Yuen Tseng. *IEEE Transactions on Electron Devices* **46**(9), 1829–1838 (1999).

[32] Maeder, T., Sagalowicz, L., and Muralt, P. *Japanese Journal of Applied Physics* **37**, 2007–2012 (1998).

[33] Golosov, D., Okojie, J., Zavadski, S., Rudenkov, S., Melnikov, S., and Kolos, V. *Thin Solid Films* **661**, 53–59 (2018).

[34] Ababneh, A., Al-Omari, A. N., Dagamseh, A. M. K., Tantawi, M., Pauly, C., Mücklich, F., Feili, D., and Seidel, H. *Microsystem Technologies* **23**(3), 703–709 (2017).

[35] Sreenivas, K., Reaney, I., Maeder, T., Setter, N., Jagadish, C., and Elliman, R. G. *J. Appl. Phys.* **75**(1), 9 (1994).

[36] Vélu, G. and Rèmiens, D. *Journal of the European Ceramic Society* **19**(11), 2005–2013 (1999).

[37] Abe, N., Otani, Y., Miyake, M., Kurita, M., Takeda, H., Okamura, S., and Shiosaki, T. *Japanese Journal of Applied Physics* **42**, 2791–2795 (2003).

[38] Sripumkhai, W., Porntheeraphat, S., Saekow, B., Bunjongpru, W., Rahong, S., and Nukeaw, J. *Journal of the Microscopy Society of Thailand* **24**(1), 51–54 (2010).

[39] Zhou, W., Apkarian, R., Wang, Z. L., and Joy, D. In *Scanning microscopy for nanotechnology*, 1–40. Springer (2006).

[40] Revenant, C., Leroy, F., Lazzari, R., Renaud, G., and Henry, C. *Physical Review B* **69**(3), 035411 (2004).

[41] Chahine, G. A., Blanc, N., Arnaud, S., De Geuser, F., Guinebretière, R., and Boudet, N. *Metals* **9**(3), 352 (2019).

[42] O'Connor, D. J., Sexton, B. A., Smart, R. S. C., Ertl, G., Lüth, H., and Mills, D. L., editors. *Surface Analysis Methods in Materials Science*, volume 23 of *Springer Series in Surface Sciences*. Springer Berlin Heidelberg, Berlin, Heidelberg, (2003).

[43] Sawyer, C. B. and Tower, C. H. *Physical Review* **35**(3), 269–273 (1930).

Chapter 3

Carboxylate based sol gel chemistry: from solutions to thin film formation

3.1 Introduction

Solution based routes such as sol gel are considered very versatile paths for metal oxide thin film elaboration. This type of chemical processing allows tailoring the properties of metal oxide thin films by modifying the precursor chemistry [1]. Sol gel processing can be used to fabricate thin film semiconductors such as IGZO [2–5] using the Pechini method [6]. This technique yields very thin layers ($\sim$ 5 nm per layer) which is suitable for semiconductor technology. On the contrary, dielectric thin films require thicker layers in order to be functional. Hence, a different approach is required for elaborating the precursor chemistry for dielectrics. In the sol gel method, carboxylate based chemistry is found to be well adapted for dielectric metal oxide thin films. The concept of this chemical route is straightforward and moisture insensitive which facilitates solution handling [7, 8].

In the context of this work, metal carboxylate precursors will be employed for thin film elaboration of two promising ferroelectric materials: strontium barium niobate (SBN) and barium strontium titanate (BST). SBN is synthesized in our laboratory using the carboxylate approach and BST is a commercial solution. This chapter will focus on the SBN precursor solution synthesis and thin film formation.

$Sr_xBa_{1-x}Nb_2O_6$ (SBN) thin films have been prepared by a plethora of methods ranging from physical deposition techniques to chemical deposition techniques [9–14]. In this chapter, the synthesis of SBN precursor solutions is explored using the carboxylate approach. Ideally, the expected molecular precursors of metals should be perfectly miscible

with one another. The molecular weight of the ligand must be reasonable allowing the formation of solutions with high concentration of metal. In addition, the challenging aspect is avoiding carbonate formation during oxide layer growth without oxygen annealing.

A brief introduction on the metal carboxylate chemistry and synthesis routes is presented throughout the chapter. The synthesis of SBN precursor solutions using carboxylic acids with various alkyl group ramifications is discussed in detail. The effect of solution chemistry on thin film morphology is probed using SEM. Furthermore, the composition of SBN films is investigated by XPS.

3.2 Alkoxide and carboxylate chemical approaches

In this section, metal alkoxides and carboxylates are introduced and their use in metal oxide thin films is discussed. The interest in the carboxylate route is highlighted for synthesis of stable precursor solutions.
The chemistry of metal alkoxides $M(OR)_x$ where M is a metal and R is an alkyl group, is very well documented and is extensively used in the sol gel processing of ceramics and perovskite thin films [15–17]. Mehrotra et al.[18–20] among others [21] have studied the synthesis and reactions of metal alkoxides and the characteristics of their structure. Reactions of metal alkoxides with solvents are considered as sol gel processes. Metal alkoxides are highly reactive chemical species which can be tailored in order to control their reactivity. Depending on the nature of the metal and the steric hindrance of the R group, the molecular complexity n of $[M(OR)_x]_n$ can be tuned. This parameter will impact the ability of mixtures of metal alkoxides to form heterometallic species. However, metal alkoxides are very reactive in solvents i.e water, alcohols and acids, rendering them susceptible to hydrolysis by moisture. They require careful handling, thus solution processing can be tedious and difficult. Among the available solvents, 2-methoxyethanol has been widely used as a reactant in the fabrication of perovskite thin film materials [7, 22]. This solvent is often used for its ability to dissolve large range of precursor materials. 2-methoxyethanol has also been found helpful in the dissolution of carboxylate precursors This solvent is quite effective, but it is toxic in nature [7, 23].

An alternative approach to prepare precursor solutions has been used: the carboxylate route. The chemistry of metal carboxylates is known since ancient times. Mehrotra et al.[24] described in their book the history of metal carboxylates, their synthesis, their physicochemical properties and their bonding nature.

What is a carboxylic acid?

A carboxylic acid RCOOH possesses a carboxyl group (COOH) and an alkyl group (R); Fig.(3.1) shows the general structure of the carboxylic acid.

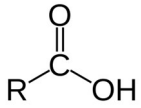

Figure 3.1: Scheme of the structure of the carboxylic acid.

The general formula for the carboxylic acids can be written in molecular form as C_nH_{2n+1} CO_2H where n+1/2 =(0-19). Metal carboxylates stem from carboxylic acids. Carboxylic acids are ionized in aqueous solution to give a stabilized carboxylate anion $RCOO^-$ and a hydrated proton H_3O^+. The carboxylate ions are far more stable than their free acid counterparts.

Among the carboxylate chemistry advantages, moisture insensibility and stability in air of the prepared precursor solutions are very important. The reactivity towards water is minimal and the esterification reactions are slower and less reactive. In contrast with the typical sol gel process where the hydrolysis and condensation reactions dominate, making solution manipulation more complex. In addition, the richness of the carboxylate chemsitry is shown in Fig. (3.2), by illustrating the different ways a carboxylate ion RCO^{2-} can coordinate to metals. The different bonding types are listed in the legend of Fig. (3.2) to show the versatility of carboxylate coordination.

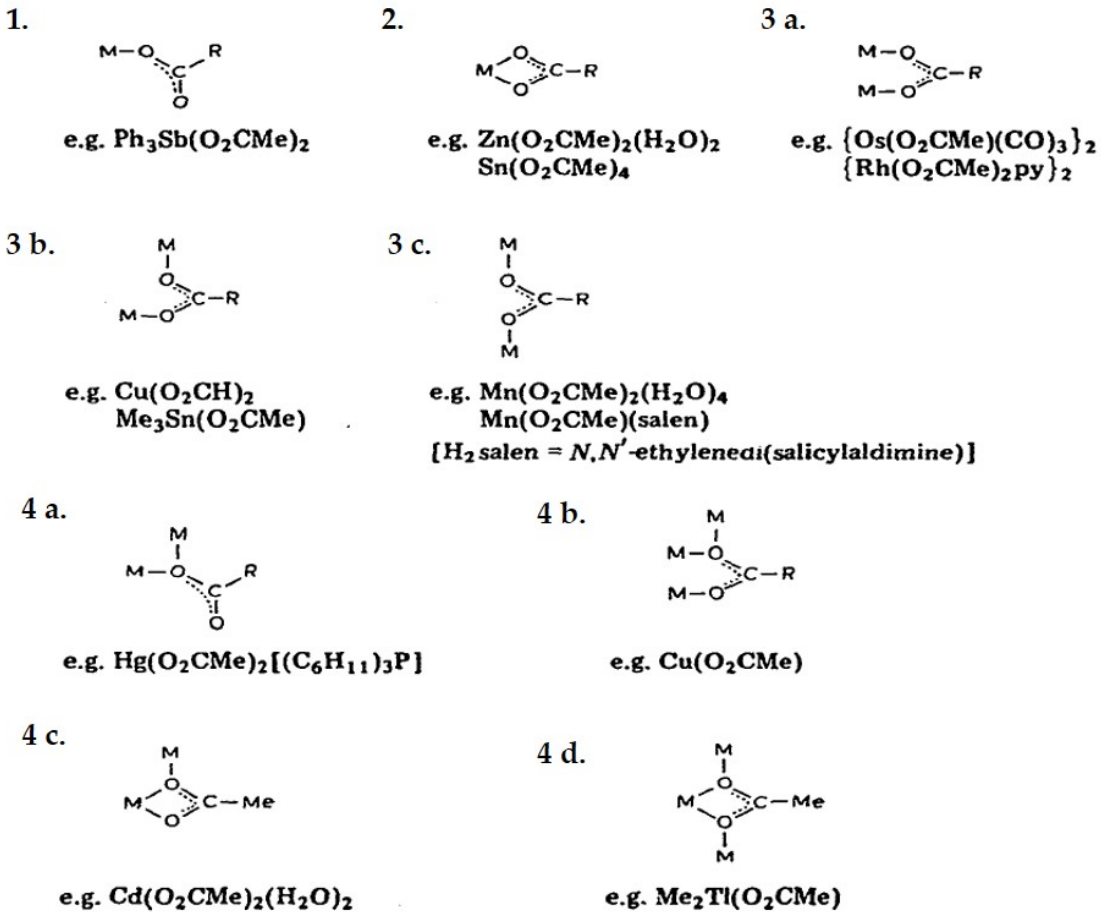

Figure 3.2: Carboxylate ion coordination to metals: (1) as a unidentate ligand, (2) as a chelating ligand, (3 a.) as a bridging bidentate ligand in a *syn-syn*, (3 b.) *syn-anti* or *anti-anti* configuration, or as a monatomic bridging ligand, either alone (4 a.), with additional bridging (4 b.), or in arrangements involving chelation and bridging (4 c., 4 d.). Figure adapted from Deacon et al.[25].

Steric hindrance effects

When a metal alkoxide reacts with a carboxylic acid, the following reaction occurs:

$$\mathrm{M(OR)}_n + n\mathrm{R'COOH} \longrightarrow \mathrm{M(OOCR')}_n + n\mathrm{ROH}$$

In this configuration, $\mathrm{M(OOCR')}_n$ is less reactive than its alkoxide counterpart. That is due to the steric effects of the R' group in the carboxylic acid. By definition, steric hindrance at a given atom in a molecule is the congestion caused by the physical presence of the surrounding ligands, which may slow down or prevent reactions at the atom. In

the case of carboxylic acids, steric hindrance effects become more important with larger R' groups. Thus, tailoring the reactivity and the molecular complexity n of the metal carboxylates is possible.

In the context of this thesis, the work on SBN solutions was inspired by the flexibility of the carboxylate approach that allowed us to tailor the solution chemistry. Multiple challenges were faced in the preparation of metal carboxylate solutions of each metal:

1. Stabilizing the solutions.
2. Miscibility of the mixture of precursor solutions.
3. Achieving high concentrations of metal precursors.
4. Obtaining the right stoichiometry for the mixture of precursors.

Several carboxylic acids with different alkyl groups and different solvents were tested in order to achieve those challenging aspects of solution making.
In the following sections, the synthesis routes of metal carboxylates, the choice of the carboxylic acids and synthesis of SBN metal precursors are discussed.

3.3 Synthesis routes of metal carboxylates

There are several possible reactions of metal derivatives with carboxylic acids or their metal carboxylates. The most popular methods to synthesize metal carboxylates are precipitation and fusion techniques. Reactions of metals in non-aqueous media have been used for precursor solution preparation. Precipitation method consists of the reaction of a metal salt with a solution of the alkali carboxylate in a solvent. The fusion method involves the reaction between the oxide or hydroxide of the metal with a fused fatty acid. Reactions of metal derivatives in non-aqueous media is frequently used with the less electropositive metals, whose salts are susceptible to hydrolysis in aqueous media [8, 24, 26]. Herein, the last technique can answer the requirements of SBN metal carboxylate solution synthesis.

Reaction of metal derivatives with carboxylic acids in non-aqueous media

This technique is suitable for the synthesis of metallic carboxylates that tend to hydrolyze in aqueous solutions as mentioned earlier. The mixture of various carboxylate

derivatives is possible using this method. The methods employed usually rely on the reaction of carboxylic acids or alkali metal salts with the metal derivatives in organic solvents.
Many types of reactions can occur depending on the metal derivatives. Two types of reactions were used in the chemical synthesis of the SBN solutions.

Reaction with metal halides

Metal halides (mostly chlorides) react with an alkali carboxylate in a suitable organic solvent to give a metal carboxylate and a metal salt. The side product (metal salt) is usually insoluble in the solvent and can be removed. The chemical reaction is written as follows:

$$\mathrm{M(X)}_n + n\mathrm{R'CO_2M'} \longrightarrow \mathrm{M(O_2CR')}_n + n\mathrm{M'X}$$

Several metal carboxylates have been prepared by reacting the metal halides with carboxylic acids or their alkali metal salts. The Nb carboxylate solution in this study was prepared using this technique. Nb pentachloride $NbCl_5$ was treated with sodium carboxylate. The resulting solution consisted of Nb carboxylate and sodium salt that was insoluble in the organic solvent and was removed by filtering the solution.

Reaction with metal alkoxides

The advantage of this route is that the side product is a non reactive alcohol. In contrast, side products such as metal salts and water H_2O are formed when halides, oxides and hydroxides are used as starting materials.
The reaction between the metal alkoxides and the carboxylic (organic) acids is written as follows:

$$\mathrm{M(OR)}_n + n\mathrm{R'CO_2H} \longrightarrow \mathrm{M(O_2CR')}_n + n\mathrm{ROH}$$

Another advantage of this technique is that the reactions can be carried out at much lower temperatures (100°C), thus side reactions at higher temperatures are avoided. Ba and Sr carboxylates were prepared by treating their alkoxides with carboxylic acids.

3.4 Solution chemistry of SBN carboxylates

The initial aim of the synthesis process of the SBN carboxylate solutions was to provide a miscible mixture of the three precursor solutions of Ba, Sr and Nb. The metal alkoxide route is very utilized for the formation of such precursor solutions [10, 12], but in the case of our system, it was challenging to obtain stable precursor solutions. The alternative carboxylate approaches discussed above were then employed for the preparation of SBN precursor solutions. As mentioned in section (3.3), Ba and Sr alkoxides were treated with carboxylic acids to attain the desired carboxylate solutions in the right metal stoichiometry. Metal alkoxides of Ba and Sr were first synthesized using the following reaction:

$$\mathrm{M} + n\mathrm{ROH} \longrightarrow \mathrm{M(OR)}_n + n/2\ \mathrm{H}_2$$

This method is restricted to strongly electropositive elements such as alkali and alkaline earth metals, since the alcohols have weak acid character [18]. ROH is the alcohol and $\mathrm{M(OR)}_n$ is the metal alkoxide of the metal M. Carboxylic acid was then introduced to form Ba and Sr carboxylates.

Niobium chloride was used as a starting reagent to make Nb carboxylate. It was mixed with a solution of sodium carboxylate to form the niobium caboxylate. The side product of this reaction was the sodium chloride (NaCl) that was not soluble in the alcohol solvent and was filtered later on.

In the case of this study, a number of carboxylic acids were employed to synthesize the precursor solution for thin film formation. The interest in varying the acids was to study the influence of alkyl group ramification on the precursor chemistry. In fact, when changing the alkyl group, steric factors change, in other words, carboxylate bonding modes differ thus, altering the solution chemistry.

The aim was to tailor the chemistry of the precursors in order to achieve good quality thin films that will have functional ferroelectric properties.

3.4.1 Choice of carboxylic acids

The debate on whether to choose a short chain or long chain carboxylic acids has been reported elsewhere [8]. The major drawback of using short chain carboxylates was the formation of an intermediate carbonate phase. On the other hand, long chain carboxy-

lates exhibit faster thermal decomposition. Hence, the difference between the short chain and long chain carboxylates is the decomposition behavior. The long chain carboxylates are preferred in the CSD routes for being moisture insensitive and can dissolve in relatively inert solvents. The primary criteria for the solution synthesis were the solubility of the metal precursors in the appropriate acids, the miscibility of the three precursor solutions of Ba, Sr and Nb and finally the ability to achieve relatively high metal concentrations. Carboxylic acids that had relatively high C-chain length were chosen as shown in Fig.(3.3). The steric hindrance effects play an important role in decreasing the reactivity of the components and slowing down the esterification reactions that produce water.

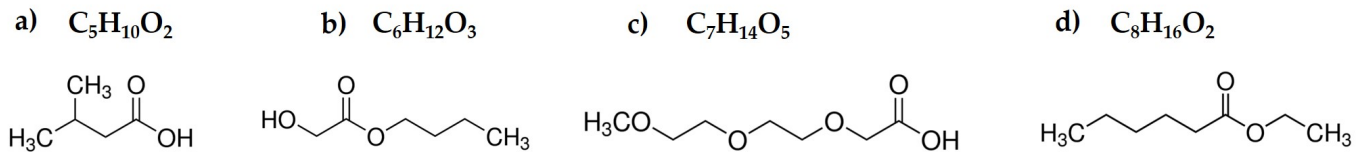

Figure 3.3: Scheme showing the formulas of the carboxylic acids :(a) Isovaleric (MW=102.13 g/mol), (b) Butyl glycolate (MW=132.16 g/mol),(c) 2-(2-methoxyethoxy)ethoxy acetic acid (MW=178.18 g/mol) and (d) 2-Ethylhexanoic (MW=144.21 g/mol).

3.4.2 Synthesis of SBN precursor solutions

In the following, experimental details for the preparation of SBN carboxylates are discussed. The general reactions were first presented then real quantities of metals, solvents, and the different carboxylic acids are summarized in Tables (3.1) and (3.2).

Niobium carboxylates:

In a round bottom flask filled with argon Ar, sodium (Na) metal was dissolved in 2-isopropoxyethanol (Iso) and methanol (MeOH). The mix was put on a magnetic stirrer until the sodium is completely dissolved, then a stoichiometric amount of carboxylic acid (RCOOH) was added to the formed Na alkoxide. Na is very reactive and H_2 was clearing out following the reactions below:

$$\mathrm{Na} + \mathrm{iP_rCH_2CH_2OH} \xrightarrow{MeOH} \mathrm{NaOCH_2CH_2OiP_r}(\textbf{Na alkoxide}) + \mathrm{H_2}$$

$$NaOCH_2CH_2OiP_r + RCOOH \longrightarrow NaO_2CR : \textbf{Na carboxylate}$$

In another flask, niobium chloride $NbCl_5$ was dissolved in MeOH. A stoichiometric amount of sodium carboxylate was then added. The reaction of Nb alkoxide with Na carboxylate yielded a final solution containing Nb carboxylate and NaCl as shown in the reaction below:

$$NbCl_5 \xrightarrow{MeOH} NbCl_5, xMeOH + 5NaO_2CR \longrightarrow [Nb(COOR)_5]_n + 5NaCl$$

Fig.3.4 (a) presents the flask with a white Nb carboxylate solution, the white color is due to NaCl residue. The final solution was then filtered using a pump under vacuum to remove the excess salt as shown in Fig.3.4 (b).

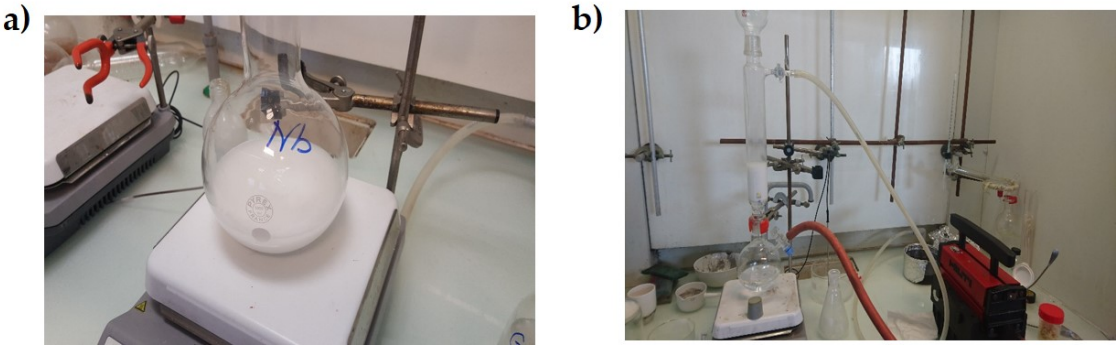

Figure 3.4: Pictures showing the flask containing a white Nb carboxylate solution (a) and the NaCl filtering process (b).

Barium and Strontium carboxylates:

For the alkaline earth elements Ba and Sr, the alkoxides of these metals were first prepared then carboxylic acids were added to obtain the metal carboxylates.

Sr carboxylate: In a round bottom flask filled with Argon Ar, Sr metal was dissolved in Iso and MeOH under constant stirring. Carboxylic acid was added and the stirring continued at 70°C.The resulting solution was white and after some time, crystallization of the liquid solution began. Fig.3.5 (a) shows the white Sr 2-ethylhexanoate solution when crystallization was occurring. The solution was extremely viscous and little crystal aggregates were forming. This phenomena occurred due to the high concentration of Sr

in the solution. More solvent was added to dilute the solution and was further stirred at 70 °C until the solution turned clear and limpid as presented in Fig.3.5 (b).

$$\mathrm{Sr_{(metal)} + iP_rCH_2CH_2OH \xrightarrow{\mathit{MeOH}} [Sr(OCH_2CH_2OiP_r)_2]_n : Sr\ alkoxide}$$

$$\mathrm{[Sr(OCH_2CH_2OiP_r)_2]_n + 2RCOOH \longrightarrow [Sr(COOR)_2]_n : Sr\ carboxylate}$$

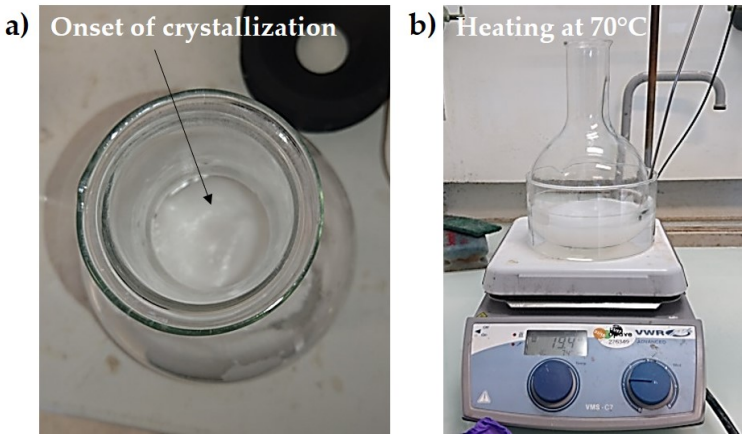

Figure 3.5: Pictures taken of (a):Sr 2-ethylhexanoate solution beginning to crystallize and (b) Heating the Sr 2-ethylhexanoate solution at 70°C in a hot water bath under stirring.

Barium carboxylate: In a similar manner, Ba carboxylate was prepared by first dissolving Ba metal in Iso and MeOH, then adding the carboxylic acid. The solution was under constant stirring and heating at approximately 70°C.

$$\mathrm{Ba_{(metal)} + iP_rCH_2CH_2OH \xrightarrow{\mathit{MeOH}} [Ba(OCH_2CH_2OiP_r)_2]_n :}\ \textbf{Ba alkoxide}$$

$$\mathrm{[Ba(OCH_2CH_2OiP_r)_2]_n + 2RCOOH \longrightarrow [Ba(COOR)_2]_n :}\ \textbf{Ba carboxylate}$$

Tables (3.1) and (3.2) represent the quantities of metals, solvents and carboxylic acids involved in the preparation of the precursor solutions of Na,Ba,Sr and Nb. The weight of the carboxylic acids was calculated as follows:

$$m_{acid} = \frac{n_{metal}}{M_{metal}} \times \text{ionization number of the metal} \times M_{acid}.$$

No carboxylic acid was added to the niobium pentachloride since it was mixed with the resulting sodium carboxylate after its dissolution in the solvent. The final solutions consisted of a mixture of Ba, Sr and Nb carboxylates.
Table (5.6) represents the chosen mixture compositions. The precursor solutions of Ba,Sr and Nb were named after the respective carboxylic acid. The mixture of the different solutions was first made with the same type of carboxylates for the three metal precursors. This mixture is called T1. Then, mixtures of different metal precursor carboxylates were elaborated and were called T2 and T3. The main interest in preparing those different mixtures is to evaluate the effect of the chosen solution chemistry on the final state of the thin films.

Metals	Metal weight (g)	Solvents	Solvent weight (g)	Carboxylic acids	Acid weight (g)
Na	4.09	Iso	114	2-Ethylhexanoic	25.92
$NbCl_5$	5.12	MeOH	84	-	-
Ba	2.52	Iso/MeOH	65/24	2-Ethylhexanoic	5.5
Sr	1.86	Iso/MeOH	51/75	2-ethylhexanoic	6.32

Table 3.1: Table representing the metals and solvents used in the preparation of the precursor solutions using 2-Ethylhexanoic acid.

Metals	Metal weight (g)	Solvents	Solvent weight (g)	Carboxylic acids	Acid weight (g)
Na	1.53	MeOH/EtOH[1]	37/30	Butyl glycolate	8.86
$NbCl_5$	3.6	MeOH	37	-	-
Ba	1.10	MeOH/EtOH	58/39	Isovaleric	1.63
Sr	1.08	MeOH/EtOH	45/29	2-2[2]	4.39

Table 3.2: Table representing the metals and solvents used in the preparation of the precursor solutions using different carboxylic acids.

[1]EtOH is ethanol

[2]2-2 is short for 2-2(methoxyethoxy)ethoxy acetic acid.

Solutions	Ba carboxylate	Sr carboxylate	Nb carboxylate	Metallic wt.%
T1	Ba 2-ethylhexanoate	Sr 2-ethylhexanoate	Nb 2-ethylhexanoate	7
T2	Ba 2-ethylhexanoate	Sr 2-2	Nb glycolate	13
T3	Ba isovalerate	Sr 2-2	Nb glycolate	15

Table 3.3: Table showing the different mixed precursor solutions and their weight percentages.

3.4.3 Preparation of SBN thin films

After the preparation of the three SBN solutions, they were left in the clean room for a few days to stabilize. Then, spin coating is used to deposit the solutions onto a silicon substrate. Prior to the deposition, the substrates were cleaned in acetone and the solutions were filtered using a 0.2 μm PTFE membrane filter.
For this experiment, the speed of the spin coater was limited to 1000 rpm and two spin velocities were used successively for each sample:
Spin 1:

- t=10s
- speed= 300 rpm,
- acceleration = 100 rpm/min

Spin 2:

- t=30s,
- speed= 1000 rpm,
- acceleration = 300 rpm/min

After the spin coating step, the deposited film was pyrolyzed at 200°C for 10 min then 450°C for 10 min on a hot plate in air prior to the final annealing. This pre-annealing was used to decompose the organic species in the film structure. The films were then annealed at 600°C in air for one hour to achieve the crystallization of SBN thin films.

3.5 Characterization of SBN thin films

3.5.1 Morphological study

The surface morphology of the deposited thin films was characterized by SEM. Fig.(5.23) presents the plane view of the three thin film samples annealed at 600°C. The morphological difference between the three samples is clear in the SEM images. T1 has a rough surface showing a non continuous film. Many pores are present due to the combustion of organic species, mainly the carbon residue from the long chain carboxylates. The morphology of the T1 sample is similar to particles rather than a homogeneous film.
T2 exhibits a smoother surface morphology with less pores, the film is more homogeneous and uniform. The surface defects and roughness decreased. T3 presents a mildly granular surface. T3 microstructure is much denser, this is due to the higher metallic percentage in solution T3.

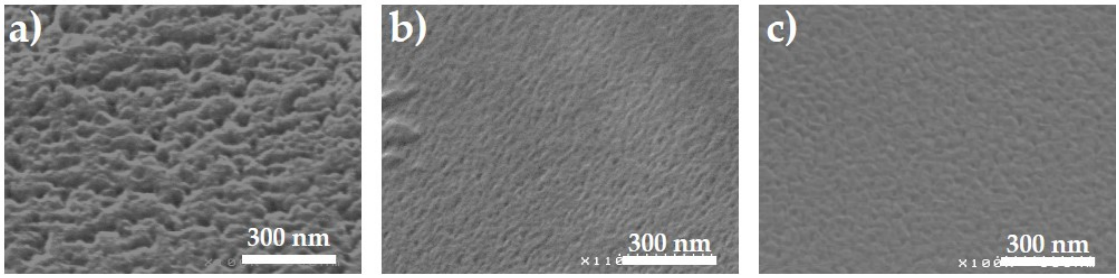

Figure 3.6: SEM images showing the plane view of one deposited layer of SBN thin films on ITO/Si/SiO_2 after thermal treatment at 600°C: (a)T1, (b)T2 and (c)T3 samples.

The above images clearly indicate that solution chemistry has a strong influence on the morphology of films. When the ligands of carboxylates change, the bonds between the different mixed precursors change as well. These changes also manifest through thin film morphology.

SEM summary

- SEM figures show different morphology for T1,T2 and T3.
- Sample T1 with the lowest metal wt.% and longest alkyl group has more surface defects such as significant surface roughness, pores and non-uniform films.
- T2 and T3 have smoother surface morphology and less surface defects.

3.5.2 Composition analysis

The XPS measurements were conducted on the surface of the annealed SBN thin film samples to investigate their composition. The interest in these measurements was to identify the presence of carbonates on the surface of the SBN thin films. The samples contained Ba, Sr, Nb, O and C in their surface region. Some impurity elements were present, mainly Na and Cl in small concentrations due to the NaCl residues from the preparation of Nb carboxylates. The different concentrations are presented in Table (3.4).

Samples	C1s	O1s	Na1s	Sr3d	Nb3d	Ba4d
T1	19.99	29.95	0.29	2.88	4.28	42.56
T2	18.70	39.41	1.17	9.09	10.34	21.26
T3	19	27.99	0.18	2.05	3.73	46.97

Table 3.4: Table showing the concentrations of the different elements present in the SBN thin film samples.

Figs.(3.7) and (3.8) show the XPS spectra of Ba4d, Sr3d, Nb3d, O1s, C1s and the deconvoluted O1s spectra respectively. Ba, Sr, and Nb spectra did not show significant variations in peak positions for the three samples. In contrast, C1s and O1s spectra showed additional peaks in T1 in comparison with T2 and T3.

Barium, Strontium and Niobium:

The elements are present in different concentrations in the three samples (see table 3.4). Ba has a valence of +2 (Ba^{2+}) and Nb is present as Nb^{5+} in all samples. $SrCO_3$ is the dominant environment for Sr in the three samples. The Ba4d peaks are more intense for T1. In contrast, $SrCO_3$ and Nb peaks are less intense for T1 and have similar intensities for T2 and T3.

Carbon and oxygen:

As depicted in Fig.3.7 (d), the C1s peak around 284 eV belongs to the C-C linkage and is present in all three samples. Another peak around 289.46 eV corresponds to the contribution of the carbonate CO_3 that is significant in T1, on the other hand, the C1s spectra for T2 and T3 show little carbonate.
O1s XPS spectra are presented in Fig.3.7 (e), the peaks around 529.7 eV correspond to O^{2-}. This represents the oxygen species in the SBN lattice, normally it is linked to a metal M (MO) in the structure. This peak is intense for T2 and T3, and less important for T1. In contrast, a significant peak around 531 eV is present in T1. It represents the contribution of the carbonates.

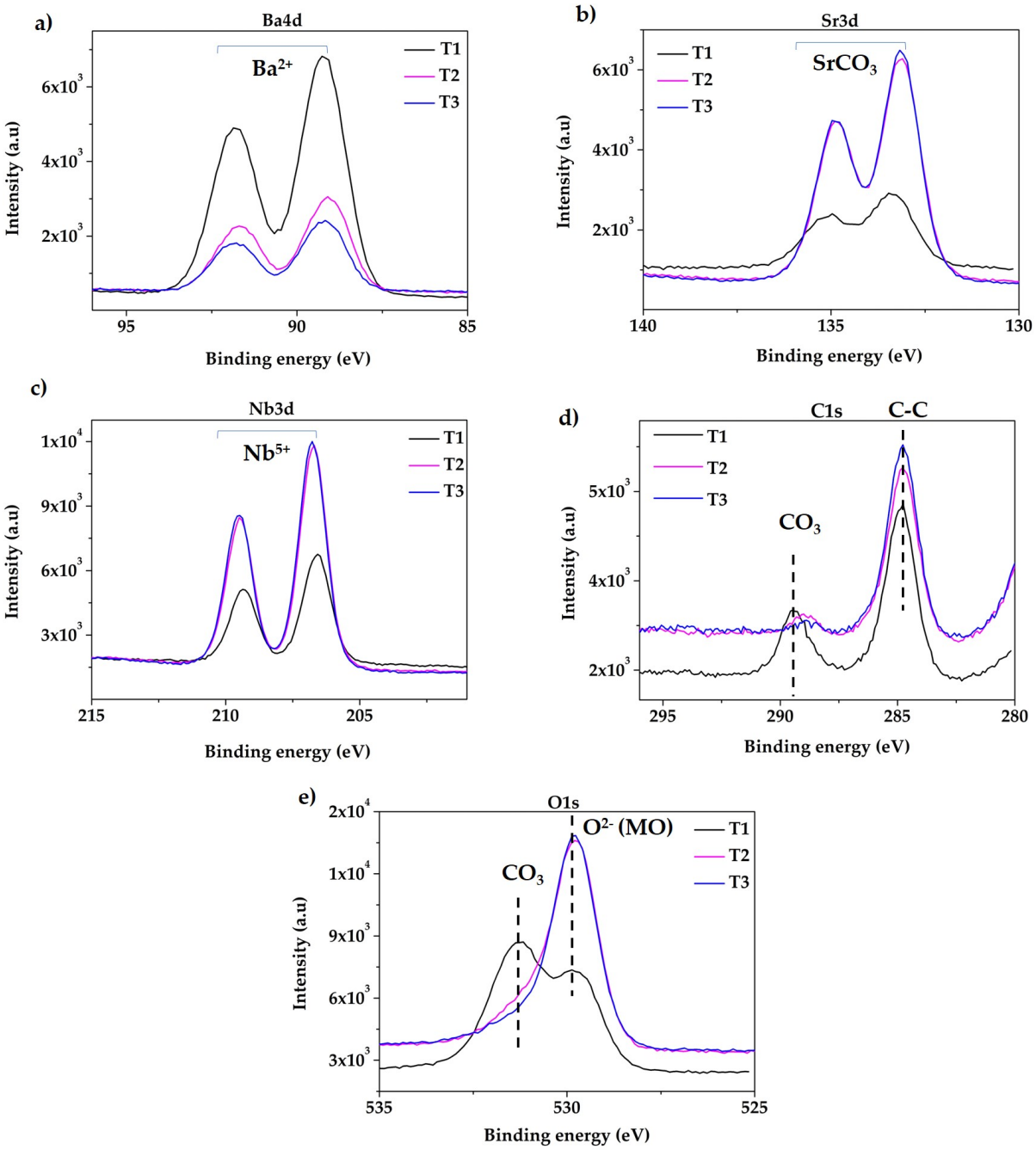

Figure 3.7: XPS spectra for Ba4d, Sr3d, Nb3d, O1s and C1s of the three samples T1,T2 and T3.

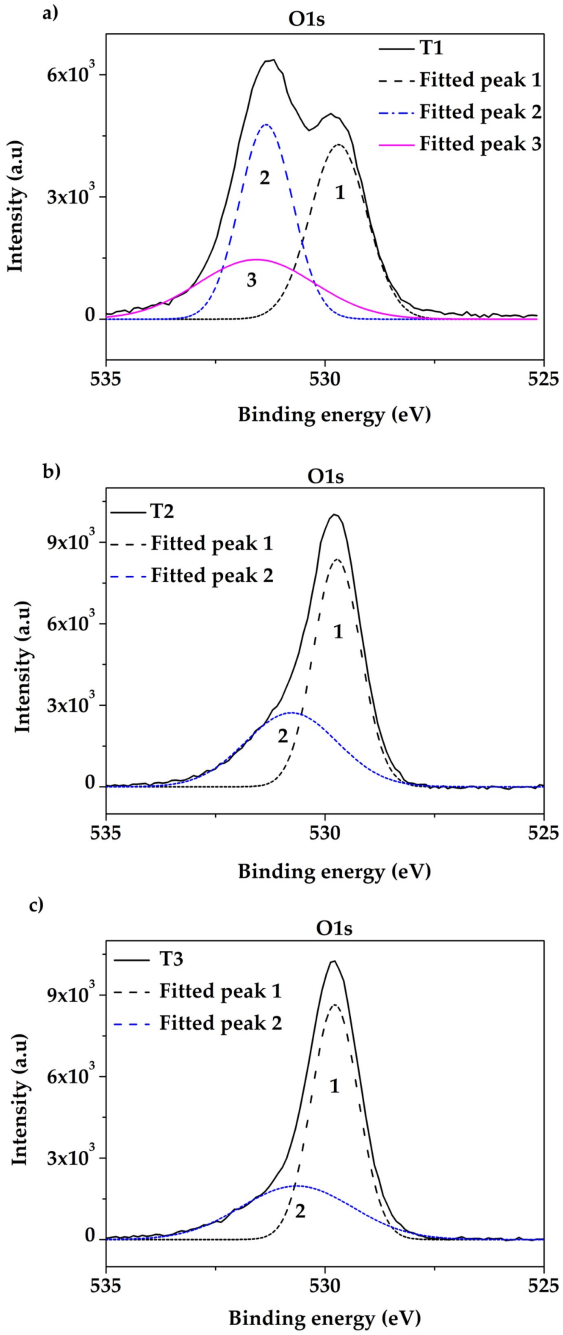

Figure 3.8: XPS spectra of deconvoluted O1s band structure for: (a) T1, (b) T2 and (c) T3.

Fig.(3.8) focuses on the deconvoluted O1s spectra. The binding energy values at 529.69 eV (peak 1), 531.34 eV (peak 2) and 531.57 eV (peak 3) are present in T1 sample. These peaks are associated with O^{2-} species in the lattice, oxygen from carbonates and chemisorbed or dissociated species (OH^{-}, CO, COOH) respectively. The binding energy values at 529.72 $\pm$ 0.5 eV (peak 1) and 530.65 $\pm$ 1.2 eV (peak 2) are present in T2 and T3

samples. They are associated with oxygen in the structure and carbonates (CO_3) respectively. CO_3 related peaks in C1s and O1s spectra are significant in T1. The decomposition of the carboxylates in T1 has left carbonates and carbon residue. This is not the case for T2 and T3, where little carbonates were found.

XPS summary

- Presence of carbonates on the surface of SBN thin films, significantly in T1 sample.
- Difference in stoichiometry between T1, T2 and T3.
- Presence of Na impurities.

3.6 BST solutions

The SBN solutions synthesized in our laboratory show promising results and yielded homogeneous thin films for some precursor mixtures. Further work is needed to achieve the correct stoichiometry and eliminate the carbonates. Thus, we chose to work with the BST commercial solution in order to obtain a functional ferroelectric capacitor during the PhD work. The BST solution is stable and has the right metal stoichiometry. Thus, it is a better candidate to move forward with this project and to properly study the physics of thin films.
The BST commercial solution is provided by Mitsubishi Materials Corporation. The data sheet in Fig. (3.9) shows the composition of the metal carboxylates of each metal in addition to the carboxylic acid and solvents involved.

Substance / Mixture: Mixture

Ingredients and Composition:

Chemical Name	CAS No.	wt%	OSHA TWA(mg/m³)	ACGIH TWA(mg/m³)
Barium 2-ethylbutyrate	—	0～14%	—	—
Strontium 2-ethylbutyrate	—	0～15%	—	—
Titanium tetra-iso-propoxide	546-68-9	5～14%	—	—
2-Ethylbutyric acid	88-09-5	14～22%	—	—
Isoamyl acetate	123-92-2	45～65%	525	532

Figure 3.9: BST solution data sheet from Mitsubishi Materials Corporation.

The description in the data sheet is very vague, for that reason the composition percentages are adapted from Sette et al.[27]. It comprised of approximately 7 wt.% of metallic precursor, 88 wt.% of isoamyl acetate, and 5 wt.% of isoamyl alcohol.

3.7 Conclusion

SBN precursor solutions were successfully synthesized using the carboxylate route. This route yielded miscible solutions with high metallic concentration. The use of carboxylic acids with variant ramification resulted in different solution chemistry and film morphology. SEM results manifest various thin film morphology for T1, T2 and T3 samples, T2 having the most compatible morphology for the desired thin films. XPS put in evidence carbonate species in SBN films, particularly in T1 sample. The carbonate presence is a very common issue in this type of chemistry and is detrimental for thin film functionality. Using this route, there is a way to eliminate the carbonates even without annealing under oxygen atmosphere. The chemistry of the solutions itself was not thoroughly characterized since it was not the main aim of this thesis.
This chapter focused on the synthesis of the SBN solutions and the promising carboxylate route in the preparation of thin film materials.
Further studies are required to fully understand the mechanisms of SBN thin film formation from carboxyate solutions. In light of the current findings, the BST commercial solution will be used to conduct technological and fundamental studies described in the remaining two chapters.

References

[1] Bretos, I., Jiménez, R., Ricote, J., and Calzada, M. L. *Chem. Soc. Rev.* **47**(2), 291–308 (2018).

[2] Benwadih, M., Coppard, R., Bonrad, K., Klyszcz, A., and Vuillaume, D. *ACS Applied Materials & Interfaces* **8**(50), 34513–34519 (2016).

[3] Revenant, C. and Benwadih, M. *Thin Solid Films* **616**, 643–648 (2016).

[4] Revenant, C., Benwadih, M., and Maret, M. *Chemical Communications* **51**(7), 1218–1221 (2015).

[5] Revenant, C., Benwadih, M., and Proux, O. *physica status solidi (RRL)–Rapid Research Letters* **9**(11), 652–655 (2015).

[6] Dimesso, L. In *Handbook of Sol-Gel Science and Technology*, Klein, L., Aparicio, M., and Jitianu, A., editors, 1–22. Cham (2016).

[7] Schwartz, R. W. *Chemistry of Materials* **9**(11), 2325–2340 (1997).

[8] Schneller, T., Waser, R., Kosec, M., and Payne, D. *Chemical Solution Deposition of Functional Oxide Thin Films*. Springer Vienna, (2013).

[9] Chen, C. J., Xu, Y., Xu, R., and Mackenzie, J. D. *Journal of Applied Physics* **69**(3), 1763–1765 (1991).

[10] Hirano, S.-i., Yogo, T., Kikuta, K.-i., and Ogiso, K.-j. *Journal of the American Ceramic Society* **75**(6), 1697–1700 (1992).

[11] Koo, J., Jang, J. H., and Bae, B.-S. *Journal of the American Ceramic Society* **84**(1), 193–199 (2001).

[12] Shen, Z., Ye, H., Mak, C., Wong, K., Yum, T., Liu, W., and Zou, T. *Materials Chemistry and Physics* **99**(1), 10–14 (2006).

[13] Scarisoreanu, N. D., Dinescu, G., Birjega, R., Dinescu, M., Pantelica, D., Velisa, G., Scintee, N., and Galca, A. C. *Applied Physics A* **93**(3), 795–800 (2008).

[14] Gupta, S., Kumar, A., Gupta, V., and Tomar, M. *Vacuum* **160**, 434–439 (2019).

[15] Guglielmi, M. and Carturan, G. *Journal of Non-Crystalline Solids* **100**(1-3), 16–30 (1988).

[16] Chandler, C. D., Roger, C., and Hampden-Smith, M. J. *Chemical Reviews* **93**(3), 1205–1241 (1993).

[17] Danks, A. E., Hall, S. R., and Schnepp, Z. *Materials Horizons* **3**(2), 91–112 (2016).

[18] Mehrotra, R. C. *Journal of Non-Crystalline Solids* **100**(1), 1 – 15 (1988).

[19] Bradley, D. C. *Chemical Reviews* **89**(6), 1317–1322 (1989).

[20] Mehrotra, R. C. *Journal of Non-Crystalline Solids* **121**(1-3), 1–6 (1990).

[21] Turova, N. Y., Turevskaya, E. P., Kessler, V. G., and Yanovskaya, M. I. *The chemistry of metal alkoxides*. Springer Science & Business Media, (2006).

[22] Halder, S. and Gottstein, G. Technical report, Fakultät für Georessourcen und Materialtechnik, (2006).

[23] Pardo, L. and Ricote, J., editors. *Multifunctional polycrystalline ferroelectric materials: processing and properties*. Springer, (2011).

[24] Mehrotra, R. and Bohra, R. *Metal Carboxylates*. Academic Press, (1983).

[25] Deacon, G. *Coordination Chemistry Reviews* **33**(3), 227–250 (1980).

[26] Mishra, S., Daniele, S., and Hubert-Pfalzgraf, L. G. *Chemical Society Reviews* **36**(11), 1770 (2007).

[27] Sette, D., Kovacova, V., and Defay, E. *Thin Solid Films* **589**, 111–114 (2015).

Chapter 4

Effect of thermal annealing on the morphology of sol–gel processed BST thin films: Consequences on electrical properties

4.1 Introduction

In the previous chapter, the carboxylate route was investigated for its promising potential in ferroelectric thin film elaboration. The chosen material to go forward with the study on thin film formation was BST due to the sol gel solution stability. In addition, BST is a good candidate for ferroelectric thin films applications.
In this chapter, the link between the morphology and the electrical properties of the sol-gel processed $Ba_{0.7}Sr_{0.3}TiO_3$ thin films is investigated. Previous studies have not fully explained the differences in growth morphology as a function of the elaboration conditions.
First, Grazing Incidence Small Angle X-ray Scattering (GISAXS) technique was used extensively to study the film morphology. *In situ* measurements allowed to probe the morphology from the very beginning of organic-inorganic phase separation in the film as a function of thermal annealing. *Ex situ* measurements allow following particle and pore formation as a function of the annealing temperature. The effects of the annealing time from 5 min to 60 min and of the substrate (SiO_2 or Pt) were also investigated. A general

model for sol-gel film formation based on the physics of fluids at the nanoscale [1] was developed. This model is also completed with the *in situ* GISAXS observations, at the very beginning of the liquid film annealing. Finally, optimized deposition and annealing conditions allow us to obtain preliminary ferroelectric capacitor results.

4.2 BST thin films

BST has been intensively studied due to its high pyroelectric coefficient [2] and is also used for microwave applications [3]. The BST films are typically elaborated by sintering [4], sputtering [5], or sol-gel [6, 7]. Sol gel as seen in previous chapters, is a versatile and simple technique. Sol gel derived BST thin films can be ferroelectric [8, 9]. For $Ba_xSr_{1-x}TiO_3$, the annealing temperature necessary for crystallization and the Curie temperature increase with x [10, 11]. Hence, a good compromise seems to be x $\sim$ 0.7, in order to get a Curie temperature slightly above RT without using very high annealing temperatures. For many applications, the dielectric performances are crucial. As the pyroelectric figure of merit is inversely proportional to the dielectric constant, a low value of the permittivity is favorable [12]. One possibility of decreasing the dielectric constant of BST layers is to introduce porosity. Interestingly, porosity formation occurs intrinsically during the sol-gel process. For $Ba_{0.7}Sr_{0.3}TiO_3$ samples prepared by sol-gel with grain size less than 1 μm, permittivity decreases swiftly with grain size decrease [13].

4.3 Fundamental study of BST thin films

Previous studies of sol-gel $BaTiO_3$ and $SrTiO_3$ thin films have shown different morphologies according to the individual layer thickness [14]. For a thickness up to typically 10-20 nm, columnar growth occurs. In fact, multiple sol-gel layers are usually deposited in order to reach the desired final film thickness. Between each sol-gel deposited layer, at least one thermal annealing is performed in order to remove a large amount of organic constituents. During annealing, nuclei occur and then form fractal aggregates, which are often studied with the Diffusion-Limited Aggregation (DLA) model [15]. Fig. (4.1) depicts the steps from solution to film formation. It shows the evolution of the sol up to the film state.

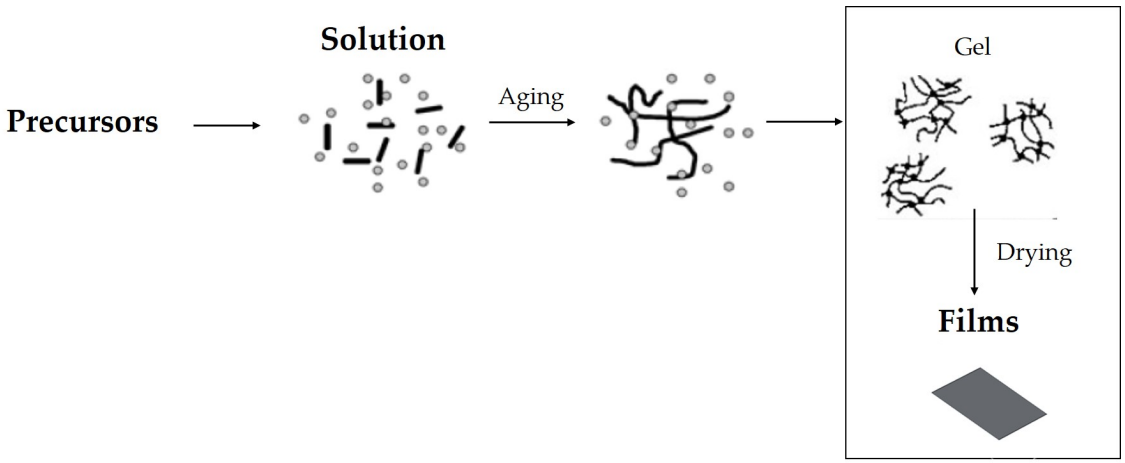

Figure 4.1: Schematic illustrating the steps from solution to film formation.

Although sol-gel films are widely used, the underlying physical processes governing the film evolution from the liquid state up to the dry one are not yet clearly understood. This part of the chapter is dedicated to unraveling the drastic morphology evolution from the liquid film up to the dry one as a function of thermal annealing.

4.3.1 Decomposition of BST solution

Before jumping to the thin film deposition, the decomposition behavior of the BST sol gel solution was thoroughly studied using thermogravimetric analysis (TGA). This will allow us to assess the evolution of the BST solution with increasing temperature.
The sol-gel solution was dried at 150°C for 24 hours in air prior to the TGA analysis. The measurement was conducted by heating the dried gel in air from RT to 800°C. The curve in Fig.(4.2) indicates that the weight of the BST solution begins to decrease at approximately 140°C, corresponding to the boiling temperature of isoamyl acetate (142°C). From 200°C to 400°C, a sharp decrease in the weight occurs. This decrease corresponds to the removal of the organic compounds. Above 440°C, the weight loss is very small indicating that most of the organic species have evaporated and decomposed.

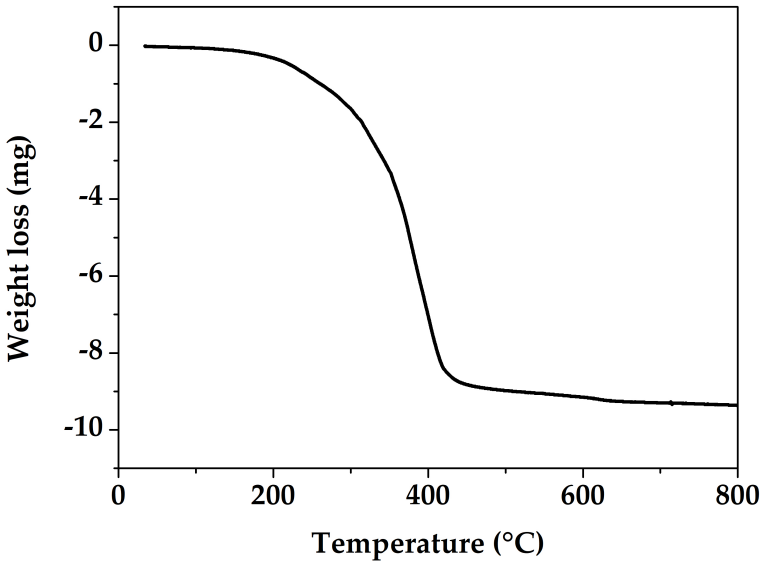

Figure 4.2: TGA analysis of BST dried solution.

4.3.2 Thin film preparation

For the fundamental study conducted on the BST films, the BST solution was deposited on SiO_2 (3 μm)/ Si (725 μm) and Pt(200 nm)/Cr(20 nm)/SiO_2(3 μm)/Si (725 μm) substrates by spin coating. As a matter of fact, Pt is used as an electrode for the BST thin film capacitor configuration. Prior to the solution deposition by spin coating, the substrates were cleaned with acetone and isopropanol in an ultrasonic cleaner and then rinsed with deionized water. The BST solution was spun at 300 rpm for 10s, then, 1000 rpm for 30s. The as-deposited films were pre-annealed on a hot plate at 130°C for 5 min for pyrolysis and 360°C for 5 min for organic decomposition, similarly to the annealing process used for the BST capacitors [16]. The deposition-pre-annealing cycle was repeated five times before the final annealing. The samples were annealed at 600°C for 1h and a half on a hot plate, 700°C or at 800°C for 1h in a conventional furnace under ambient air conditions. From the observation of the films by cross-sectional SEM, one could get the film thickness (approximately 640 nm).

4.3.3 GISAXS study of BST films

GISAXS is indeed a powerful technique to probe sol-gel thin films [17, 18], leading to a better knowledge of said films [19]. As a matter of fact, X-rays are particularly well-adapted for liquid or gel films for which microscopy studies are difficult. X-rays yield statistical information and *in situ* X-ray experiments can be carried out as a function of thermal annealing. More precisely, the GISAXS technique allows us to obtain characteristic sizes in the directions parallel and perpendicular to the surface.
In order to gain insight into the statistical morphology of the films, GISAXS measurements were performed. The measurements took place at the European Synchrotron Radiation Facility (ESRF) on the BM02 beamline with an X-ray energy of 16 025 eV and an incident angle of 0.16° [20]. The GISAXS analysis was performed with the FitGISAXS software [21]. The setup images are shown in appendix (C.1). Several measurement campaigns were conducted to study the *in situ* morphology evolution of the films up to 200°C and the *ex situ* morphology evolution as a function of annealing temperature, time and substrates. The *in situ* GISAXS measurements for one deposited layer are discussed first, then, the *ex situ* GISAXS of one and several deposited layers will be presented.

4.3.3.1 *In situ* GISAXS

For *in situ* measurements, the solution was deposited on the SiO_2/Si substrate, annealed at 130°C during 5 min prior to the experiment. A hot stage (Anton Paar DHS 900) shown in appendix (C.2) was used for heating the samples during the experiment. The Anton Paar operated in ambient environment without the dome for *in situ* annealing up to 200°C. The deposited solution was mainly formed of the isoamyl acetate liquid $C_7H_{14}O_2$ with a density of 0.876 g cm^{-3}, corresponding to a critical angle of $\sim 0.07°$. The attenuation length was as large as 26 μm for isoamyl acetate, i.e., the deposited solution was probed through the whole film thickness.
GISAXS measurements were performed as a function of the momentum transfer parallel to the sample surface q_y and the momentum transfer perpendicular to the sample surface q_z. Fig.(4.3) displays *in situ* GISAXS images of one liquid BST layer on SiO_2/Si at 25°C, and successively annealed at 137°C, 150°C, 190°C, and 200°C for 5 min at each temperature. The GISAXS measurement was performed at RT after each annealing.

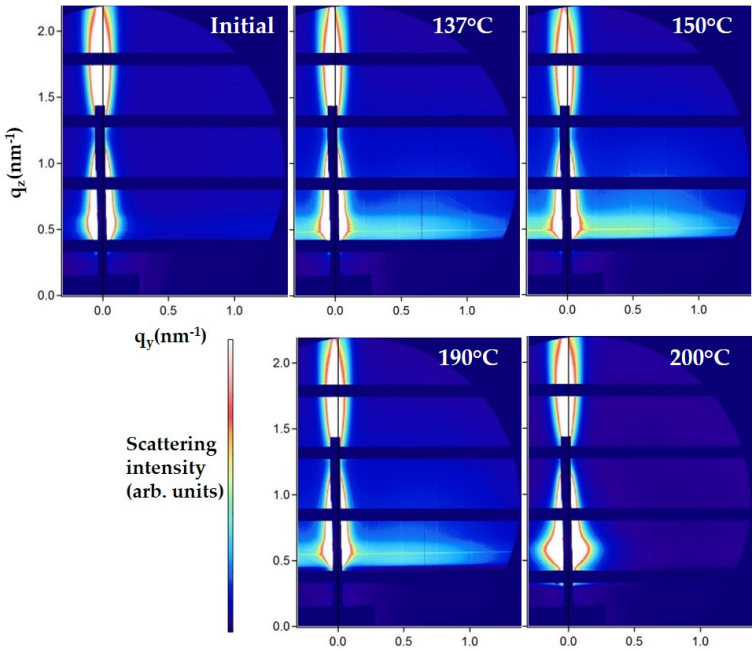

Figure 4.3: *In situ* GISAXS images of one liquid BST layer on SiO_2/Si at 25°C and successively annealed at 137°C, 150°C, 190°C and 200°C.

The initial state has a scattering at high q_z, indicating an electronic density contrast in out-of-plane direction. More precisely, the scattering has a maximum at q_z ∼1.73 nm^{-1}. The layer thickness is determined by Δq_z between two nearby q_z minima. Here, Δq_z∼ 0.9 nm^{-1} corresponds to a layer thickness of approximately 7 nm. This means that the inorganic compounds are not homogeneously distributed in the solvent-rich film. The 7 nm layer at the surface of the initial BST film can be explained by comparing the different surface tension of the various compounds. No value of the BST surface tension was found in the literature. Nevertheless, the surface tension of $BaTiO_3$ is ∼ 2.6 N/m for the bulk and 0.68 N/m for nanowires [22] and that of isoamyl acetate is 24 mN/m [23]. As the surface tension of the inorganic compound is larger than that of the solvent, there is a depletion layer (poor in BST) of thickness ξ near the free surface which is the characteristic size of the inorganic compound. Such an effect has already been put as evidence in other systems [24].

At the initial state, Fig. (4.3) shows that there is a slight scattering at high q_y (∼ 1 nm^{-1}). This scattering is due to the tiny particles distributed in the entire solvent. The evaporation step begins at 137 °C, characterized by a wide scattering appearing along q_y but thinner along q_z, indicating narrow columnar domains. Between adjacent domains, the solvent/inorganic fraction changes and a solvent-rich domain adjacent to a solvent-poor domain is observed. In Fig.(4.4), horizontal cuts were performed as a function of q_y at the critical angle, as well as vertical cuts as a function of q_z. After annealing at 150°C,

the wide scattering has maximum visibility at q_y ∼0.46 nm^{-1} in Fig.(4.4).

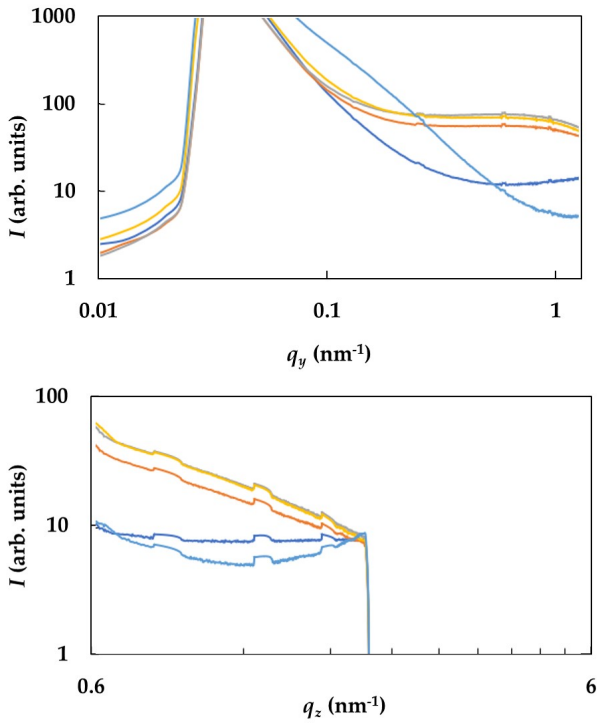

Figure 4.4: Linescans as a function of q_y at the critical angle and as a function of q_z with logarithmic scales: initial state (light blue), annealing at 137°C (orange), at 150°C (gray), at 190°C (yellow), and at 200°C (dark blue). The "bumps" originate from the dark regions in the detector and are, of course, not taken into account for the slope calculation.

This corresponds to a preferential distance D ∼ 14 nm, which is parallel to the surface, between two columnar domains having similar electronic densities, i.e., organic-rich or inorganic-rich domains. At 190°C, the scattering has a smaller extension along q_y (Fig.5.24), meaning that the domains grow.
In general, at high q_y or q_z the curves ln(I) may vary linearly as a function of ln(q_y) or ln(q_z), indicating that the intensity varies as q^{-n}, where the exponent n is characteristic of the sharpness of the diffusing entity [25]. For q_y and q_z larger than 1 nm^{-1}, the slope of ln(I) is found to be similar for ln(q_y) and ln(q_z) and is approximately -1.4 for annealing at 137°C, -1.6 at 150°C, and -1.7 at 190°C (Fig.(4.4)). These exponents do not correspond to a simple geometrical shape. For example, n=2 in the direction perpendicular to a plane, n=3 in the direction perpendicular to the curved surface of a cylinder, and n=4 for a sphere. Hence, the exponents correspond to the fractal dimension of the particles [26]. Fractals exhibit similar patterns at increasingly small scales, i.e., the scattering domains have a "zigzag" interface. The experimental exponents are in the range of that found for DLA in

2D models (1.67) [15].
The scattering shrinks along q_y after the final annealing at 200°C, revealing larger domains.

Fig. (4.5) summarizes the *in situ* morphology evolution of the deposited film from RT up to 200°C. In the initial state at RT, tiny inorganic particles are dispersed in the organic solvent (Fig. 4.5 (A)). With the increasing temperature at 150°C, the solvent starts to evaporate, which causes the beginning of a phase separation between the inorganic and organic entities. The wide and thin scattering at q_y and q_z respectively at 150°C indicate the presence of narrow columnar domains with D $\sim$ 14 nm as shown in Fig.4.5 (B). The evaporation of the solvent causes convection and diffusion movements in the film. Thus, the inorganic particles start to regroup forming inorganic-rich domains adjacent to organic-rich domains. This phenomenon will be detailed later on using a convection model. At 200°C (Fig.4.5 (C)), solvent evaporation continues, enlarging the domains and showing the onset of grain and pore formation in the film structure.

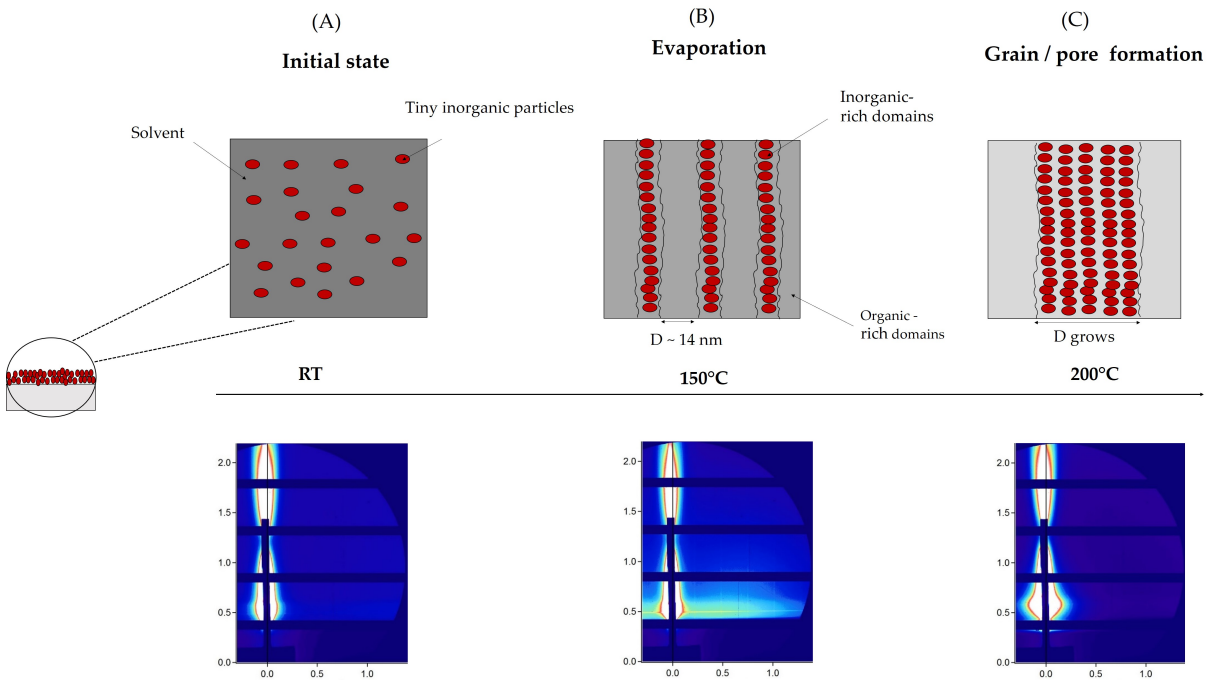

Figure 4.5: Cross-section schematic representing the *in situ* evolution of the deposited film as a function of temperature up to 200°C.

In situ GISAXS summary

- This experiment brings general knowledge about the very beginning of the sol-gel thin film formation starting from the liquid state.
- At low annealing temperatures, a density modulation occurs between adjacent domains in the liquid film.
- A phase separation between organic-rich and inorganic-rich domains occurs.

4.3.3.2 *Ex situ* GISAXS

Ex situ measurements were performed on one deposited BST layer on SiO_2/Si annealed at 600°C and on several deposited layers (five layers) on SiO_2/Si and Pt/Cr/SiO_2/Si annealed at different temperatures. The critical angles of Si, Pt and BST are shown in table (4.1). The attenuation length is the depth into the material measured along the surface normal where the x-ray intensity falls to 1/e (∼0.37) of its value at the surface. The attenuation length was then 62 nm, i.e., the morphology of the top deposited layer was probed.

Materials	Critical angle $\alpha_c(°)$
Si	0.11
Pt	0.297
BST at 600°C	0.152

Table 4.1: Table presenting the critical angles for Si, Pt, and BST films at an X-ray energy of 16025 eV

One deposited layer

A kinetic study was conducted at 600°C in order to follow the morphology evolution as a function of the annealing time. Fig.(4.6) displays *ex situ* GISAXS images of one deposited BST layer on SiO_2/Si annealead at 600°C during different times from 5 min to 60 min. The scattering shape is quite similar for an annealing time from 5 min to 30 min.

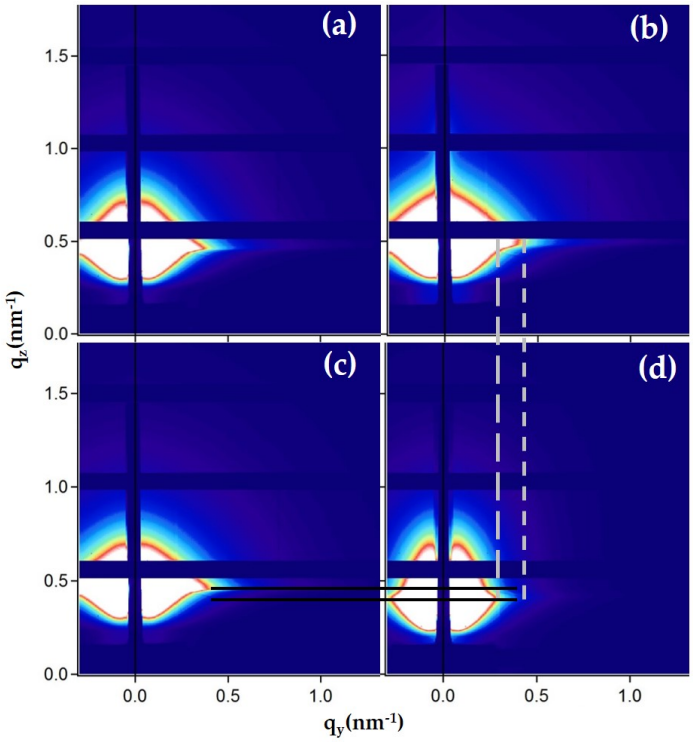

Figure 4.6: *Ex situ* GISAXS images of one deposited BST layer annealed at 600°C during (a) 5 min, (b) 15 min, (c) 30 min, and, (d) 60 min. The horizontal black lines indicate the intensity maximum (Yoneda peak) for 30 min and 60 min. Vertical lines are positioned at the yellow limit of the peak for 15 min (small dash), and 60 min (large dash).

In contrast, after an annealing of 60 min, the scattering shrinks along q_y indicating that the pores are wider in the direction parallel to the surface. In addition, there is an interference peak at $q_y \sim 0.074$ nm^{-1}, corresponding to a preferential distance D $\sim$ 85 nm between the pores, larger than that obtained at a low annealing temperature ($\sim$ 150°C). Hence, the preferential distance increases with the annealing temperature. The angle of total external reflection (Yoneda peak) is smaller for 60 min than for lower annealing times indicating that the film is less dense or more porous.

Fig. (4.7) depicts qualitatively the evolution of the organic and inorganic entities in the BST films. At 200°C, the solvent-rich and solvent-poor domains began to grow. After an annealing at 600°C, the organic species are completely gone and leave space to pores and the inorganic entities form particles. For an annealing time ranging from 5 to 30 min, the morphology of the pores and particles remains quite similar. When the annealing time is extended to 60 min, the distance between domains D $\sim$ 85 nm became larger in comparison with the lower annealing temperatures at 150°C. Thus, the pores became wider in the direction parallel to the surface according to the GISAXS observations.

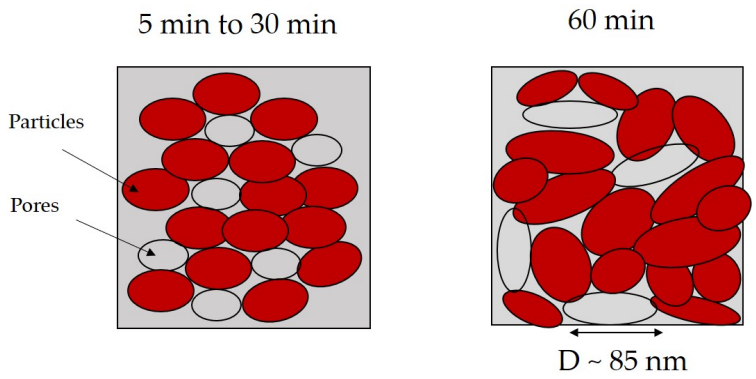

Figure 4.7: Schematic representation of the morphology evolution from 200°C to 600°C at various annealing times.

Several deposited layers

Five layers of BST were deposited and annealed at 600°C, 700°C, and 800°C. Fig.(4.8) displays the GISAXS images of the aforementioned BST thin films. The scattering from the pores is globally similar to that obtained for one deposited layer, indicating that the pores almost have the same shape and size. This means that the pores are delimited by particles, hence, there is no columnar growth.

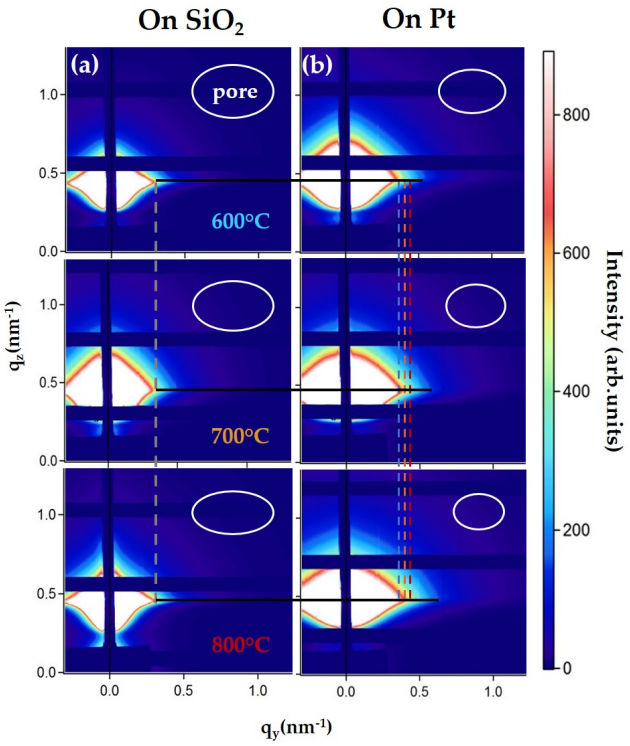

Figure 4.8: GISAXS images of five BST layers deposited on (a) SiO_2/Si or (b) on Pt and annealed at 600°C, 700°C, and 800°C. The horizontal black lines indicate the intensity maximum (Yoneda peak). The white ellipses correspond to a schematic representation of pores. For SiO_2/Si, the gray dashed line is positioned at the yellow limit of the peaks. For films deposited on Pt, the vertical dashed lines are positioned at the yellow limit of the peak at 600°C (blue), 700°C (orange), and 800°C(red).

Furthermore, the effect of the substrate was studied by probing the BST thin films deposited either on SiO_2/Si or on Pt/Cr/SiO_2/Si used for technological applications.
For deposition on SiO_2/Si, the scattering is relatively similar from 600°C to 800°C, meaning that the pores have a similar size. The scattering extension along q_z is larger than that along positive q_y, indicating that the pores have an oblate spheroid shape. Similarly for deposition on Pt, the pores have an oblate spheroid shape. As the annealing temperature increases, the scattering extends slightly further along q_z and q_y, indicating that the height of the pores and their radius slightly decrease respectively. Comparing the scattering extension for both substrates indicates that the pores are smaller in the case of films deposited on Pt.
The thermal expansion coefficient of $Ba_{0.7}Sr_{0.3}TiO_3$ ($10.5\times\ 10^{-6}\ °C^{-1}$) [27] is larger than that of Pt ($9\times\ 10^{-6}°C^{-1}$) and Si ($2.5\times\ 10^{-6}°C^{-1}$) [28]. During cooling, the substrate limits the BST layer contraction leading to a tensile stress in the layer. This stress can be at least partially relaxed by the pores, which adopt an oblate spheroid shape. The schematic of

Fig. (4.9) presents the annealing temperature and substrate effects on the pore morphology. For both substrates, pores adopted an oblate spheroid shape. When the annealing temperature increased from 600°C to 800°C, the pores did not undergo a major change for the BST films on SiO_2/Si. On the other hand, the pores dimensions decreased with higher temperatures for the BST films on Pt. This is mainly caused by the contraction of the films due to the tensile stress.

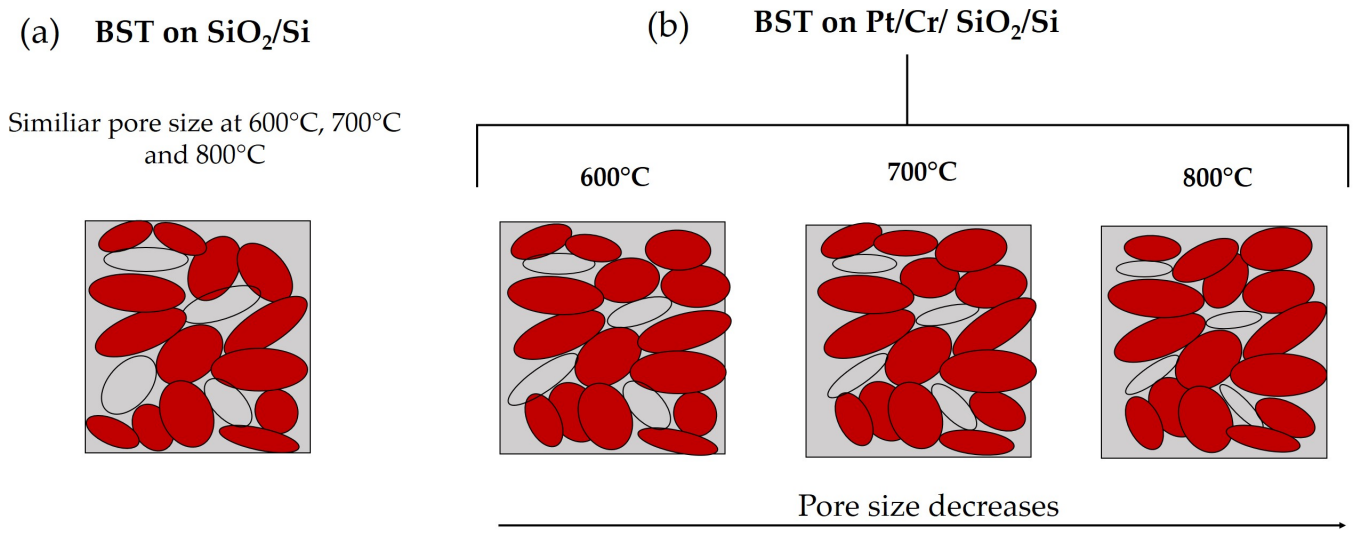

Figure 4.9: Schematic representation of the pore dimension and shape for (a) BST on SiO_2/Si and Pt/Cr/SiO_2/Si at different annealing temperatures.

4.3.3.3 Quantitative film porosity

Interestingly, GISAXS can be used to estimate the film porosity. In GISAXS, the intensity maximum (Yoneda peak) as a function of the out-of-plane angle occurs at the critical angle α_c for total external reflection. The material density ρ can be expressed as:

$$\rho = \frac{\Pi \alpha_c^2 \overline{M}}{r_e N_A (\overline{Z + f'}) \lambda^2}, \tag{4.1}$$

where M is the molecular weight, r_e is the classical electron radius, N_A is the Avogadro's number, Z is the number of electrons per atom, f' is the dispersion correction, and λ is the x-ray wavelength. The average molecular weight of $Ba_{0.7}Sr_{0.3}TiO_3$ is obtained from the sum of the relative atomic masses of each constituent element. The dispersion correction f' for a given element can be obtained from the x-ray interaction database [29]. The porosity

ϕ of the film is:

$$\phi = 1 - (\rho/\rho_0), \tag{4.2}$$

where ρ_0 is the bulk density of the $Ba_{0.7}Sr_{0.3}TiO_3$. This bulk mass density is obtained from that of $BaTiO_3$ (6.02 g cm^{-3}) and that of $SrTiO_3$ (5.11 g cm^{-3}). Hence, $\rho_0 \sim 5.747$ g cm^{-3} for bulk $Ba_{0.7}Sr_{0.3}TiO_3$.

Table (4.2) summarizes the GISAXS results for the five BST layers deposited on Pt. As the annealing temperature increases, the Yoneda peak shifts toward slightly larger angles α_c, indicating that ρ also increases, and, hence, ϕ decreases as shown in Table (4.2). In addition, the pore semi-axes decrease, which is in agreement with the decrease in ϕ. The pores have an oblate spheroid shape with an aspect ration [$(h/2)/r$] approximately equal to 0.5. The aspect ratio slightly increases as the annealing temperatures increases.

T(°C)	α_c(deg)	ρ [g cm^{-3}]	ϕ	r(nm)	$h/2$ (nm)	Aspect ratio
600	0.152	4.98	0.13	10	4.5	0.45
700	0.156	5.24	0.09	8.5	4	0.47
800	0.158	5.38	0.06	7	3.6	0.51

Table 4.2: Table presenting the critical angle α_c, material density ρ, porosity ϕ, semi-axes of the pores, namely, radius and half of the height, aspect ratio of the pores for the BST layers deposited on Pt and annealed at 600°C, 700°C, and 800°C.

Ex situ GISAXS summary

Kinetic study:

- This study puts in evidence the long annealing time necessary to remove the organic constituents in one thick deposited layer.
- Upon annealing at higher temperatures, the organic-rich domains become pores due to the evaporation of the organic constituents and the inorganic-rich domains become particles.

Substrate effect and pore formation:

- The pores adopted an oblate spheroid shape for both films on SiO_2 and Pt.
- For SiO_2, pores had similar sizes from 600°C to 800°C. In contrast, for BST films deposited on Pt, pore size decreased with the increasing annealing temperatures.
- Pores relaxed in an oblate spheroid shape due to the tensile stress in the BST films.
- Quantitatively, the porosity ϕ in BST films on Pt decreased from 0.13 to 0.06 with the increase of annealing temperature from 600°C to 800°C.

4.3.4 Structural study of BST films

The structure of BST thin films deposited on Pt was characterized by x-ray diffraction (XRD) on a Panalytical Empyrean diffractometer equipped with a Cobalt anode tube (Co $\lambda K\alpha$ = 1.789 Å). The incident optics were a fixed 1/4° divergence slit, Soller slits, and a 4 mm mask. Diffracted optics consisted of a parallel long plate collimator and a proportional one-dimensional detector.
The θ-2θ XRD spectrum of BST films annealed at 600°C, 700°C, and 800°C is shown in Fig.(5.3). The most intense peak corresponds to the (111) peak of Pt. This peak has a broad basis corresponding to small Pt crystallites. The other peaks are the (100), (110), (200), (210), and (211) peaks of BST. The BST films are crystallized in one phase, namely, the perovskite structure. There is no preferential orientation indicating that the films are

polycrystalline. The peaks of the BST films annealed at different temperatures are similar, meaning that the crystallinity does not significantly evolve above 600°C.

The cell parameters deduced from the XRD measurements are a = 3.95 Å and c = 3.99 Å, which are, respectively, slightly below and above the bulk parameter 3.974 Å [6]. The θ-2θ XRD scan probes the perpendicular direction to the surface. For the (100), (110), (200), and (210) peaks, the lattice vector $\boldsymbol{c}$ is aligned parallel to the surface corresponding to a flattened tetragonal structure. The tensile stress of the BST layers is also partially relaxed by the deformation of the grain structure.

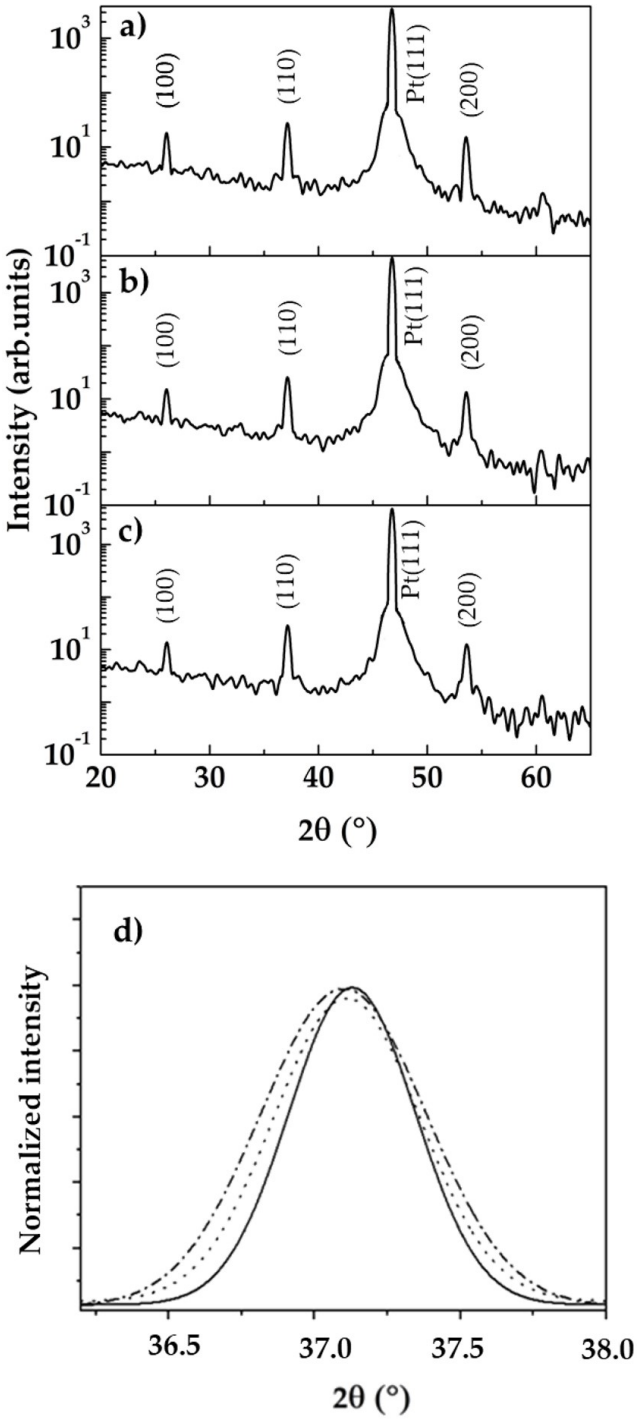

Figure 4.10: XRD pattern of sol-gel BST thin films annealed at: (a) 600°C, (b) 700°C, and (c) 800°C. (d) represents the (110) XRD peak at 600°C (full line), 700°C (dashed line), and 800°C (dotted line). The XRD patterns were identified using the ICDD PDF-4 database, reference (04-009-3218).

The grain size deduced by the Scherrer formula corresponds to the grains height. Full width at half maximum (FWHM) of the (110) peak yields $\sim$ 17 nm for the smaller crystallized grain height. The diffraction peaks slightly broaden as the temperature increases, indicating that a slight decrease in grain height occurs as the annealing temperature increases. This is coherent with the flattened tetragonal structure of the grains. For comparison, the grain height is larger than that of the pores. A height decrease was also observed for the pores as the temperature increases.

4.3.5 Morphology study and modeling

SEM was used to probe the morphology of the five layers of BST films on Pt annealed at 600°C, 700°C, and 800°C. Fig.(4.11) shows the cross-sectional SEM images of the aforementioned BST films. A high density of nanoparticles (NPs) is visible and the pores are delimited by particles in both directions parallel and perpendicular to the surface, i.e., there is no columnar growth.

Convection model

The morphology of the sol-gel BST thin films is explained by a convection model described here. The *in situ* GISAXS experiment puts in evidence the formation of columnar domains with different solvent fractions at the very beginning of film formation. Hence, let us consider the volume fraction of the solvent ψ from ψ_A (at point A) to ψ_B (at point B) as shown in Fig.(4.12). Points A and B are in two different solvent fraction regions. During evaporation, the volume fraction of the solvent decreases from ψ_d (down) at the bottom interface to ψ_u (up) at the free surface. The solution diffusion occurs from a region with a larger solvent fraction to a region with a smaller solvent fraction. The diffusion current in the film is written as follows:

$$W = D_{coop}(\psi_d - \psi_u)/(a^3 l), \tag{4.3}$$

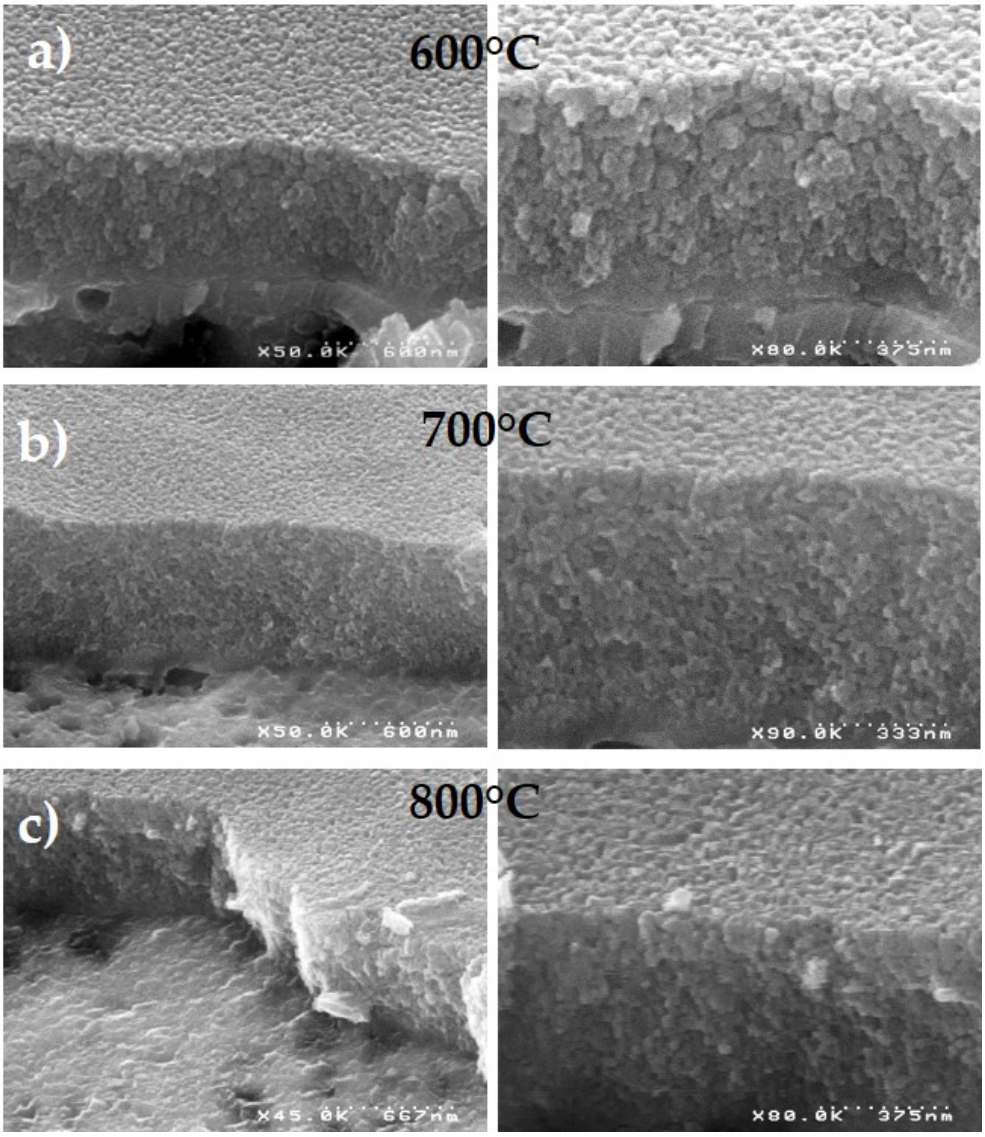

Figure 4.11: Cross-sectional SEM images of the BST layers on Pt at different annealing temperatures: (a) 600°C, (b) 700°C, and (c) 800°C. Left column: global view, and right column: more detailed view.

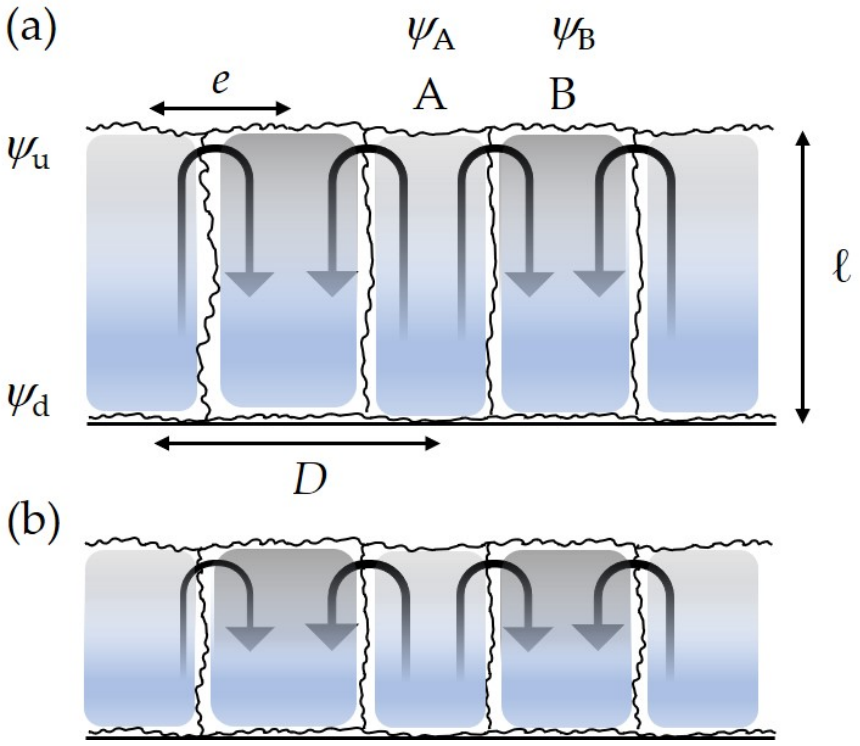

Figure 4.12: Schematic showing the occurrence of evaporation and convection loops depicted by black arrows in the film at low annealing temperatures. The inorganic and solvent fractions are represented by gray and blue shading respectively. The inorganic fraction slightly increases from bottom to top as well as from domain A to domain B. (a) depicts the beginning of the convective process and (b) the advanced process of evaporation and convection. The layer thickness decreases due to evaporation.

where D_{coop} is the cooperative diffusion of the solution, a is the size of a solvent molecule, and l is the film thickness.
An instability roll of lateral size e carries solvent from the larger solvent fraction at A to the lower one at B. The solvent motion occurs from bottom to top (near A) and from top to bottom (near B). Domain B corresponds to a particle nucleation site.
Combined diffusion and convection gives the following expression:

$$D_{coop}\frac{\psi_A - \psi_B}{e} \cong V(\psi_d - \psi_u), \tag{4.4}$$

where V is the roll velocity. This parameter is estimated by a balance between the surface forces and viscous stresses,

$$\frac{\gamma_B - \gamma_A}{e} \sim \frac{\eta V}{e}, \tag{4.5}$$

where γ is the surface tension and η is the solution viscosity. The difference in the surface

tension between point A and point B can be expressed as:

$$\gamma_B - \gamma_A = |\gamma'|(\psi_A - \psi_B), \tag{4.6}$$

where γ' = dγ/ dψ. Hence, the roll velocity becomes

$$V \sim \frac{|\gamma'|}{\eta}(\psi_A - \psi_B). \tag{4.7}$$

Furthermore, D_{coop} is proportional to the thermal energy kT and inversely proportional to the solvent viscosity η_s, as well as the typical size ξ in the solution,

$$D_{coop} = \frac{kT}{\eta_s \xi}, \tag{4.8}$$

Finally, the roll size e is

$$e \cong \frac{kT}{|\gamma'|\xi}\frac{\eta}{\eta_s(\psi_d - \psi_u)}, \tag{4.9}$$

At the beginning of annealing, the solution viscosity η is roughly that of the solvent η_s and the roll size becomes :

$$e \cong \frac{kT}{|\gamma'|\xi}\frac{1}{(\psi_d - \psi_u)} \tag{4.10}$$

The roll size increases with T, in agreement with the observed growth of domains at 150°C, 190°C, and 600°C by GISAXS. The characteristic size ξ is 7 nm from the GISAXS measurements and the parameter $|\gamma'|$ is found to be equal to 0.66 N/m by using the values of the surface tension of nano-sized $BaTiO_3$ and of isoamyl acetate. The roll size e is also equal to the size of a domain with a similar solvent fraction and is approximately half of the periodic distance D. Hence, the domain size and the periodic distance increase with T. After an annealing at 150°C, the observed roll size e of $\sim$ 7 nm corresponds to an extremely small difference between the solvent fraction at the bottom interface and at the free surface ψ_d - $\psi_u \sim$ 0.02%. Note that this beginning in phase separation between the solvent/ inorganic constituents is prior to any crystallization.
Furthermore, due to solvent evaporation, the film thickness decreases as follows:

$$dl/dt = -a^3 W. \tag{4.11}$$

Combining Eqs. (4.3) and (4.11), one gets:

$$D_{coop} = \frac{l(dl/dt)}{\psi_d - \psi_u}. \tag{4.12}$$

The time Δt corresponding to the decrease in the film thickness Δl is given by combining Eqs.(4.8) and (4.12):

$$\Delta t = \frac{\eta_s \xi}{kT} \frac{l \Delta l}{\psi_d - \psi_u}. \tag{4.13}$$

Let us note that l_i and l_d are the thicknesses of the initial and dry film respectively. By using $l = l_i$, $\Delta l = l_i$ - l_d, and $l_d = l_i \times x_{si}$ with x_{si} the initial solid fraction, Δt becomes:

$$\Delta t = \frac{\eta_s \xi}{kT} \frac{{l_i}^2 (1 - x_{si})}{\psi_d - \psi_u}. \tag{4.14}$$

The evaporation time is inversely proportional to the temperature and to the difference between the solvent fraction at the bottom interface and the free surface. The *ex situ* GISAXS measurements performed on one deposited BST layer on SiO_2/Si annealed at 600°C show that the evaporation should last at least 30 min, i.e., 1800 s in order to remove the organic compounds from the film. For an annealing time of 2000 s, for example, using η_s = 0.8 mPa.s, $l_i \sim 25$ μm, x_{si} = 0.07, one gets ψ_d - $\psi_u \sim 0.15\%$. With one final annealing at high temperatures, the annealing time necessary to remove the organic constituents is very long, as the evaporation time is proportional to the square of the film thickness.

Summary of the morphology and structure study.

- The BST thin films annealed at high temperatures crystallize in a polycrystalline perovskite phase with an average perpendicular grain size of $\sim$ 17 nm.
- No columnar growth was observed in BST films according to cross-sectional SEM and *ex situ GISAXS*.
- The convection and evaporation model explains film formation at low and high annealing temperatures.
- The model used an assumption of Fick's first law postulating that the diffusion flux goes from regions of larger solvent fraction to lower ones.
- The evaporation time is inversely proportional to the annealing temperature and proportional to the square of the film thickness, thus requiring long times to remove the organic components from the films.

4.4 BST thin film capacitor study

After having established the fundamentals of film formation at low and high annealing temperatures, an optimization of deposition and thermal annealing conditions has been performed. In addition, the electrical properties of BST films were investigated.
For this study, the samples were spin coated on $Pt/TiO_2/SiO_2/Si$ at 4000 rpm for 30 s and baked at 450°C for 5 min on a hot plate after each deposited layer. The samples were then annealed at 700°C for 1 min in a furnace under ambient air atmosphere after one deposited layer (1 L) or after two deposited layers (2 L). The thickness of the final film was approximately 440 nm measured by cross sectional SEM. Fig.(4.13) depicts the adopted high temperature annealing sequence for 1 L (Fig.4.13 (a)) and 2 L (Fig.4.13 (b)).

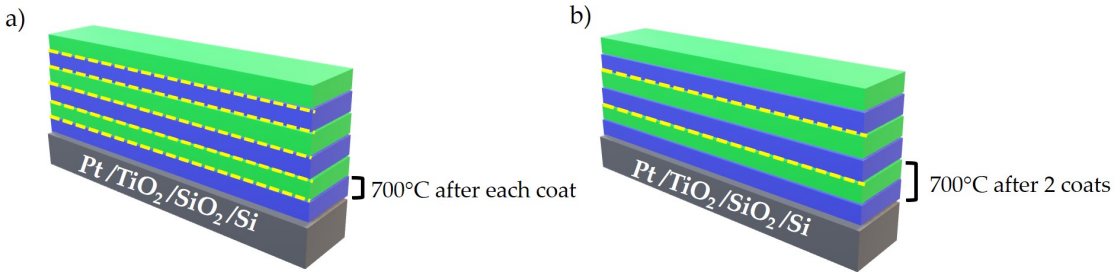

Figure 4.13: Schematic of the deposition and annealing sequence for (a) 1 L and (b) 2 L. The yellow dashes indicate the annealing step.

4.4.1 Morphology and structure

The morphology of 1 L and 2 L samples was probed using SEM. Fig.(4.14) shows the cross-sectional SEM images of BST films deposited on Pt and annealed at 700°C for 1 L and 2 L. The two annealing types correspond to two different morphologies. The 1 L annealing leads to a columnar growth, whereas the 2 L annealing leads to a granular growth.

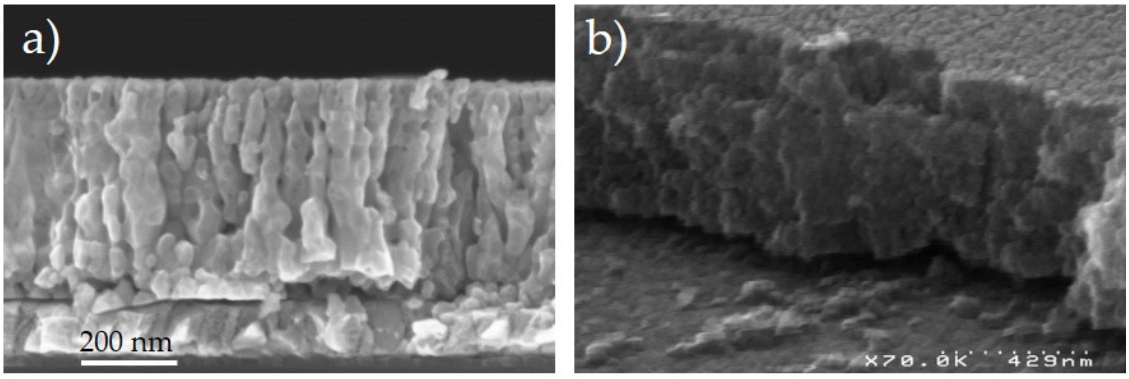

Figure 4.14: SEM images of (a) 1 L and (b) 2 L BST films deposited on $Pt/TiO_2/SiO_2/Si$ and annealed at 700°C.

In order to study the structure of the samples in question, θ-2θ measurements were conducted. The θ-2θ spectrum of the BST films after 1 L or 2 L annealing is displayed in Fig.(4.15). The XRD peaks previously observed in Fig.(5.3) are also present after 1 L or 2 L annealing. In Fig.(4.15), the shoulder on Pt (111) peak at the low angle side corresponds to BST (111). The spectra obtained after both annealing types are similar, whereas the growth morphology is different. This means that the XRD comes from grains with a similar size, whatever the 1 L or 2 L annealing. Hence, for 1 L annealing, the BST columns are made of several stacked crystalline grains. These grains are similar to those which are vertically shifted in the granular growth after 2 L annealing. The 1 L or 2 L annealing determines the growth morphology, but the crystalline structure of the grains remains quite similar.

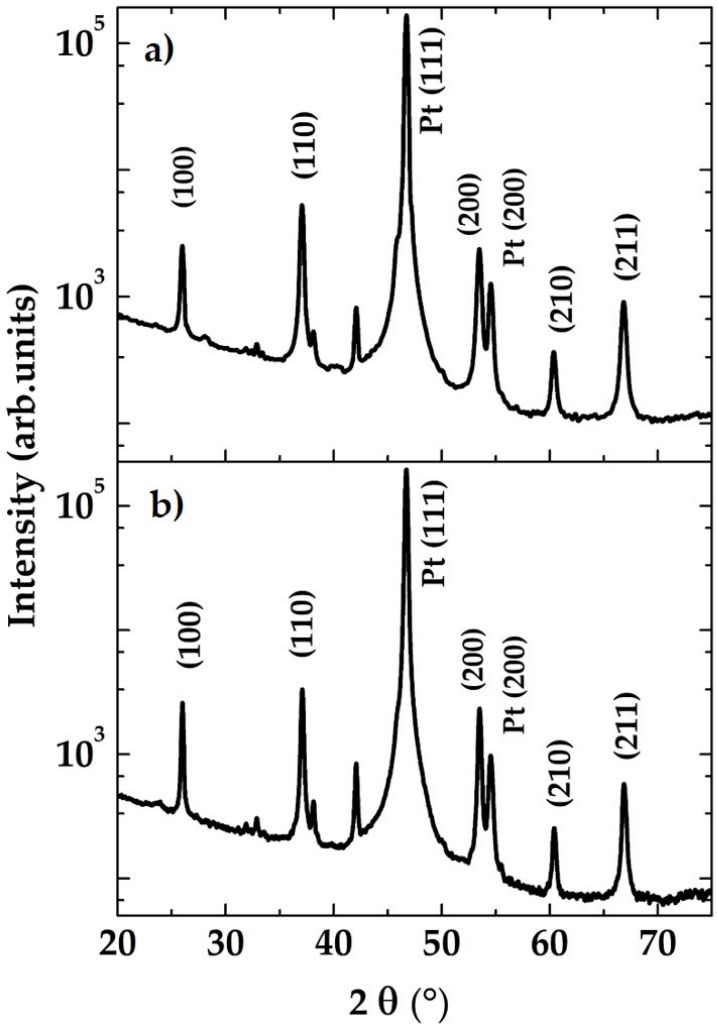

Figure 4.15: XRD spectra of BST thin films deposited on Pt and annealed at 700°C for (a) 1 L and (b) 2 L.

Morphology modeling

The convection model, discussed in previous sections, may also explain the difference in growth morphology according to the high temperature annealing types. Let us explain the granular growth observed for the 2 L annealing. The solution diffusion is initiated at the bottom of the additional deposited layer where the solvent fraction is larger, i.e., above the inorganic NPs, as shown in Fig.4.16 (a). For this reason, the diffusion flow brings the inorganic constituents laterally, shifted with respect to the particles in the previous layer. The final morphology obtained after the 2 L annealing at high temperatures is represented

in Fig. 4.16 (b).

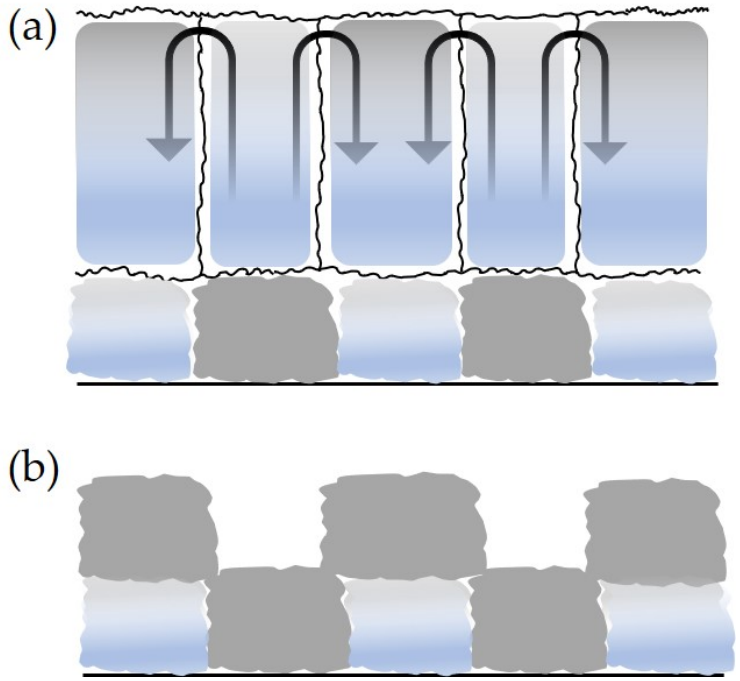

Figure 4.16: Convection-driven morphology of an additional deposited layer for 2 L annealing: (a) at the beginning of convection and evaporation for the additional layer and (b) at the end of this process and after annealing at high temperatures. The inorganic fraction is presented by the gray shading and the solvent fraction by the blue one.

On the contrary, for a 1 L annealing at high temperatures, a columnar growth is observed. The solution diffusion is initiated where the solvent fraction is larger, i.e., above the pores, as shown in Fig.4.17 (a). Thus, the diffusion flow brings inorganic constituents above the particles of the previous layer, resulting in the columnar growth. The final morphology obtained after the 1 L annealing at high temperatures is represented in Fig.4.17 (b).

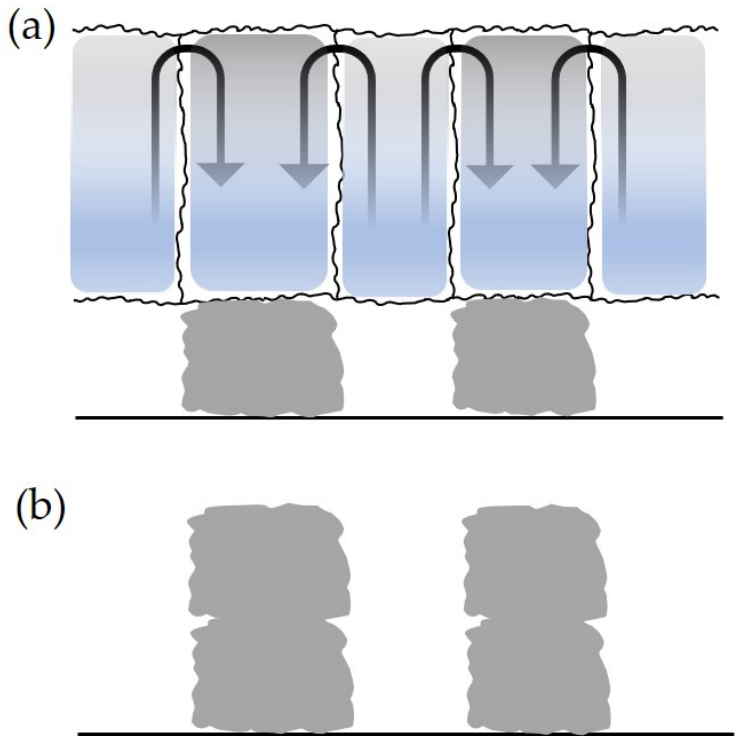

Figure 4.17: Convection-driven morphology of an additional deposited layer for 2 L annealing: (a) at the beginning of convection and evaporation for the additional layer and (b) at the end of this process and after annealing at high temperatures. The inorganic fraction is presented by the gray shading and the solvent fraction by the blue one.

Columnar growth summary

The growth type is not fundamentally linked to a thickness criterion, but to the amount of organic constituents left. Whatever the high temperature annealing types are, the deposition of additional layers occurs with heterogeneous nucleation.

4.4.2 Electrical properties

For the electrical measurements, electrodes of 200 nm thick Pt were deposited by evaporation onto the samples through a shadow mask to form BST thin film capacitors. The capacitance and dissipation factors in the range of 20 Hz-1 MHz were measured using the Agilent E4890A Precision LCR Meter. Hysteresis loops were measured using a Precision 10 kV HVI-SC from Radiante Technologies.

The dielectric constant and loss tangent were calculated using the following equations:

$$C = \frac{\epsilon_0\ \epsilon_r A}{d}, \tag{4.15}$$

$$tan\delta = \frac{1}{2\Pi C_p\ R_p f}, \tag{4.16}$$

where ϵ_r is the dielectric constant, ϵ_0 is the air permittivity (8.85$\times$ 10^{-12} F/m), A is the capacitor area (7.85 $\times$ 10^{-7} m^2), d is the thin film thickness (440 nm), C_p is the parallel capacitance (F), R_p is the parallel resistance (Ω), and f is the frequency (Hz) [30].
Fig. (4.18) shows the different electrical properties of the 1 L and 2 L thin film capacitors.

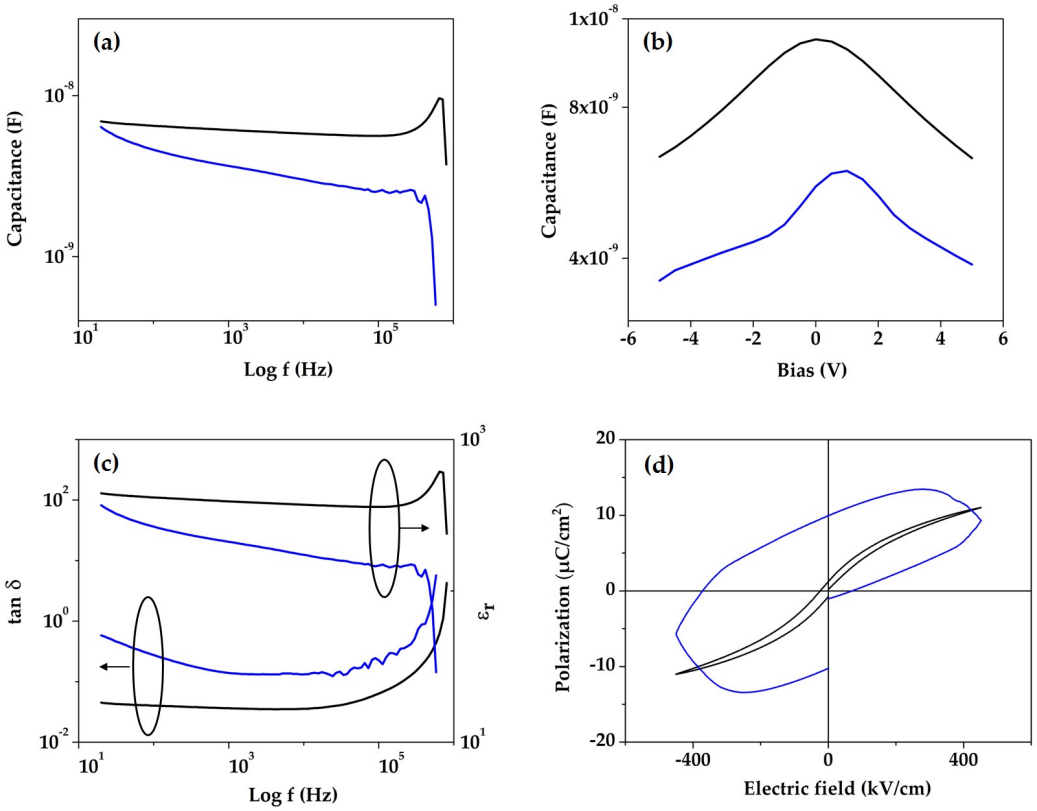

Figure 4.18: (a) Capacitance vs frequency, (b) capacitance vs voltage at 1 kHz, (c) dissipation factor and dielectric constant vs frequency, and (d) *P-E* hysteresis curve at 100 Hz. The 1 L annealing is represented in black and the 2 L in blue. The abnormality at 10^6 Hz is due to the machine limitation (20 Hz - 1 MHz).

The capacitance degradation in Fig.4.18(a) for the 2 L sample is due to the organic residues in the thin film structure in comparison to the 1 L sample, which presents good capacitive behavior for a BST capacitor. Fig.4.18(b) displays the capacitance as a function of voltage measured at 1 kHz for both samples. The 1 L sample has higher capacitance

values, higher dielectric constants, and a lower dissipation factor than 2 L, as shown in Fig.4.18(c). For example, at 10 kHz, the 1 L sample has a dielectric constant of 371 and a dissipation factor of ~ 0.035, and the 2 L sample has a dielectric constant of 178 and a dissipation factor of ~ 0.133. Hence, the electrical properties of BST thin films are improved for 1 L annealing. Compared to the work of Adikary et al.[8], the dielectric constant of the 1 L sample is divided by 2.2 and the dissipation factor is smaller by one order of magnitude.

Finally, Fig.4.18(d) displays the polarization-electric field measurements of the BST films at RT. The typical hysteresis loop of the 1 L sample indicates effective switching of the dipoles. The ferroelectric characteristics are remnant polarization of $\sim 1.2\ \mu C/cm^2$, a saturation polarization of $\sim 11\ \mu C/cm^2$ and a coercive field of 24 kV/cm. In contrast, the 2 L sample has no ferroelectric hysteresis loop. Actually, the *P-E* field curve may reveal polarization of space charge from organic constituents [31]. In the 2 L sample, organic constituents are left leading to a significant amount of ions. A high remnant polarization occurs due to the trapping of the ions on the electrode and a high field is required to extract them from the electrode, move them into the film, and decrease the polarization.

Electrical properties summary

- The remaining organic constituents are responsible for the poor electrical and non ferroelectric behavior observed in the 2 L sample.
- The 1 L sample yields good dielectric and ferroelectric properties.

4.5 Conclusion

The morphology of the sol-gel processed $Ba_{0.7}Sr_{0.3}TiO_3$ thin films was investigated. Prototype films were studied as a function of the annealing temperature at low temperatures (140°C-200°C) by *in situ* GISAXS and at high temperatures (600°C-800°C) by *ex situ* GISAXS. At $\sim$ 150°C, self-organized domains with a preferential distance of approximately 14 nm are formed. At high annealing temperatures, the growing domains become either nanoparticles or pores with a preferential distance of 85 nm at 600°C. This growth evolution is successfully explained by a general model based on convection and evaporation. With the increase of annealing temperatures, the characteristic lengths parallel to the surface increase due to convection and the perpendicular ones decrease due to evap-

oration. In addition, two types of annealing were investigated at 700°C. Annealing after two deposited layers (2 L) vertically shifted particles and no observed ferroelectric behavior. In contrast, annealing after one deposited layer (1 L) yields columnar growth and a ferroelectric hysteresis loop was obtained. The ferroelectricity of the sol-gel BST thin films is definitely linked to the complete removal of organic constituents. Thus, this work allow tailoring of sol-gel thin films at the nanoscale and development of cost-effective ferroelectric thin films on large surfaces.

References

[1] De Gennes, P. *The European Physical Journal E* **6**(1), 421–424 (2001).

[2] Batra, A. and Aggarwal, M. *Pyroelectric Materials: Infrared Detectors, Particle Accelerators and Energy Harvesters*. Press Monograph Series. SPIE Press, (2013).

[3] Nadaud, K., Borderon, C., Gillard, R., Fourn, E., Renoud, R., and Gundel, H. W. *Thin Solid Films* **591**, 90–96 (2015).

[4] Liou, Y.-C. and Wu, C.-T. *Ceramics International* **34**(3), 517–522 (2008).

[5] Taylor, T. R., Hansen, P. J., Acikel, B., Pervez, N., York, R. A., Streiffer, S. K., and Speck, J. S. *Applied Physics Letters* **80**(11), 1978–1980 (2002).

[6] Levasseur, D., El-Shaarawi, H., Pacchini, S., Rousseau, A., Payan, S., Guegan, G., and Maglione, M. *Journal of the European Ceramic Society* **33**(1), 139–146 (2013).

[7] Azim Araghi, M., Shaban, N., and Bahar, M. *Materials Science-Poland* **34**(1), 63–68 (2016).

[8] Adikary, S. U. and Chan, H. L. W. *Thin Solid Films* , 5 (2003).

[9] Budiawanti, S., Soegijono, B., and Mudzakir, I. *Journal of Physics: Conference Series* **985**, 012034 (2018).

[10] Gust, M. C., Momoda, L. A., Evans, N. D., and Mecartney, M. L. *Journal of the American Ceramic Society* **84**(5), 1087–1092 (2001).

[11] Bobby Singh, S., Sharma, H., Sarma, H., and Phanjoubam, S. *Physica B: Condensed Matter* **403**(17), 2678–2683 (2008).

[12] Chi, Q., Dong, J., Zhang, C., Wang, X., and Lei, Q. *Journal of Materials Chemistry C* **4**(20), 4442–4450 (2016).

[13] Zhang, L., Zhong, W.-L., Wang, C.-L., Zhang, P.-L., and Wang, Y.-G. *Journal of Physics D: Applied Physics* **32**(5), 546–551 (1999).

[14] Schwartz, R. W., Schneller, T., and Waser, R. *Comptes Rendus Chimie* **7**(5), 433–461 (2004).

[15] Pierre, A. C. *Introduction to Sol-Gel Processing*, volume 1. Springer US, (1998).

[16] Sette, D., Kovacova, V., and Defay, E. *Thin Solid Films* **589**, 111–114 (2015).

[17] Revenant, C., Benwadih, M., and Maret, M. *Chemical Communications* **51**(7), 1218–1221 (2015).

[18] Yang, L., Ge, D., He, X., He, F., Li, Y., and Zhang, S. *Thin Solid Films* **517**(17), 5151–5156 (2009).

[19] Revenant, C. and Benwadih, M. *Thin Solid Films* **616**, 643–648 (2016).

[20] Chahine, G. A., Blanc, N., Arnaud, S., De Geuser, F., Guinebretière, R., and Boudet, N. *Metals* **9**(3), 352 (2019).

[21] Babonneau, D. *Journal of Applied Crystallography* **43**(4), 929–936 (2010).

[22] Ma, W. *Applied Physics A* **96**(4), 915–920 (2009).

[23] Sheu, Y.-W. and Tu, C.-H. *Journal of Chemical & Engineering Data* **51**(5), 1634–1641 (2006).

[24] De Gennes, P. G. *Macromolecules* **14**(6), 1637–1644 (1981).

[25] Revenant, C., Leroy, F., Lazzari, R., Renaud, G., and Henry, C. *Physical Review B* **69**(3), 035411 (2004).

[26] Schaefer, D. W., Martin, J. E., Wiltzius, P., and Cannell, D. S. *Phys. Rev. Lett.* **52**(26), 2371–2374 (1984).

[27] Ban, Z.-G. and Alpay, S. P. *Journal of Applied Physics* **91**(11), 9288–9296 (2002).

[28] Zhang, L., Ichiki, M., and Maeda, R. *Journal of the European Ceramic Society* **24**(6), 1673–1676 (2004).

[29] Henke, B. L., Gullikson, E. M., and Davis, J. C. *Atomic Data and Nuclear Data Tables* **54**(2), 181 – 342 (1993).

[30] Salam, M. A. and Rahman, Q. M. *Fundamentals of electrical circuit analysis*. Springer, (2018).

[31] Kliem, H. and Martin, B. *Journal of Physics: Condensed Matter* **20**(32), 321001 (2008).

Chapter 5

Investigating the dilution effect on the morphological, structural and electrical properties of BST thin films

5.1 Introduction

In the previous chapter, the mechanisms governing BST film formation at low and high temperatures were discussed. The optimization of the deposition and thermal annealing conditions took place. A preferred columnar growth was observed for the one layer (1 L) annealing type, and this sample yielded better dielectric and ferroelectric properties.

Herein, we were interested in investigating the precursor solution dilution effect on the different properties of BST thin films. First of all, the columnar morphology, grain size and roughness of the diluted films were studied using SEM and AFM. The structure evolution of the BST thin films was investigated using XRD. An explanation of the grain size and roughness variation was proposed based on the convection and diffusion model. At last, the electrical properties of the diluted BST thin films were discussed.

5.2 Precursor solution dilution study

As discussed in chapter 4 , in sol gel processing, the growth can be granular or columnar according to the annealing efficiency in removing the organic species depending on the dilution/thickness of the deposited layer [1]. Schwartz et al.[2] found that for diluted solutions and sufficient annealing, the growth is columnar. Cheng et al.[3] studied $Ba_{0.8}Sr_{0.2}TiO_3$ thin films with several precursor solution concentrations (0.4 M, 0.1 M and 0.05 M). Then, Cheng et al.[4] studied the ferroelectric and pyroelectric properties of highly diluted $Ba_{0.8}Sr_{0.2}TiO_3$ thin films (0.05 M). A theoretical study was performed by Zhang et al.[5] on the dependence of ferroelectric properties as a function of grain height and width in columnar-grained $BaTiO_3$ thin films. For grain size smaller than 200-300 nm, most of the grains consist of single domains and do not have domain walls [6]. The observed polarization decrease is linked to the depolarization field associated to the charges at the material surfaces.
In this chapter, we are interested in studying even more diluted systems and investigating its effects on the microstructure and ferroelectric properties of $Ba_{0.7}Sr_{0.3}TiO_3$ thin films.

5.2.1 Diluted BST thin film preparation

The same $Ba_{0.7}Sr_{0.3}TiO_3$ sol gel commercial solution from chapter 4 is used in the preparation of the BST thin films with different solution concentrations.
Solutions with 0.032 M, 0.016 M and 0.008 M of the precursor solution were deposited onto a platinized silicon substrate Pt (100 nm)/TiO_2 (10 nm)/SiO_2 (500 nm)/Si (725 μm). The substrate was cleaned in acetone in an ultrasonic cleaner for 3 min prior to solution deposition. A spin coating scheme was used to deposit the BST solution with a clean glass syringe to avoid any contamination. The solutions were spun at 4000 rpm for 30s. No wetting problems were observed, the solution spread homogeneously on the platinized silicon substrate.
The edge of the as-deposited films was cleaned with a Q-tip dipped in isoamyl acetate giving access to the bottom platinum electrode, enabling the electrical measurements later.

Heat treatment

The as-deposited films were annealed at 450°C for 5 min on a hot plate in air for solvent evaporation and organic decomposition and then annealed directly at 700°C for 1 min in air using a furnace for film crystallization. The annealing cycle was repeated after each layer deposition to achieve the desired film thicknesses. The annealing time has been reduced to avoid Pt/TiO_2 diffusion in the active BST layer. This phenomenon can cause detrimental consequences on the electrical properties of the films.

Let us denote BST32, BST16 and BST8 the three thin film samples with 0.032M, 0.016M and 0.008M precursor concentrations respectively.

5.2.2 Diluted thin films morphology and structure

5.2.2.1 Morphology

SEM observations

The BST thin films with different solution concentrations were studied by SEM. The cross-section SEM views of Fig.(5.1) show the columnar morphology through the entire film thickness for the BST thin films. There is no visible amorphous layer along the electrodes. The film thickness was estimated from the cross-section SEM images and was reported in Table (5.1). By taking into account the number of deposited layers, the average layer thickness was calculated (Table 5.1).

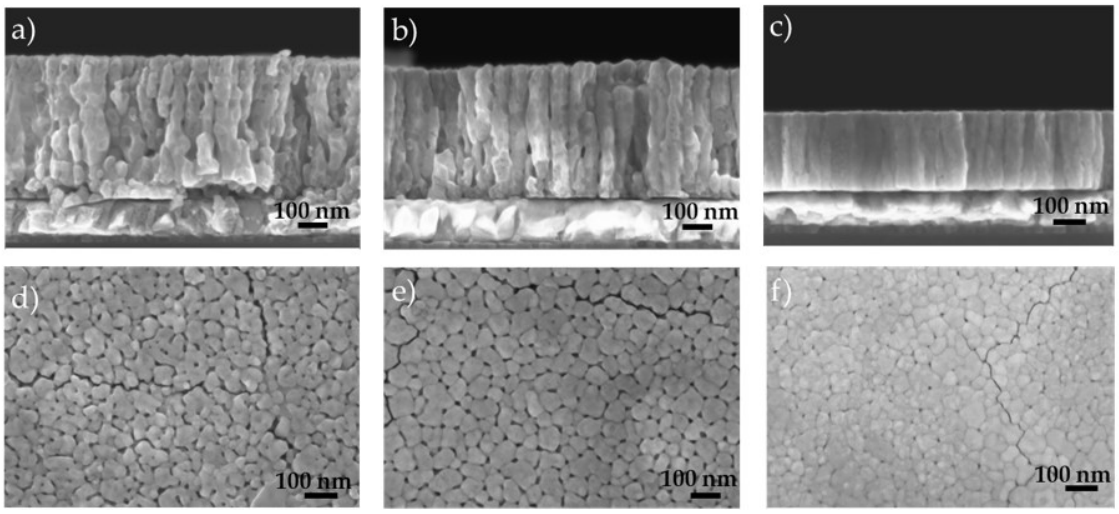

Figure 5.1: SEM images of BST thin films with different precursor concentrations: (a-c) cross section view and (d-f) surface view of BST32, BST16 and BST8 left to right.

For BST32 (Fig.5.1(a)), each column may not go from the film bottom to the free surface, i.e. several columns may succeed from the film bottom to the free surface and pores are visible between the columns, which may be slightly curved. Moreover, individual oblong grains can be observed in the columns. For BST16 (Fig.5.1(b)), the columns are straighter and taller compared to BST32. Some pores are also visible between irregular columns. For BST8 (Fig.5.1(c)), the columns can barely be distinguished and there are no large voids anymore. As the solution dilution increases, the thin film becomes more homogeneous and the surface roughness seems to decrease. Plane-view images in Fig.5.1(d-f) show the BST film surface. The grains may have curved shapes and are separated by numerous pores in BST32 sample (Fig.5.1 (d)). Intergranular cracks are visible probably

Samples	Number of deposited layers	Final film thickness (nm)	Average layer thickness Δ (nm)
BST32	8	443	55.4
BST16	15	390	26
BST8	20	250	12.5

Table 5.1: Table summarizing sample characteristics.

due to tensile stress originating from the mismatch of thermal expansion coefficient between the BST film and Pt. The grains are more regular and rounded in BST16 (Fig.5.1(e)). The grains may touch each other or be separated by pores. For BST8 (Fig.5.1(f)), the in-

dividual grains are smaller and coalesce. Pores when present are extremely small. The intergranular cracks are thinner than for the previous samples.
As dilution increases, the size of the pores and of the cracks decreases, the film becomes denser. The dilution has a clear impact on the morphology of the grains and of the film.

AFM results

AFM was used to investigate the grain size and the roughness of the thin films. The measurement was performed in tapping mode on the surface of the thin films in the range of 1 µm. The lateral grain size and the root mean squared roughness of the films were obtained using the Nanoscope analysis software. Fig.(5.2) displays the film surface observed by AFM as a function of the solution dilution. For BST32 (Fig.5.2(a)), the surface is not homogeneous and consists of a region with small dots and another one with stripes composed of aligned grains. For BST16 (Fig.5.2(b)), the region with individual dots increases. For BST8 (Fig.5.2(c)), the grains are clearly organized along lines. The grain width and roughness of the films are reported in Table (5.2). From BST32 to BST8, the average grain width increases by a factor of approximately 2 and the roughness decreases by a factor of 2.6.
As the precursor solution dilution increases, the average grain width increases and the surface roughness decreases. The increase of the grain width is coherent with the grain coalescence observed in SEM.

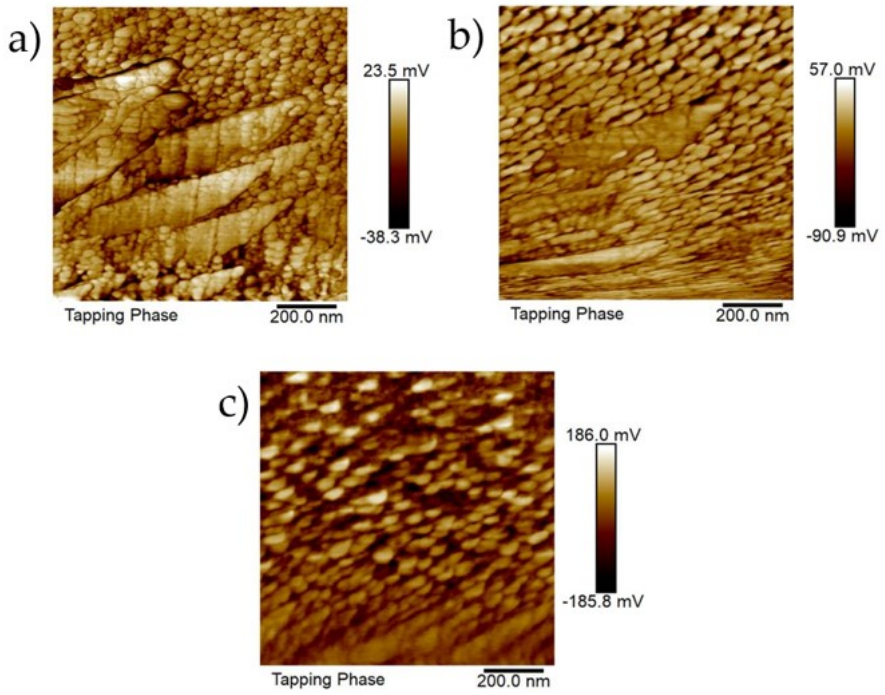

Figure 5.2: AFM images of a) BST32, b) BST16 and c) BST8.

Samples	Grain size (nm)	Roughness (nm)
BST32	58	12.9
BST16	119	9.5
BST8	121	5.0

Table 5.2: Grain width and roughness *Rms* of the BST thin films.

5.2.2.2 Structure

XRD measurements were conducted to investigate the crystallinity of the thin films. The measurement setup, incident, and diffracted optics are identical to those used in the previous chapter. Fig.(5.3) displays the θ-2θ XRD patterns for the thin films.

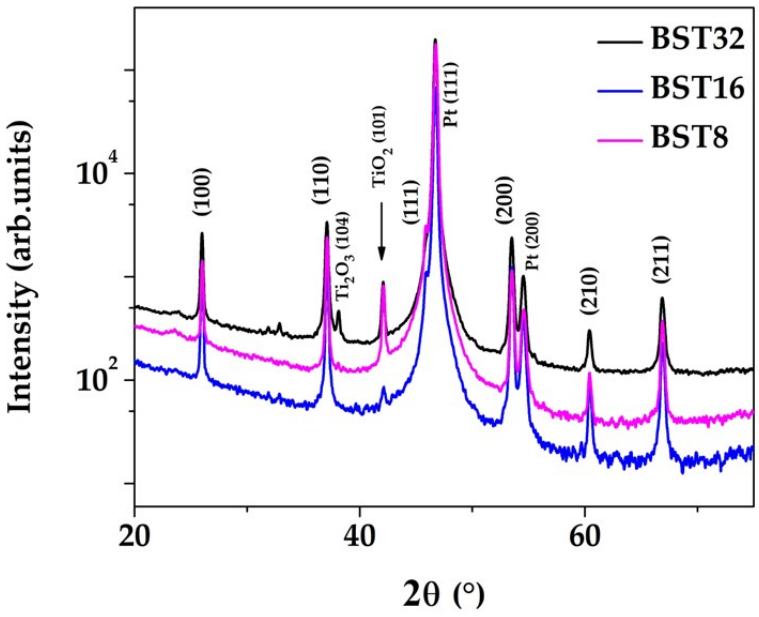

Figure 5.3: XRD spectra of the BST32, BST16 and BST8 samples.

The most intense peak belongs to Pt(111) present on the silicon substrate. The other peaks (100), (110), (111), (200), (210), and (211) indicate that the films crystallized in a polycrystalline perovskite phase of BST. The peaks (100), (110), (200), and (210) originate from particles with the lattice vector **c** aligned parallel to the surface. As the deposited layers are quite thin, the short time at high temperature is sufficient for crystallizing the thin films.

From the JCPDS card (04-019-7881 of the ICDD PDF-4 database), tetragonal symmetry was found for all the films. More precisely, the interplanar spacing d (Å) was calculated using Bragg's equation:

$$n\lambda = 2\, d\, sin(\theta). \tag{5.1}$$

and the lattice constants a and c are calculated using the equation for a tetragonal unit cell:

$$\frac{1}{d^2} = \frac{h^2 + k^2}{a^2} + \frac{l^2}{c^2}. \tag{5.2}$$

Table (5.3) displays the calculated lattice parameters from the XRD data. The lattice parameter a (resp. c) slightly decreases (resp. increases) as dilution increases. The lattice parameter a of the three films is slightly higher than the bulk value of BST (3.974 Å) [7]. As most of the particles have the lattice vector **c** aligned parallel to the surface, the tetragonality ratio of the films is calculated as a/c. It slightly decreases with the dilution increase.

Thus, the tetragonal structure evolves from a slightly elongated to a slightly flattened one. Indeed, the thermal expansion coefficient of BST (α_{BST} =10.5 $\times$ 10^{-6} °C^{-1}) is larger than that of Pt (α_{Pt} = 9$\times$ 10^{-6} °C^{-1}). Hence, the substrate limits the layer contraction during cooling after thermal annealing. The resulting tensile stress can be relaxed by the pores or by the lattice. As dilution increases, porosity decreases and the stress relaxation by the pores decreases. Thus, the tensile stress on the lattice increases. More precisely, the lattice parameter c (resp. a) increases (resp. decreases), as the dilution increases. As a consequence, the lattice volume V_L calculated in Table (5.3) slightly increases with dilution.

Samples	a(Å)	c(Å)	a/c	V_L(Å^3)
BST32	3.977	3.963	1.004	62.5
BST16	3.975	3.972	1.001	62.7
BST8	3.974	3.988	0.996	63.2

Table 5.3: Experimental lattice parameters and tetragonality ratio a/c of the BST thin films.

The (111) peak is the most intense for BST8, less intense for BST16 and weakest for BST32 for which there is only a shoulder at the low angle side of the Pt (111) peak. Hence, a qualitative comparison of the different (111) XRD peak intensity indicates that BST is more crystallized with (111)–oriented lattices in the BST8 sample compared to the others. In addition, the (211) peak is more intense for the BST8 sample compared to the BST32 one and similar to the BST16 one. In the (111) and (211) peaks, the out-of-plane direction corresponds to the diagonal of one or two tetragonal lattices. Crystallites tend to have grain boundaries (GBs) following dense planes like (100), (110), (210) [8]. The surface energy of $BaTiO_3$ (111) surface theoretically calculated by [9] is considerably larger than the calculated (011) or (001) surface energy [10]. Hence, the (111) and (211) grains are favored in the core region of the grains.

Grain height

Using Scherrer's equation, grain height is calculated as follows:

$$L = k\lambda/\beta cos(\theta) \tag{5.3}$$

where k is the Scherrer constant taken to be 0.9, β is the full width at half maximum (FWHM) of the XRD peaks and L is the crystallite size. Table (5.4) presents the perpen-

dicular grain characteristics of BST thin films.

Peak	Samples	FWHM β (°)	Grain height H (nm)	H/Δ
(110) BST	BST32	0.23	42.3	0.8
	BST16	0.2	48.6	1.9
	BST8	0.19	51.2	4.1
(211) BST	BST32	0.38	29.1	0.5
	BST16	0.33	33.5	1.3
	BST8	0.31	35.7	2.9
(101) TiO_2	BST32	0.23	43	0.8
	BST16	-	-	-
	BST8	0.15	68	5.4

Table 5.4: Perpendicular characteristics of the BST thin films. The grain height is obtained from the FWHM of the corresponding XRD (110), (211), and (101) BST peaks.

As dilution increases:

- The FWHM of the (110) BST peak decreases indicating a larger particle height.
- From BST32 to BST8, the (110) particle height increases from 42 to 51 nm.
- The ratio H/Δ increases.
- The (110) grain height corresponds approximately to one to four individual deposited layers.
- The roughness decrease makes coalescence possible, thus, particles higher than one deposited layer are obtained.
- (211) peak grain height varies from 29 to 36 nm, corresponding approximately from half to three individual deposited layers respectively.

Figure (5.4) illustrates the particle morphology (size and roughness) as dilution increases. It depicts a summarized scheme of the SEM, AFM and XRD results for the grain size, shape and roughness. As shown in Table (5.4), for the (110) BST peak, the particles are higher than for (211). Surface and GBs roughness decreases as the dilution increases.

In addition, Fig.5.4(b) shows the grain elongation parallel to the surface with the increase of dilution.

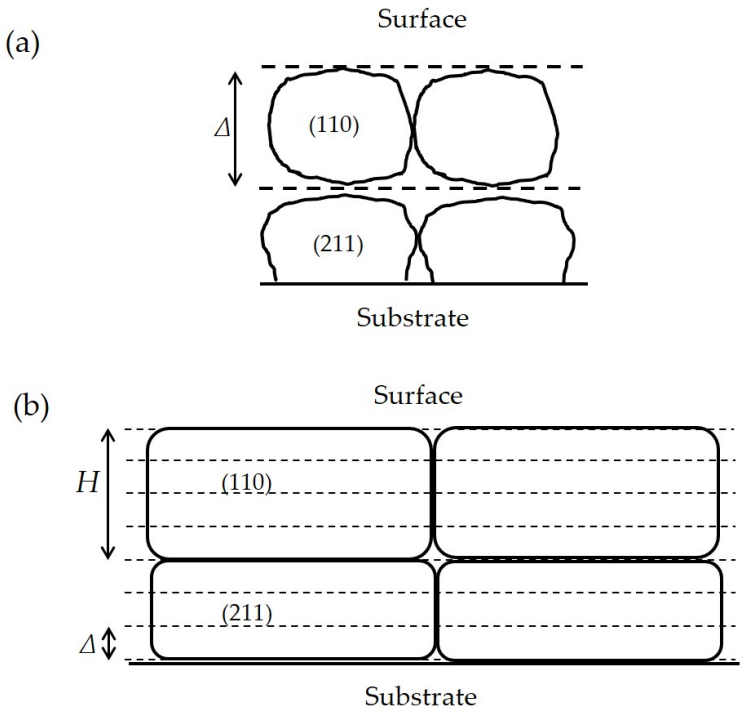

Figure 5.4: Schematic depicting particle morphology in the thin film as a function of dilution: (a) BST32 case, (b) BST8 case. For the sake of simplicity, only two crystallite rows are drawn.

The (101) TiO_2 peak is significant only for the BST32 and BST8 samples (Fig.5.5). From BST32 to BST8, the peak slightly shifts towards higher angles indicating that the distances in the out-of-plane direction decreases. This is coherent with the already observed increased tensile stress on the lattice as dilution increases. The n-type semiconductor TiO_2 acts as electron donors and leads to oxygen vacancies.

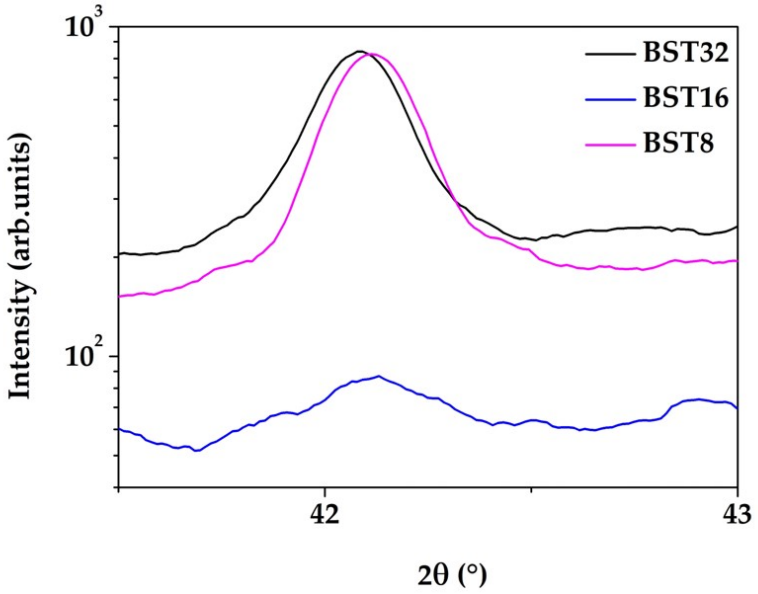

Figure 5.5: XRD spectra of the (101) TiO_2 peak for the BST32, BST16 and BST8 samples.

5.2.2.3 Roughness and grain size

The observed columnar growth is explained by the model based on diffusion and convection in chapter 4. To recapitulate, in the case of thermal annealing after each layer deposition, the solvent is fully evaporated. When a liquid film is deposited on an annealed layer, the solution diffusion begins where the solvent fraction is larger (the inorganic fraction is smaller) i.e. above the pores (in between the particles). Then, the convection flow brings inorganic constituents above the existing particles forming columnar growth.
Herein, we used this model to explain the change in roughness and grain size observed in the diluted thin films.

Surface roughness

When convection dominates over diffusion, the amplitude h of the surface undulations can be expressed as:

$$h \sim D_{coop}\, \eta \,/\, \gamma. \tag{5.4}$$

where D_{coop} is the cooperative diffusion coefficient, η the viscosity and γ the surface tension of the solution [11]. With increasing precursor dilution, the solution viscosity η de-

creases and the undulation amplitude h decreases. Hence, when dilution increases, the surface roughness decreases. This successively happens on the surface of each deposited layer. The film is made of a vertical succession of particles. For concentrated solutions, the surface of the successive deposited layers is rough, yielding pores between the layers. On the contrary, for diluted solutions, the surface of the successive deposited layers is smooth, yielding an homogeneous particle growth without any pores. In this case, the particles can easily coalesce along the direction perpendicular to the surface.

Columnar roughness and grain size

The previous expression of h on the top surface can be generalized at the particle side. The undulation amplitude around the particle boundaries varies as η. Hence, roughness at the top surface and at the column surface decreases as dilution increases. Moreover, the nanofluidic model allows obtaining the convective roll size e as:

$$e \cong \frac{kT}{|\gamma'|\xi} \frac{\eta}{\eta_s(\psi_d - \psi_u)}. \tag{5.5}$$

where k is the Boltzmann constant, T the temperature, ψ the volume fraction of the solvent, $\gamma' = \mathrm{d}\gamma/\mathrm{d}\psi$, ξ the typical size in the solution [1]. The subscripts d, u and s stand for down, up and solvent respectively.
When dilution increases:

- η and the roll size e decreases, which is in agreement with the decrease in grain size observed in the SEM plane-view.
- The column surface is smooth.
- The flow process can continue up to near contact between parallel columnar particles and lateral coalescence can occur between adjacent grains
- The average grain size increases due to possible coalescence.
- The film becomes densified without voids.

On the other hand, when dilution decreases:

- The column surface is rough.
- The flow process stops when no path is available anymore.

- Pores form and the film becomes less dense.
- Voids between the columns are present both in parallel and perpendicular directions.

The schematic in Fig.5.6 depicts the morphology change that occurs in the BST thin films as a function of dilution. The grain size and shape differences are shown along with the surface and columnar roughness as the dilution increases Fig.5.6 (a-c).

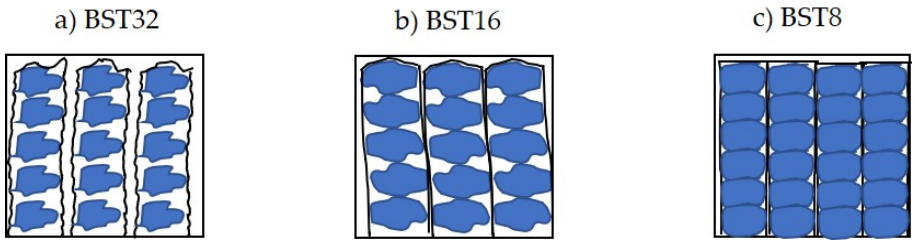

Figure 5.6: Schematic representation of the morphology evolution with the dilution for (a)BST32, (b) BST16 and (c)BST8.

Morphology and structure summary

With the dilution of the BST precursor solution:

- More homogeneous and dense films are obtained.
- Grain size (width and height) increases due to coalescence. Grain width is larger with an increase of a factor of 2 from BST32 to BST8.
- Surface and inner-columnar roughness decrease. Rms values increase by a factor of 2.6 from BST32 to BST8.
- The lattice parameters a and c become smaller and larger respectively.
- The lattice volume V_L increases.

5.3 Electrical properties

A metal-ferroelectric-metal (MFM) structure was achieved by depositing 100 nm of Pt thin films using ion beam evaporation at RT, through a shadow mask with a circular

diameter of 1 mm. This configuration is needed to conduct the electrical measurements of the BST thin films.

5.3.1 Dielectric properties

The dielectric measurements of the thin film capacitors were conducted in the range of 100 Hz - 1 MHz using the Agilent E4980A Precision LCR Meter. The capacitance was measured as a function of frequency from 10^2 to 10^5 Hz. The dielectric constant of the thin films was calculated from the capacitance using the following equation for a parallel plate capacitor:

$$C = \frac{\epsilon_0 \epsilon_r A}{\Delta_F}. \tag{5.6}$$

where ϵ_r is the dielectric constant, ϵ_0 is the vacuum permittivity (8.85 $\times$ 10^{-12} F/m), A is the capacitor area (7.85 $\times$ 10^{-7} m^2) and Δ_F is the thin film thickness. According to Fig.(5.7), the dielectric constant decreases as the frequency f increases, due to the dipole movement upon the application of an applied voltage [12]. According to the Curie-von Schweidler relaxation law, the dielectric constant varies as f^{n-1} with $0 \leq n \leq 1$ [13]. The crystallinity and the strain of the dielectric thin film are the main factors for the Curie–von Schweidler relaxation [13].

The dielectric constant of BST16 is similar to that obtained for BST32. On the contrary, the dielectric constant of BST8 is smaller than the previous ones. It has been reported in literature that the dielectric constant decreases due to the increased effect of an amorphous layer as the thickness of the film decreased.

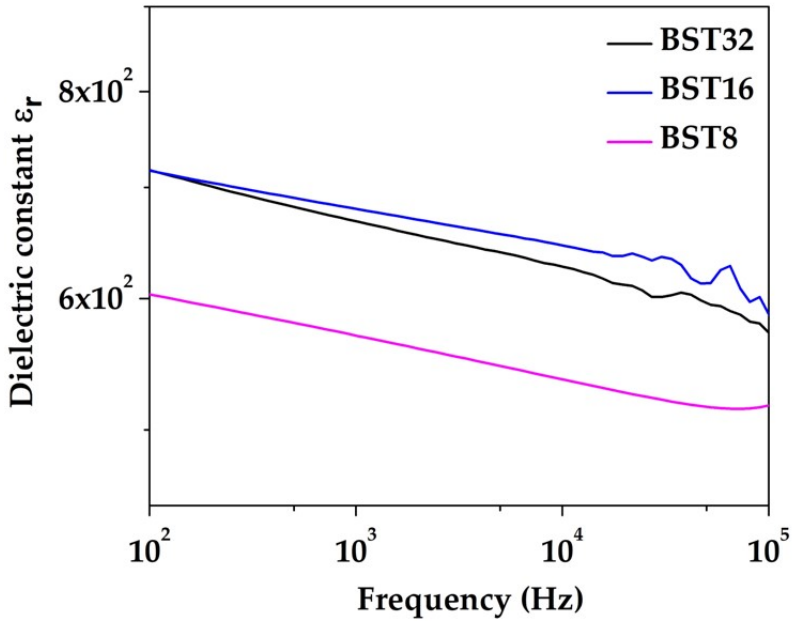

Figure 5.7: Relative permittivity vs frequency for the BST thin films.

Hwang et al. [14] proposed a partial depletion model with a very thin layer (approximately 1 nm) devoid of space charge at the interface with Pt electrode. This model explains the decreasing dielectric constant . Oh et al. [13] observed also that the dielectric constant of sputtered films increases due to the reduction of the interfacial dead layer effect as the thickness of the film increased. For films produced by PLD, Silva et al. [15] also observed a decrease in the dielectric constant in case of an amorphous layer at the interface between the metal electrode and dielectric film. Pecnik et al. [16] put in evidence that a reduced dielectric permittivity is linked to the tensile residual stress due to the thermal expansion mismatch between the film and the substrate. This stress could even lead to cracks.

Anyhow, in our case, the very first deposited layer was thermally annealed for all the samples in order to get crystallized and no amorphous layer was observed by SEM.

Frey et al. [17] proposed a model with ferroelectric grains having high permittivity ϵ_g surrounded by a grain boundary having lower permittivity ϵ_{gb}. The effective permittivity is expressed as follows:

$$\frac{1}{\epsilon_r} = \frac{v_g}{\epsilon_g} + g\frac{v_{gb}}{\epsilon_{gb}}. \tag{5.7}$$

where g is a factor describing the grain shape (g=0.8), v_g and v_{gb} the volume fraction of the core and of the boundary respectively.

For BST32, the SEM view shows that there are amorphous zones between grains in the

out-of-plane direction. From the SEM observations and from the ratio H/Δ for the high (110) BST peaks in Table(5.4), the volume fraction of the boundary is estimated to 20%. Similarly, for BST16, the volume fraction of the boundary is estimated to 5%. For BST8, no GBs are visible under/above the grains, but some GBs of a few nanometers wide are slightly visible on the lateral side of the grains. The GB width is estimated to $\sim$ 2 nm on each side and yields a boundary volume fraction of approximately 3%. The dielectric constant of GBs is fixed to 35% that of the grains like in the work of Zhang et al. [18].
For BST32, the experimental dielectric constant ϵ_r = 717 and the calculation with Eq. (5.7) yields ϵ_g =901. This ϵ_g value is used for the other samples and yield to ϵ_r values higher than the experimental ones (cf. Table 5.5(a)). Then, ϵ_g is fitted for every sample in order to get the experimental ϵ_r values (cf. Table 5.5(b)). The permittivity of the grains and of the GBs decreases as dilution increases. This may be explained by two main reasons. First, the crystallographic data show that the lattice volume increases with dilution. For a given sum of electric dipole moments, the polarization decreases if the lattice volume V_L increases. Thus, the dielectric susceptibility and the dielectric permittivity decrease. Second, the tetragonality decreases as dilution increases. This out-of-plane reduction of the lattice shrinks the distance between the center of charges in dipoles, decreasing the dipole moment and consequently the polarization. Hence, the slight decrease of the tetragonality ratio is another factor which explains the decrease of the dielectric constant.

	Samples	v_g	v_{gb}	ϵ_g	$\epsilon_{gb} = 35\% \ \epsilon_g$	ϵ_r
(a)	BST32	0.8	0.2	901	315	717
	BST16	0.95	0.05	901	315	847
	BST8	0.97	0.03	901	315	868
(b)	BST32	0.8	0.2	901	315	717
	BST16	0.95	0.05	762	267	716
	BST8	0.97	0.03	626	219	603

Table 5.5: Permittivity of the samples. The experimental values of ϵ_r are taken at 100 Hz. (a) The fit on ϵ_r is made for BST32 and yields ϵ_g which is used then for all the samples. (b) The fit on ϵ_r is made for each sample and yields ϵ_g.

5.3.2 Current density

The dc current of the films was measured at RT up to a voltage of 5 V with the step-voltage technique with a step of 50 mV. Fig.(5.8) displays the dc current of the films as a function of the voltage. Globally, the current density decreases as the solution dilution increases. This is due to a resistivity increase because of larger grains, i.e. a smaller density of GBs and hence less possible electric paths. In earlier studies, leakage current and conduction mechanisms in thin films such as BST are usually attributed to electrode-film interface effects [14, 19].
In the case of this study, the observed decrease in current density is attributed to the roughness, GB density and void decrease. Among the possible conduction mechanisms, the Space-Charge Limited Conduction (SCLC) is possible [20]. In addition, some works put in evidence the important role of oxygen vacancies which provide n-type carriers (electrons), giving rise to electronic conduction in BST [21–23]. At very low voltage, the current J varies linearly with V indicating ohmic conduction. This behavior was already observed for example by Silva et al. [15] and mentioned by Chiu [20]. This current is due to mobile electrons in the conduction band or holes in the valence band.

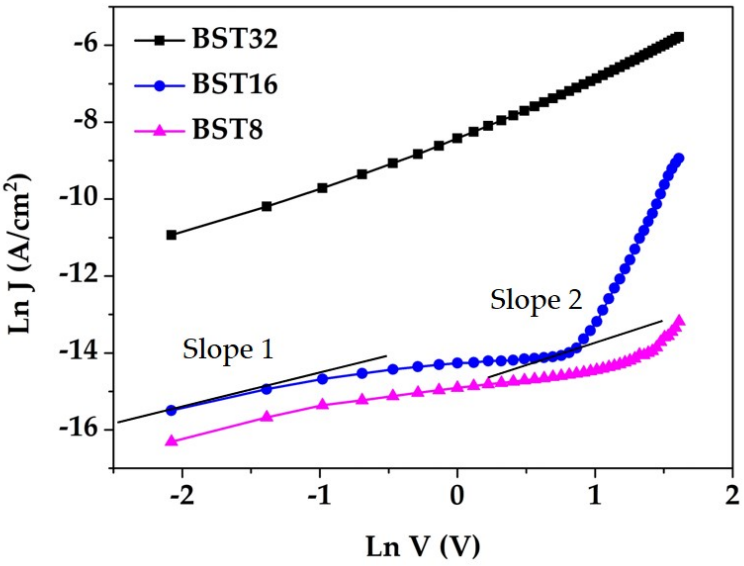

Figure 5.8: Ln J - Ln V plot for BST thin films.

The current curve for BST16 is different from that for the other samples. The current for BST16 increases significantly at medium and high voltages in contrast to the other samples. This is characteristic of SCLC [24]. After the ohmic conduction with J propor-

tional to V, the current density J is proportional to V^2 as shown in Fig. (5.9).

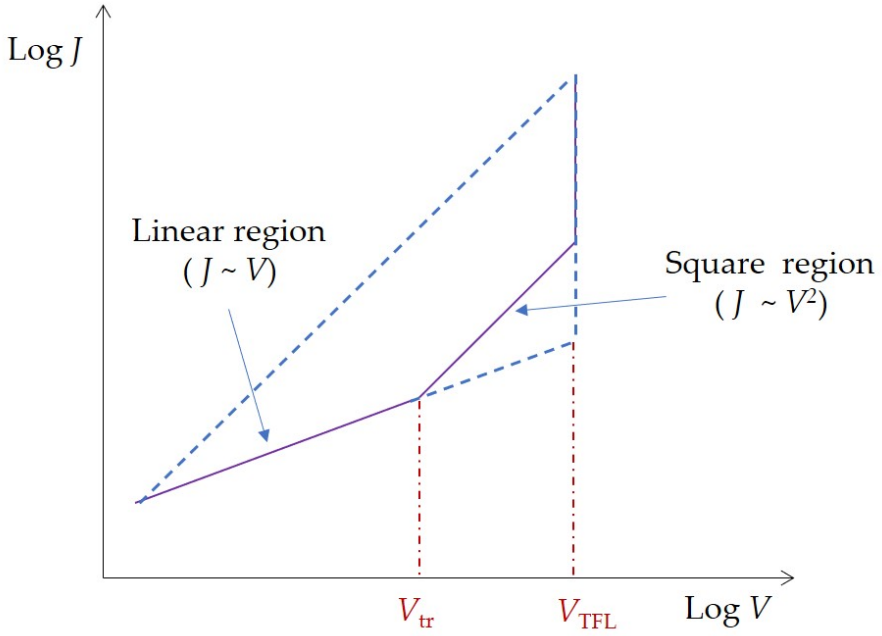

Figure 5.9: Current density curve characteristic of SCLC adapted from Chiu et al. [20].

The plot Ln(J) vs Ln(V) displayed in Fig.(5.8) shows that the slope is approximately 2 from the transition voltage $V_{tr} \sim 0.629$ V to the trap-filled limit voltage $V_{TFL} \sim 0.965$ V. The density of trapped electrons is then [20]:

$$N_t = \frac{2}{e}\epsilon_r\epsilon_0\frac{V_{TFL}}{d^2}. \tag{5.8}$$

One finds $N_t \sim 5.2 \times 10^{17}$ cm^{-3}. This value is in the same range as N_t for polycrystalline La_2O_3 [24]. Once all the traps are filled up, the injected electrons are free to move in the film and the current increases rapidly. The traps correspond to defects for example to oxygen vacancies. For the other samples BST32 and BST8, the TiO_2 grains are larger and may yield more electrons and oxygen vacancies. For these samples, the traps may not be filled in the explored voltage range.

5.3.3 Poling of the BST diluted thin films

Poling is the process by which an electric field is applied to the ferroelectric material usually below the Curie temperature T_C. Dipole moments are present in the crystalline

grains below T_C, but they may be randomly oriented, thus no overall polarization is observed. Fig. 5.10 (a) shows the initial state of the randomly aligned domains. After applying the electric field, the domains line up along directions nearly parallel to the electric field as depicted in Fig. 5.10 (b). After removing the electric field, the domains stay locked in the configuration of near alignment. Thus, the ferroelectric element have a permanent net polarization and a remnant polarization (Fig. 5.10 (c)) [25, 26]

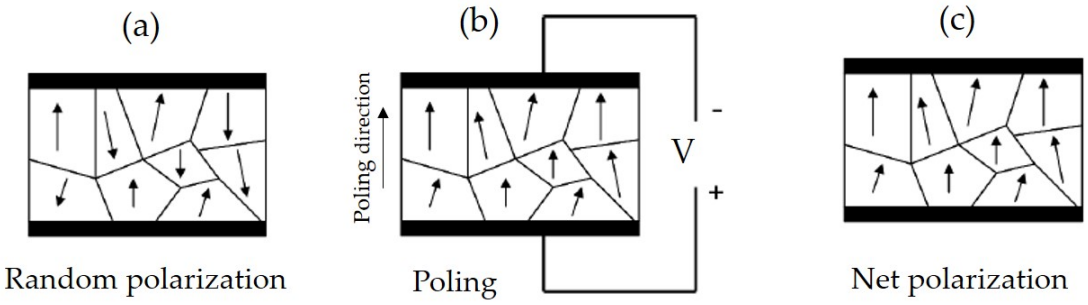

Figure 5.10: Schematic showing the poling process of the ferroelectric element.

In practice, the mechanisms of poling in thin films are quite complex. There is not a single rule that applies to all ferroelectric materials. Two major factors are crucial for the poling process of the dielectric material: the dielectric strength and the dielectric loss.

By definition, the dielectric strength of a material is the electric field strength at which electrical breakdown occurs. The electric field is caused by a voltage difference applied across the material. The voltage required to cause breakdown in a given material is called the breakdown voltage. In a parallel plate capacitor, the electric field E is proportional to the voltage difference V divided by the thickness D of the dielectric, so the breakdown voltage V_b is proportional to the dielectric strength E_d and the thickness $V_b = D\,E_d$.
I-V measurements in Fig. (5.11) show the limit of applied voltage for the three BST samples. Above this voltage, electrical breakdown will occur.

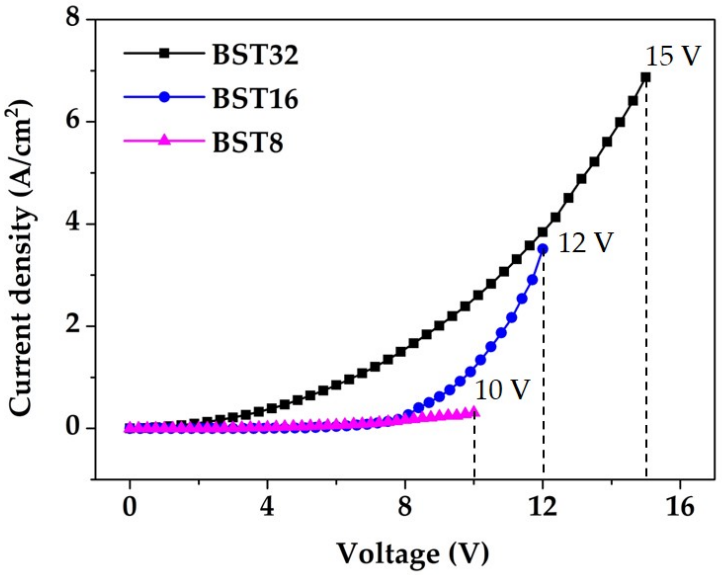

Figure 5.11: Current density curve showing the breakdown voltage for each BST sample.

It is important to consider losses in the dielectric before the poling process. Dielectric loss is due to the movement of atoms or molecules in an alternating electric field. It is dependent on frequency and on the dielectric material. One way of describing dielectric losses is to consider the permittivity as a complex number defined as :

$$\epsilon = \epsilon' - j\epsilon'' = |\epsilon|\, e^{-j\delta}. \tag{5.9}$$

where ϵ' is the real part of the permittivity, ϵ " is the imaginary part and δ is the dielectric loss angle. The dissipation factor or loss tangent tan δ is usually expressed as:

$$tan\ \delta = \frac{\epsilon''}{\epsilon'}. \tag{5.10}$$

The poling frequency can be estimated from the dissipation factor curve. For a capacitor, the loss tangent tan δ can be calculated from the capacitance measurements using the following equation:

$$tan\ \delta = \frac{1}{2\pi f C_p R_p}. \tag{5.11}$$

where C_p is the parallel capacitance, R_p is the parallel resistance and f is the frequency. Fig. 5.12 shows the variation of the dissipation factor as a function of frequency for the three BST diluted samples.

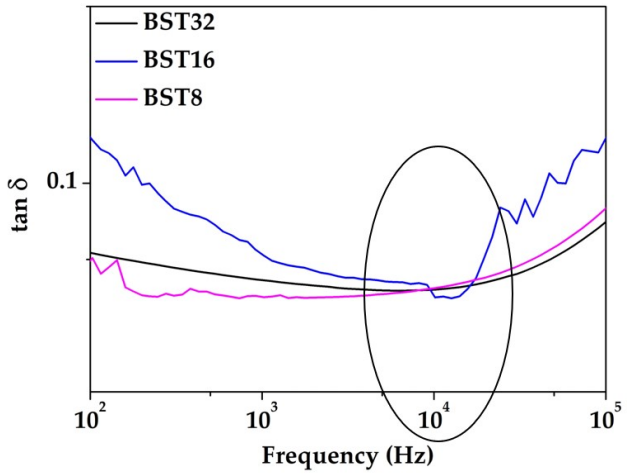

Figure 5.12: Dissipation curve for the three BST diluted samples.

One can estimate the adequate poling frequency from the lowest value of the loss tangent. For that value, the capacitor shows the least losses. The frequency range with the least dielectric loss is around 10^4 Hz for the BST thin film capacitors as shown in Fig. (5.12) [27].

Poling protocol

After gathering up the necessary data on the dielectric behavior in the ac regime, we can proceed to the actual poling of the BST capacitors. Fig. (5.13) summarizes the poling protocol used for the electrical poling of the BST thin film samples. The key parameters of the poling process are:

- The poling voltage.
- The poling frequency.
- The poling time.

We started with low voltages because electrical leakage significantly depends on voltage. At low voltage, lower frequencies and longer times can be applied since there is no risk of breakdown. Once the voltage increases, higher frequencies are applied to prevent the dielectric breakdown near high voltages. The dipoles respond more easily at low frequencies, this is why we start at lower frequencies and then we increase it slowly. As shown in the *tan* δ curves displayed in Fig. (5.12), there is high leakage at low and high frequencies.

Hence, to correctly align the dipoles, one avoids working in these frequency conditions. The time factor is the least important of the three key parameters of poling. Once, some dipoles are well aligned, the time factor becomes relevant and more time is needeed to align as much dipoles as possible. Table (5.5) summarizes the parameters used in the process of poling and Fig. (5.14) shows the evolution of the hysteresis loop with increasing voltage.

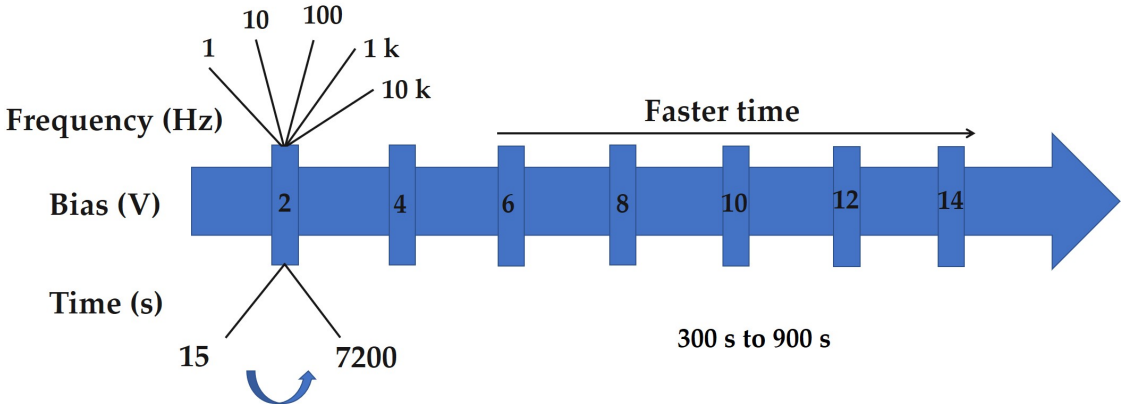

Figure 5.13: Schematic depicting the protocol employed for BST thin films poling.

Voltage (V)	Frequency (Hz)	Time (s)
2	7000	1800
4	7000	900
6	8000	600
10	11000	300
15	11000	1800

Table 5.5: Poling conditions for BST thin films at RT.

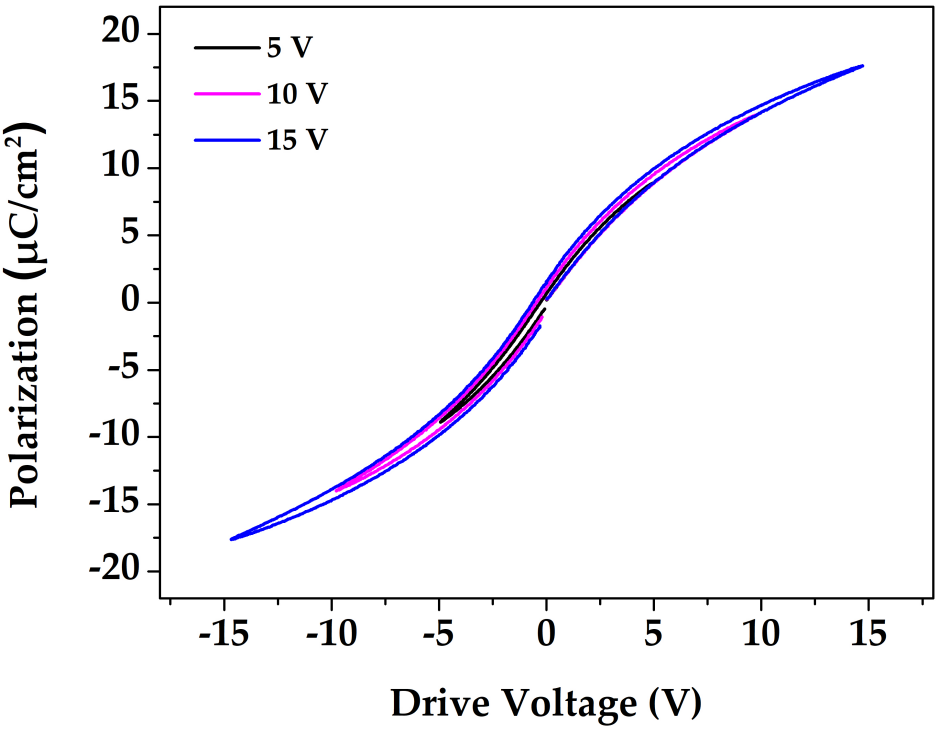

Figure 5.14: Hysteresis loop evolution with the poling voltage measured at 1 kHz for BST8 sample.

Grain size and poling voltage

Fig. (5.15) shows the poling voltage and electric field as a function of grain width for a polarization P= ± 5 μC/cm^2. The poling voltage and the electric field decrease with increasing grain width indicating that the samples with wider grains are easier to pole. The film with the largest grain width (BST8) was poled with the lowest electric field. For grains with limited effect of GBs, the polarization dynamics is dominated by 0° to 180° polar reorientation. On the contrary, for narrower grains with an increased effect of the GBs, nucleation sites may lead more easily to polar reorientation in the grain. There is a higher probability of non-180° domain switching. The GBs may induce depolarization field [5]. This may explain why the wider grains are easier to pole.
Moreover, according to the work of Wu et al. [28], some planes like (111) are stable during/after poling. The stability comes from the equivalence of the three axes with respect to the poling axis, assuming that the tetragonality is small. On the contrary, other planes are not stable and may switch to other orientations due to the poling effect. In our case,

according to the XRD results, the (111) grains are larger as dilution increases. At least for these planes, no poling voltage is needed for polarizing these grains. Hence, the poling voltage was decreased by increasing the grain width by diluting the precursor solution. By increasing the grain width by a factor of 2, the poling voltage was decreased by a factor of 2.3.

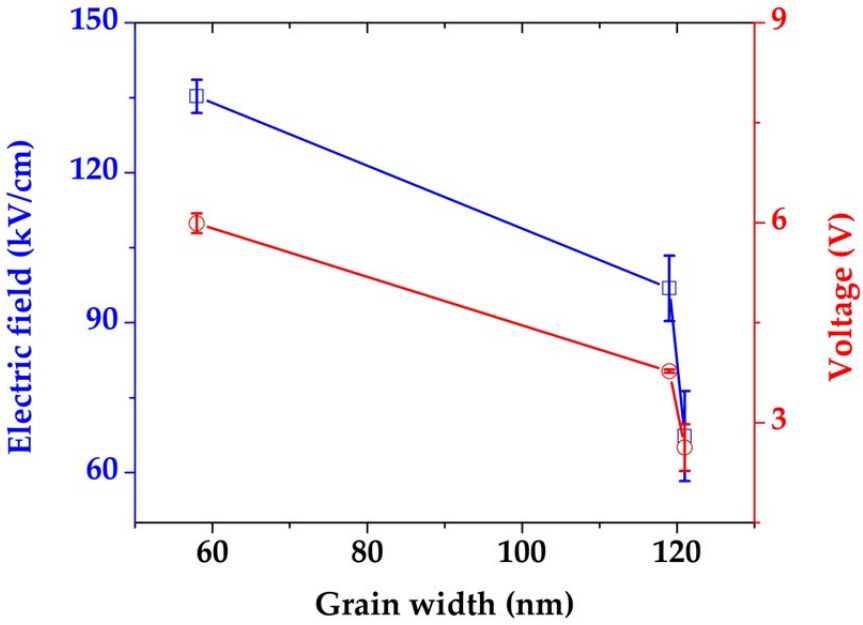

Figure 5.15: Poling characteristics as a function of grain width: electric field (blue) and voltage (red) at a polarization $P = \pm\ 5\ \mu C/cm^2$.

5.3.4 Ferroelectricity vs structure

5.3.4.1 Capacitance vs Bias

Fig. (5.16) displays the capacitance variation with the applied voltage. The measurements were carried out at RT with a step voltage of $\pm$ 0.5 V from -5 V to 5 V at 1 kHz. The shape of the *C-V* curves indicates the presence of a switching polarization with the applied voltage. The capacitance increases and the peaks get sharper with dilution. Moreover, there is a slight shift of the *C-V* curve for the BST8 sample towards higher voltage, confirming a spontaneous polarization.

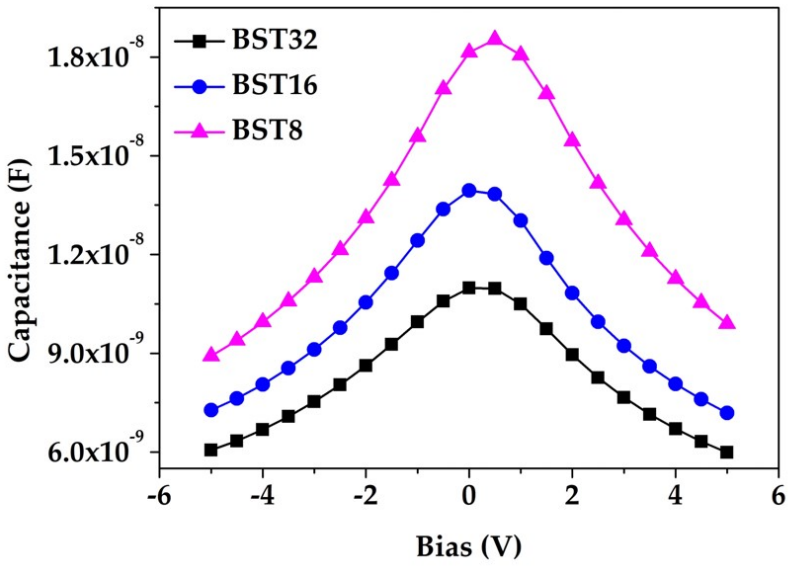

Figure 5.16: Capacitance vs bias for BST thin films measured at RT with a step voltage of $\pm$ 0.5 V at 1 kHz as a function of precursor solution dilution.

5.3.4.2 Polarization-field hysteresis loop

The polarization-electric field (*P-E*) hysteresis loop measurements were performed using a Precision 10 kV HVI-SC from Radiant Technologies at 1 kHz. Fig.(5.25) displays the characteristic polarization-voltage hysteresis loop for the BST thin films. All the samples exhibit a ferroelectric behavior. The saturation polarization P_S is 7.1, 10.4 and 14 μC/cm^2 for BST32, BST16 and BST8 respectively. The remnant polarization P_r is 0.47, 1.06 and 1.08 μC/cm^2 for BST32, BST16 and BST8 respectively. The slim hysteresis loop with high saturated polarization and low remnant polarization is typical of a ferroelectric relaxor [29]. The increase in remnant polarization can be attributed to the larger grain size in the thin films [3, 30]. In fact, conventional ferroelectric materials exhibit a high P_r while the latter is much lower for a relaxor ferroelectric. This is due to the presence of polar nano-domains. In addition, the hysteresis loop is not very open for a relaxor (i.e. a very weak coercive field E_C). For a classical ferroelectric, when increasing the temperature, the ferroelectric properties decrease until they disappear at T_C. On the other hand, the ferroelectric properties of relaxor ferroelectrics persist beyond T_C. The reason is the presence of nano-polar regions beyond T_C which means that a local dielectric order exists. However, the polarizations are randomly oriented so no spontaneous polarization is present

and no ferroelectric phase exists anymore. If an electric field is applied beyond the Curie temperature, then a ferroelectric phase is induced, but it is not stable. It will disappear, in a more or less short time, when the electric field is removed [31, 32].

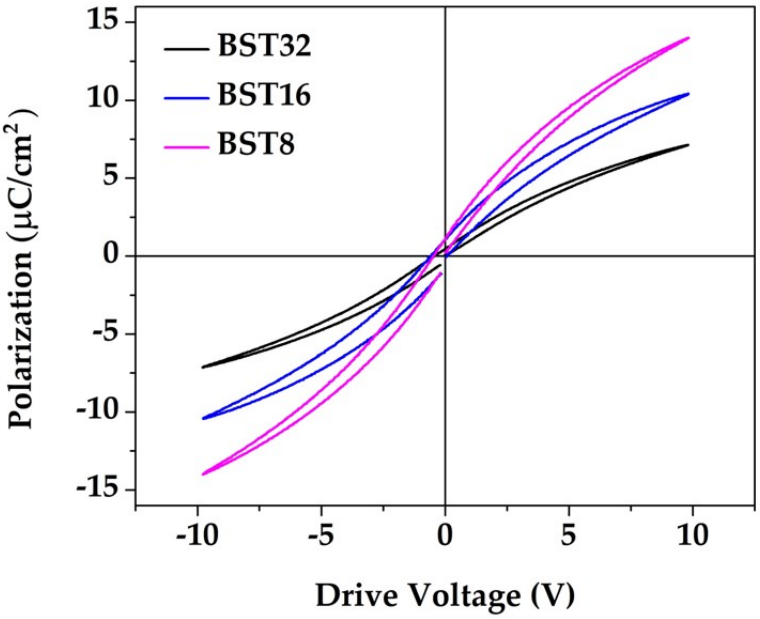

Figure 5.17: Polarization vs voltage for the BST films at RT at 1 kHz.

Fig. (5.18) displays the saturation polarization P_S and the remnant polarization P_r as a function of the grain size. Both P_S and P_r increase with the grain width. The increase of P_S and P_r with the grain width is in agreement with a theoretical study on columnar-grained $BaTiO_3$ thin films [5].

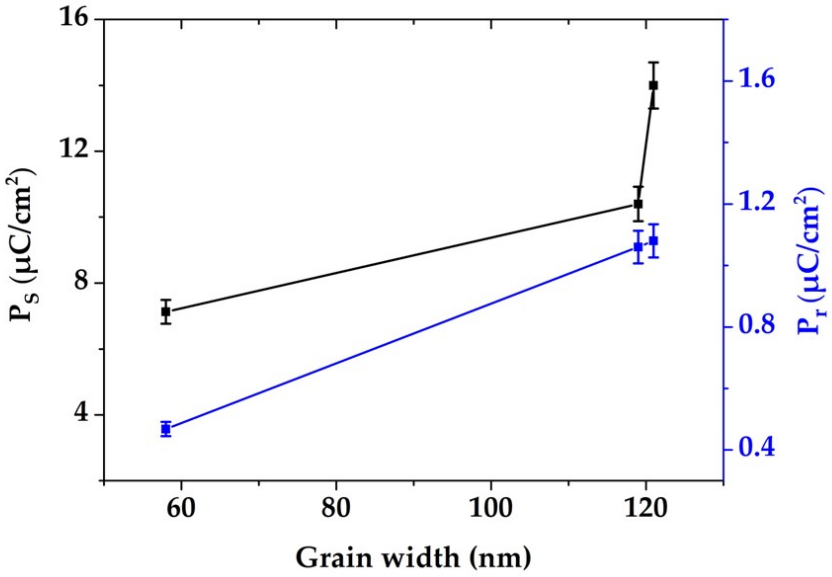

Figure 5.18: P_S (black line) and P_r (blue line) values at 1 kHz as a function of grain width.

Electrical property summary

- The permittivity of the grains and grain boundaries decrease as the dilution increases due to the lattice volume increase and *a* decrease.
- The conduction mechanism in the BST16 sample can be attributed to trap-filled limited charges at high voltages.
- The poling voltage decreases when the grain width increase which allows a faster poling process.
- All the samples show relaxor ferroelectric behavior. The P_S and P_r values increase with the grain width.

5.4 Conclusion

This chapter focused on the effect of solution dilution on the different properties of BST thin films. More homogeneous and dense films were obtained with increasing the dilution. This increase in dilution affected the morphology of the thin films by increasing the grain size and decreasing the surface and columnar roughness. An expansion in the

lattice volume was observed with dilution. The permittivity of grains and grain boundaries decreased with dilution due to the decrease in polarization caused by the out-of plane reduction in the lattice. A trap assisted conduction was detected in the BST16 sample at medium to high voltages. The increase in grain width allows lowering the poling voltage which is a very promising result that contributes in facilitating the poling process. Finally, the BST diluted samples exhibit ferroelectric relaxor behavior with increasing P_S and P_r values as the dilution increases.

References

[1] Mansour, C., Benwadih, M., Chahine, G. A., and Revenant, C. *AIP Advances* **10**(6), 065204 (2020).

[2] Schwartz, R. W., Schneller, T., and Waser, R. *Comptes Rendus Chimie* **7**(5), 433–461 (2004).

[3] Cheng, J.-G., Meng, X.-J., Li, B., Tang, J., Guo, S.-L., Chu, J.-H., Wang, M., Wang, H., and Wang, Z. *Applied Physics Letters* **75**(14), 2132–2134 (1999).

[4] Cheng, J.-G., Tang, J., Chu, J.-H., and Zhang, A.-J. *Applied Physics Letters* **77**(7), 1035 (2000).

[5] Zhang, Q. and Su, Y. *Journal of Applied Physics* **124**(14), 144103 (2018).

[6] Buscaglia, V. *Journal of the European Ceramic Society* , 15 (2020).

[7] Levasseur, D., El-Shaarawi, H., Pacchini, S., Rousseau, A., Payan, S., Guegan, G., and Maglione, M. *Journal of the European Ceramic Society* **33**(1), 139–146 (2013).

[8] Straumal, B., Kogtenkova, O., Gornakova, A., Sursaeva, V., and Baretzky, B. *Journal of materials science* **51**(1), 382–404 (2016).

[9] Eglitis, R. I. *Applied Surface Science* **358**, 556–562 (2015).

[10] Eglitis, R. I. and Vanderbilt, D. *Physical Review B* **76**(15), 155439 (2007).

[11] De Gennes, P. *The European Physical Journal E* **6**(1), 421–424 (2001).

[12] Saif, A. A. and Poopalan, P. *Journal of Materials Science & Technology* **27**(9), 802–808 (2011).

[13] Oh, J., Moon, T., Kim, T.-G., Kim, C., Lee, J. H., Lee, S. Y., and Park, B. *Current Applied Physics* **7**(2), 168–171 (2007).

[14] Hwang, C. S., Lee, B. T., Kang, C. S., Lee, K. H., Cho, H.-J., Hideki, H., Kim, W. D., Lee, S. I., and Lee, M. Y. *Journal of Applied Physics* **85**(1), 287–295 (1999).

[15] Silva, J., Sekhar, K., Rodrigues, S., Pereira, M., Parisini, A., Alves, E., Barradas, N., and Gomes, M. *Applied Surface Science* **278**, 136–141 (2013).

[16] Pečnik, T., Glinšek, S., Kmet, B., and Malič, B. *Journal of Alloys and Compounds* **646**, 766–772 (2015).

[17] Frey, M., Xu, Z., Han, P., and Payne, D. *Ferroelectrics* **206**(1), 337–353 (1998).

[18] Zhang, Q. and Su, Y. *Physics Letters A* **384**(12), 126374 (2020).

[19] Nagaraj, B., Aggarwal, S., and Ramesh, R. *J. Appl. Phys.* **90**(1), 9 (2001).

[20] Chiu, F.-C. *Advances in Materials Science and Engineering* **2014**, 1–18 (2014).

[21] Xiao, Y., Shenoy, V. B., and Bhattacharya, K. *Physical Review Letters* **95**(24), 247603 (2005).

[22] Hong, L., Soh, A. K., Du, Q. G., and Li, J. Y. *Physical Review B* **77**(9), 094104 (2008).

[23] Bednyakov, P. S., Sluka, T., Tagantsev, A. K., Damjanovic, D., and Setter, N. *Scientific reports* **5**, 15819 (2015).

[24] Chiu, F.-C., Chou, H.-W., and Lee, J. Y.-m. *Journal of Applied Physics* **97**(10), 103503 (2005).

[25] Isarakorn, D., Sambri, A., Janphuang, P., Briand, D., Gariglio, S., Triscone, J.-M., Guy, F., Reiner, J. W., Ahn, C. H., and de Rooij, N. F. *Journal of Micromechanics and Microengineering* **20**(5), 055008 (2010).

[26] Devasia, S., Eleftheriou, E., and Moheimani, S. O. R. *IEEE Transactions on Control Systems Technology* **15**(5), 802–823 (2007).

[27] Tahan, D., Safari, A., and Klein, L. C. In *Proceedings of 1994 IEEE International Symposium on Applications of Ferroelectrics*, 427–430, (1994).

[28] Wu, J., Gao, X., Yu, Y., Yang, J., and Dong, S. *Journal of Alloys and Compounds* **745**, 669–676 (2018).

[29] Huang, Y., Zhao, C., Wu, B., and Wu, J. *ACS Applied Materials & Interfaces* **12**(21), 23885–23895 (2020).

[30] Adikary, S. U. and Chan, H. L. W. *Thin Solid Films* , 5 (2003).

[31] Orlik, K. *Nouvelles céramiques piézoélectriques sans plomb pour des applications sonar ou de contrôle non destructif*. PhD thesis, Polytechnique Hauts-de-France, (2019).

[32] Samara, G. A. In *Solid State Physics*, volume 56, 239–458. Elsevier (2001).

Résumé

Chapitre 1 : Ferroélectricité et structure

Historique

L'une des plus grandes percées dans ce domaine a été la découverte de la ferroélectricité dans $BaTiO_3$ (1945) qui est devenu le matériau ferroélectrique le plus étudié avec une structure pérovskite ABO_3. Il était logique de poursuivre la recherche sur les matériaux pérovskites avec les blocs octaédriques à oxygène BO_6 qui sont à l'origine de la ferroélectricité. Cette recherche a donnée lieu à la découverte de nouveaux matériaux ferroélectriques tels que $KNbO_3$ et $KTaO_3$ (1949), $LiNbO_3$ et $LiTaO_3$ (1949), $PbTiO_3$ (1950).

Classification des matériaux

La figure (5.19) montre une représentation générale de la classification des matériaux diélectriques. Les ferroélectriques forment un sous-groupe de pyroélectriques qui sont un sous-groupe de piézoélectriques. La principale caractéristique d'un matériau ferroélectrique est d'avoir une polarisation spontanée qui peut être inversée par un champ électrique appliqué.

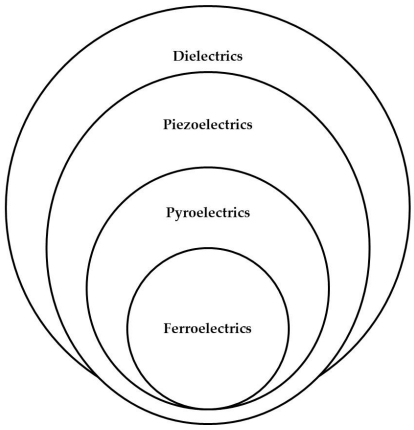

Figure 5.19: Diagramme des classes de matériaux diélectriques.

Phénomène de ferroélectricité

Les ferroélectriques sont des diélectriques qui sont des matériaux polaires qui possèdent un vecteur de polarisation spontanée, existant intrinsèquement dans le matériau sans l'application d'un champ électrique externe. La caractéristique distincte d'un matériau ferroélectrique est la capacité pour la polarisation de basculer entre au moins deux orientations d'équilibre en présence d'un champ électrique appliqué. Ces matériaux passent par une transition de phase non polaire paraélectrique à haute température à une phase polaire ferroélectrique à plus basse température. Les transitions de phase sont basées sur le changement de la symétrie à l'intérieur du matériau, par exemple, la transition la plus courante est de la symétrie cubique à tétragonale. La température de transition est appelée température de Curie T_C. La figure (5.20) montre comment la permittivité diélectrique ϵ diminue fortement au-dessus de T_C. La permitivté diélectrique suit la loi Curie-Weiss:

$$\varepsilon = \varepsilon_0 + \frac{C}{T - T_C}. \tag{5.12}$$

où C est la constante de Curie et ϵ_0 est la permittivité diélectrique du vide.

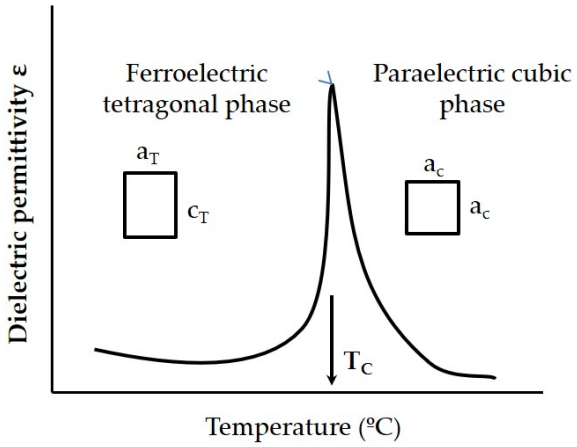

Figure 5.20: Transition de phase ferroélectrique-paraélectrique de la symétrie tétragonale à cubique.

Matériaux ferroélectriques

La ferroélectricité peut être vue dans les matériaux sous plusieurs formes tels que les monocristaux, les polymères, les céramiques et les films minces. Dans cette thèse, nous nous intéressons aux couches minces ferroélectriques. Les films minces sont technologiquement souhaitables afin d'éviter le traitement de matériaux massifs. Le traitement des matériaux massifs est difficile et coûteux, et il est plus pratique de déposer directement le matériau sous forme de film mince sur un substrat. Il existe de nombreuses techniques de dépôt utilisées pour la fabrication de couches minces ferroélectriques telles que le dépôt de solution chimique (CSD), en particulier les voies sol-gel ou le dépôt organique de métaux (MOD), pulvérisation, dépôt par faisceau ionique et dépôt laser pulsé (PLD). Le défi principal est d'obtenir des propriétés similaires à celles des céramiques massifs et même d'améliorer les facteurs de mérite.

Matériaux sans plomb

De nos jours, les matériaux ferroélectriques sans plomb commencent à remplacer les composés toxiques à base de plomb. Dans cette thèse, deux matériaux prometteurs sont étudiés pour leurs propriétés ferroélectriques et pyroélectriques exceptionnelles sous forme de couches minces.

Titanate de baryum strontium (BST)

BST a une structure de type pérovskite présentée dans la figure 5.21 (a). La T_C peut être adaptée en faisant varier la concentration de Sr. La température de transition ferroélectrique à paraélectrique, marquée par le pic de permittivité diélectrique, varie en changeant le rapport Ba/Sr de 0 à 1. La microstructure des films minces BST peut être adaptée en ajustant les paramètres tels que la chimie de la solution de précurseur, les traitements thermiques et la concentration de la solution. De plus, la microstructure a une influence majeure sur les propriétés des couches minces.

Niobate de strontium baryum (SBN)

$Sr_xBa_{1-x}Nb_2O_6$ (SBN) cristallise dans la région 0,25 < x < 0,75 avec la structure bronze tungstène tétragonal (TTB) présenté sur la figure 5.21 (b).

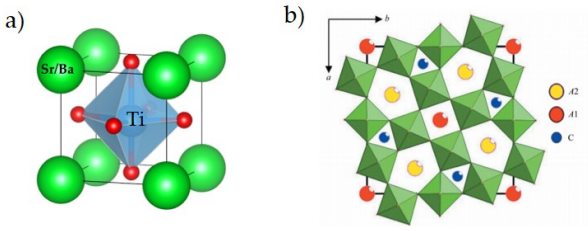

Figure 5.21: Schématique de la cellule unitaire de (a) BST et (b) SBN.

Dans les films minces de SBN, l'effet des interfaces sur la permittivité diélectrique mesurée est augmenté. C'est probablement l'une des raisons de la dispersion des résultats rapportés. La deuxième raison réside dans la méthode utilisée pour enregistrer un cycle d'hystérésis. En effet, le courant de perte diélectrique est également intégré et peut contribuer à former le cycle d'hystérésis observé.

Conclusion

Dans ce chapitre, la phénoménologie de la ferroélectricité a été présentée. Une approche théorique et thermodynamique sur le phénomène ferroélectrique a été introduite ainsi que des caractéristiques ferroélectriques importantes. En outre, la variété des matériaux ferroélectriques a été présentée dans ce chapitre, en mettant l'accent sur des matériaux inorganiques sans plomb tels que les films minces de BST et SBN.

Chapitre 2 : Méthodes d'élaboration et de caractérisation des condensateurs à couche mince

Introduction

Ce chapitre vise à discuter les différents aspects de l'élaboration et de la caractérisation des condensateurs à couche mince. La méthode sol gel, le traitement des couches minces pérovskites et les travaux expérimentaux effectués sur la formation de couches minces inorganiques sont abordés. Les différentes techniques de caractérisation utilisées pour étudier la morphologie, la structure et les propriétés électriques des couches minces sont présentées.

Méthode sol gel

Le processus de sol gel est une approche bien établie pour préparer des films minces d'oxyde, avec un contrôle potentiel sur les propriétés de texture et de surface des matériaux. D'un point de vue technologique, le sol-gel nécessite moins d'équipement et est potentiellement moins coûteux. Avec cette méthode, on peut contrôler précisément la microstructure des films déposés tels que la taille des pores, le volume des pores et la surface. Il permet également le dépôt de solution à plus grande échelle et même sur des substrats flexibles.

Dépôt de solutions sol-gel

Le spin coating et le dip coating peuvent être utilisés pour le dépôt de solutions. Le processus de spin coating est utilisé dans ce travail, et est divisé en quatre étapes: **dépôt, spin up, spin off et évaporation** (Fig. 5.22). La quatrième étape peut se produire pendant les trois autres étapes à moins qu'il n'y ait des précautions pour retarder l'évaporation.

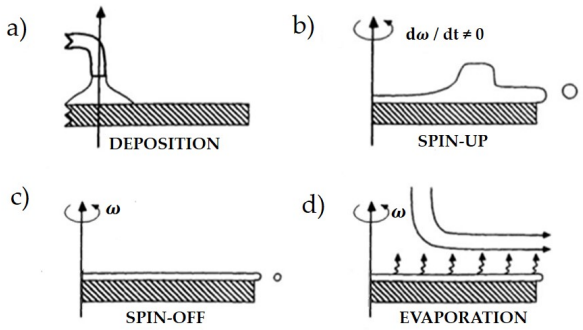

Figure 5.22: Étapes du spin coating.

Traitement des couches minces pérovskites

La microstructure des couches minces de pérovskite dépend généralement de la nature du substrat, de la chimie de la solution et du traitement thermique. Le comportement de décomposition du précurseur change suivant la méthode adoptée (MOD, sol gel ou chélate). En outre, l'atmosphère ambiante utilisée lors de la pyrolyse et de la cristallisation peut affecter non seulement la teneur en carbone résiduel dans les films mais également la nature des phases intermédiaires. La vitesse de chauffage et la température de pyrolyse ont également un impact.

Équipements et matériaux

La préparation de la solution et le dépôt de la couche mince sont effectués dans un environnement de salle blanche pour éviter toute contamination par des particules de poussière dans l'air. Le substrat choisi pour le dépôt des couches minces était $Pt/TiO_2/SiO_2/Si$. Les épaisseurs de film mince d'électrode étaient Pt (100 nm), TiO_2 (10 nm), oxyde de silicium SiO_2 (500 nm) et plaquette de silicium (725 μm). Après le dépôt de solution par spin coating, les films subissent un traitement thermique en deux temps pour la pyrolyse et la cristallisation des couches minces.

Techniques de caractérisation des couches minces

Les techniques morphologiques et structurelles utilisées sont: la microscopie électronique à balayage (MEB), la microscopie à force atomique (AFM) et la diffusion des rayons X aux petits angles en incidence rasante (GISAXS) ont été choisies pour sonder la morphologie des couches minces à l'échelle nanométrique. La diffraction des rayons X (DRX) a été utilisée pour étudier la structure des films. La spectroscopie photoélectronique aux rayons X (XPS) est utilisée pour déterminer la composition des couches minces. Les techniques de caractérisation électriques comprennent des mesures diélectriques, de densité de courant et des mesures de cycle ferroélectrique.

Conclusion

Ce chapitre a présenté les méthodes utilisées dans l'élaboration de couches minces. Le traitement des films minces dérivés du sol gel a été discuté, mettant en lumière l'importance de la chimie de synthèse des précurseurs et des processus de recuit thermique. Les techniques d'étude de la morphologie et de la structure ont été présentées ainsi que les méthodes de mesures diélectriques et ferroélectriques des couches minces.

Chapitre 3 : Chimie sol-gel à base de carboxylate: des solutions à la formation de couches minces

Introduction

Des précurseurs de carboxylates métalliques sont utilisés pour l'élaboration de couches minces de deux matériaux ferroélectriques prometteurs: le niobate de strontium baryum (SBN) et le titanate de baryum strontium (BST). Le SBN est synthétisé dans notre laboratoire en utilisant l'approche carboxylate et le BST est une solution commerciale. Ce chapitre se concentre sur la synthèse de solutions de précurseurs SBN et la formation de couches minces. Les précurseurs moléculaires attendus des métaux doivent être parfaitement miscibles entre eux. Le poids moléculaire du ligand doit être raisonnable permettant la formation de solutions à forte concentration en métal. De plus, l'aspect difficile est d'éviter la formation de carbonate pendant la croissance de la couche d'oxyde sans faire de recuit sous oxygène.

Préparation des solutions SBN

De multiples défis ont été rencontrés dans la préparation de solutions de carboxylates métalliques de chaque métal:

- Stabiliser les solutions.
- Miscibilité du mélange de solutions précurseurs.
- Atteindre des concentrations élevées de précurseurs métalliques.
- Obtention de la stoechiométrie correcte pour le mélange de précurseurs.

Plusieurs acides carboxyliques avec différents groupes alkyles et différents solvants ont été testés afin de surmonter les difficultés de la fabrication de solutions. Les alcoxydes de Ba et Sr ont été traités avec des acides carboxyliques pour obtenir les solutions de carboxylate souhaitées dans la stoechiométrie appropriée. Le chlorure de niobium a été utilisé comme réactif de départ pour fabriquer du carboxylate de Nb. Il a été mélangé avec une solution de carboxylate de sodium pour former le carboxylate de niobium. Le produit secondaire de cette réaction était le chlorure de sodium (NaCl) qui n'était pas

soluble dans le solvant alcoolique et a été filtré plus tard. Le tableau (5.6) représente les compositions de mélange choisies.

Solutions	Ba carboxylate	Sr carboxylate	Nb carboxylate	Metallic wt.%
T1	Ba 2-ethylhexanoate	Sr 2-ethylhexanoate	Nb 2-ethylhexanoate	7
T2	Ba 2-ethylhexanoate	Sr 2-2	Nb glycolate	13
T3	Ba isovalerate	Sr 2-2	Nb glycolate	15

Table 5.6: Tableau montrant les différentes solutions de précurseurs mixtes et leurs pourcentages en poids.

Couches minces SBN

Après la préparation des trois solutions de SBN, celles-ci ont été laissées en salle blanche pendant quelques jours pour se stabiliser. Ensuite, les solutions sont déposées sur un substrat de silicium par spin coating. Le film déposé a été pyrolysé à 200 °C pendant 10 min puis 450 °C pendant 10 min sur une plaque chauffante à l'air avant le recuit final. Ce pré-recuit a été utilisé pour décomposer les espèces organiques dans la structure du film. Les films ont ensuite été recuits à 600 °C dans l'air pendant une heure pour obtenir la cristallisation des films minces SBN.

Étude morphologique

- Les figures MEB Fig.(5.23) montrent une morphologie différente pour T1, T2 et T3.
- L'échantillon T1 avec le poids en métal le plus faible et le groupe alkyle le plus long a plus de défauts de surface tels qu'une rugosité de surface significative, des pores et des films non uniformes.
- T2 et T3 ont une morphologie de surface plus lisse et moins de défauts de surface.

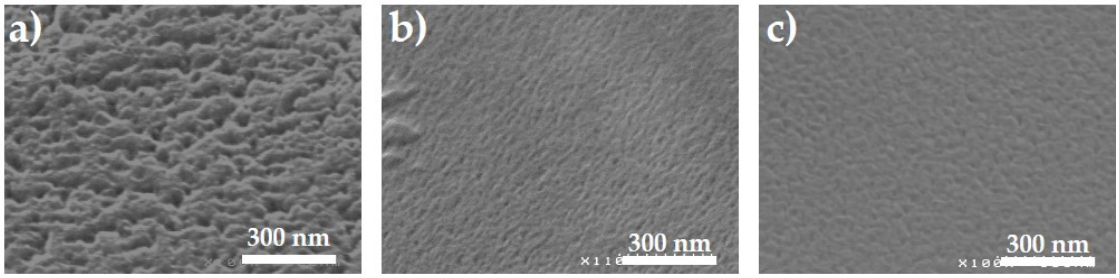

Figure 5.23: Images MEB montrant la vue en plan d'une couche déposée de films minces SBN sur ITO/Si/SiO_2 après traitement thermique à 600 °C: (a) échantillons T1, (b) T2 et (c) T3.

Analyse de composition par XPS

Les résultats des mesures XPS montrent:

- La présence de carbonates à la surface des couches minces SBN, significativement dans l'échantillon T1.
- Une différence de stoechiométrie entre T1, T2 et T3.
- La présence d'impuretés sous forme de Na.

Conclusion

Les solutions de précurseurs de SBN ont été synthétisées avec succès en utilisant la voie carboxylate. L'utilisation d'acides carboxyliques avec une ramification variante a abouti à une chimie de solution et une morphologie de film différentes. La présence de carbonate est un problème très courant dans ce type de chimie et est préjudiciable à la fonctionnalité des couches minces. En utilisant cette voie, il existe un moyen d'éliminer les carbonates même sans recuit sous atmosphère d'oxygène. La chimie des solutions elle-même n'a pas été complètement caractérisée car ce n'était pas le but principal de cette thèse.
La solution commerciale BST sera utilisée pour mener les études technologiques et fondamentales décrites dans les deux chapitres suivants.

Chapitre 4 : Effet du recuit thermique sur la morphologie des couches minces de BST : conséquences sur les propriétés électriques

Introduction

Le lien entre la morphologie et les propriétés électriques des couches minces sol-gel de $Ba_{0.7}Sr_{0.3}TiO_3$ est étudié. Des mesures de GISAXS *in situ* ont permis de sonder la morphologie dès le début de la séparation de phase organique-inorganique dans le film en fonction du recuit thermique. Les mesures *ex situ* permettent de suivre la formation des particules et des pores en fonction de la température de recuit, la durée du recuit et la nature du substrat. Un modèle général de formation de film sol-gel basé sur la physique des fluides à l'échelle nanométrique a été développé. Enfin, des conditions optimisées de dépôt et de recuit nous permettent d'obtenir des résultats préliminaires de condensateurs ferroélectriques.

Étude fondamentale

in situ GISAXS

Pour les mesures *in situ*, la solution a été déposée sur le substrat SiO_2/Si, puis recuite à 130 °C pendant 5 min avant la mesure. Cette expérience apporte des connaissances générales sur le tout début de la formation de couches minces sol-gel à partir de l'état liquide. Une modulation de densité électronique indique la formation de domaines dans le film liquide à basse température de recuit (Fig. 5.24 (B)). Une séparation de phase se produit entre les domaines riches/pauvres en matières inorganiques. Ces domaines commencent à croître à partir de 200 °C (Fig.5.24 (C)).

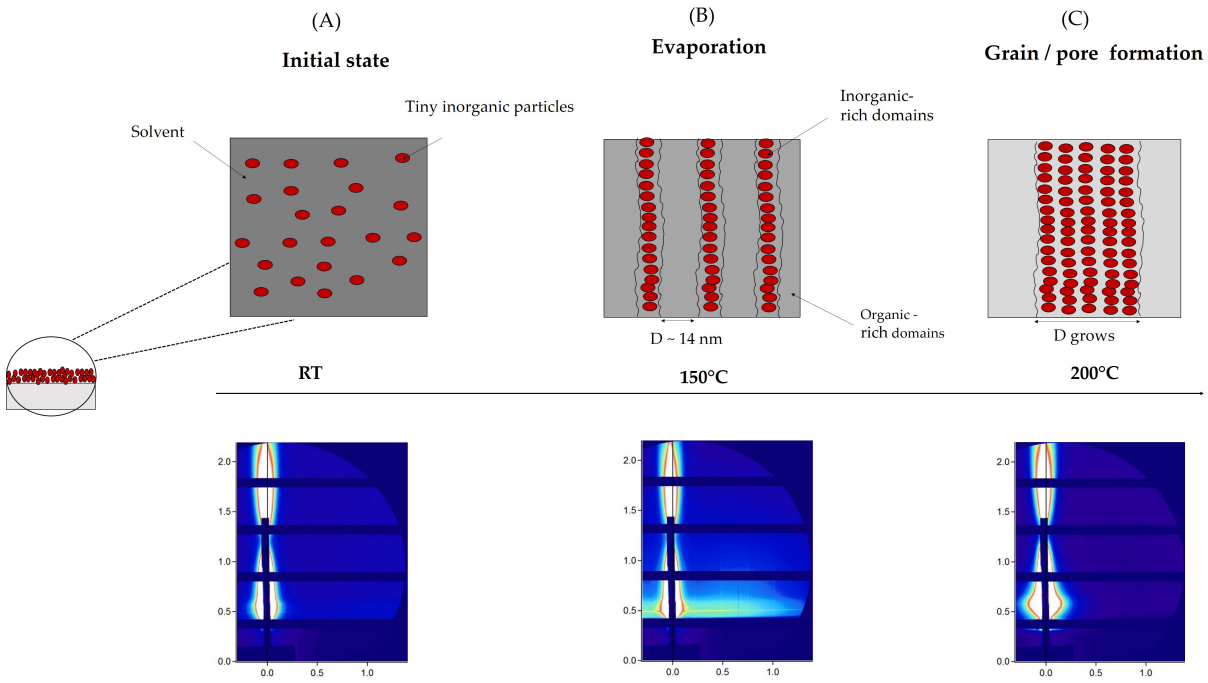

Figure 5.24: Schéma en coupe représentant l'évolution *in situ* du film déposé en fonction de la température jusqu'à 200 °C.

ex situ GISAXS

Les mesures *ex situ* ont été effectuées sur une couche de BST déposée sur SiO_2/Si puis recuite à 600 °C et aussi sur plusieurs couches déposées (cinq couches) sur SiO_2/Si et Pt/Cr/SiO_2/Si recuites à différentes températures. Une étude cinétique avec plusieurs temps de recuit (5 min, 15 min, 30 min et 60 min) sur une couche de BST recuit à 600°C a été effectuée. Cette étude met en évidence le long temps de recuit nécessaire pour éliminer les constituants organiques dans une couche déposée épaisse. Ainsi, lors d'un recuit à des températures plus élevées, les domaines riches en matières organiques deviennent des pores en raison de l'évaporation des constituants organiques et les domaines riches en inorganiques deviennent des particules.

Effet de substrat et formation de pores:
Les pores adoptent une forme sphéroïde aplatie pour les deux films sur SiO_2 et Pt. Pour SiO_2, les pores ont des tailles similaires de 600 °C à 800 °C. En revanche, pour les films BST déposés sur Pt, la taille des pores diminue avec l'augmentation des températures de recuit. Les pores adoptent une forme de sphéroïde aplatie en raison de la contrainte de traction dans les films BST. Quantitativement, la porosité ϕ dans les films BST sur Pt a

diminué de 0,13 à 0,06 avec l'augmentation de la température de recuit de 600 °C à 800 °C.

Structure et morphologie

La structure des couches minces est étudiée par DRX et la morphologie par MEB. Les couches minces de BST recuites à haute température cristallisent dans une phase de pérovskite polycristalline avec une hauteur de grains de $\sim$ 17 nm en moyenne. Aucune croissance colonnaire n'a été observée dans les films BST selon les observations MEB et le GISAXS *ex situ*. Le modèle de convection et d'évaporation explique la formation d'un film à des températures de recuit basses et élevées. Le modèle utilise une hypothèse de la première loi de Fick postulant que le flux de diffusion va des régions de plus grande fraction de solvant vers les plus faibles. Le temps d'évaporation est inversement proportionnel à la température de recuit et proportionnel au carré de l'épaisseur du film, expliquant le nécessité de longs temps pour éliminer les composants organiques des films.

Étude de condensateur à couche mince BST

Pour cette étude, les échantillons ont été déposés par centrifugation sur $Pt/TiO_2/SiO_2/Si$ à 4000 tours/min pendant 30 s et recuits à 450 °C pendant 5 min sur une plaque chauffante après chaque dépôt de couche. Les échantillons ont ensuite été recuits à 700 °C pendant 1 min dans un four sous atmosphère d'air ambiant après une couche déposée (1 L) ou après deux couches déposées (2 L).
Le type de croissance n'est pas fondamentalement lié à un critère d'épaisseur, mais à la quantité de constituants organiques restants. Quels que soient les types de recuit à haute température, le dépôt de couches supplémentaires se produit avec une nucléation hétérogène. Les constituants organiques restants sont responsables du mauvais comportement électrique et non ferroélectrique observé dans l'échantillon de 2 L. L'échantillon 1 L a de bonnes propriétés diélectriques et ferroélectriques.

Conclusion

Des films prototypes ont été étudiés en fonction de la température de recuit à basse température (140 °C -200 °C) par in situ GISAXS et à des températures élevées (600 °C -800 °C) par ex situ GISAXS. À $\sim$ 150 °C, des domaines auto-organisés avec une distance préférentielle d'environ 14 nm sont formés. Aux températures de recuit élevées, les domaines de croissance deviennent soit des nanoparticules, soit des pores avec une distance préférentielle de 85 nm à 600 °C. Cette évolution de croissance est expliquée avec succès par un modèle général basé sur la convection et l'évaporation. De plus, deux types de recuit ont été étudiés à 700 °C. Un recuit après deux couches déposées (2 L) produit de particules décalées verticalement et aucun comportement ferroélectrique n'est observé. Au contraire, un recuit après une couche déposée (1 L) donne une croissance en colonne et un cycle d'hystérésis ferroélectrique a été obtenue.

Chapitre 5 : Étude de l'effet de dilution sur les propriétés morphologiques, structurelles et électriques des couches minces BST

Introduction

Dans ce chapitre, nous nous sommes intéressés à l'étude de l'effet de dilution de la solution de précurseur sur les différentes propriétés des couches minces de BST. Tout d'abord, la morphologie colonnaire, la granulométrie et la rugosité des films dilués ont été étudiées à l'aide du MEB et de l'AFM. L'évolution de la structure des couches minces BST a été étudiée à l'aide de la XRD. Une explication de la taille des grains et de la variation de rugosité a été proposée sur la base du modèle de convection et de diffusion. Enfin, les propriétés électriques des films minces de BST dilués ont été discutées.

Morphologie et structure des couches minces diluées

Notons BST32, BST16 et BST8 les trois échantillons de couches minces avec des concentrations de précurseurs de 0,032 M, 0,016 M et 0,008 M respectivement.
Avec la dilution de la solution de précurseur BST:

- On obtient des films plus homogènes et plus denses.
- La taille des grains (largeur et hauteur) augmente en raison de la coalescence. La largeur du grain est plus grande avec une augmentation d'un facteur 2 de BST32 à BST8.
- La rugosité de la surface libre et des colonnes intérieures diminue. Les valeurs Rms diminuent d'un facteur 2,6 de BST32 à BST8.
- Les paramètres du réseau *a* et *c* deviennent respectivement plus petits et plus grands.
- Le volume du réseau augmente.

Propriétés électriques

- La permittivité des grains et des joints de grains diminue à mesure que la dilution augmente.
- Le mécanisme de conduction dans l'échantillon BST16 peut être attribué au Space Charge Limited Conduction (SCLC).
- La tension de polarisation diminue lorsque la largeur du grain augmente, ce qui permet un processus de polarisation plus rapide.
- Tous les échantillons présentent un comportement ferroélectrique (Fig.5.25). Les valeurs de P_S et P_r augmentent avec la largeur du grain.

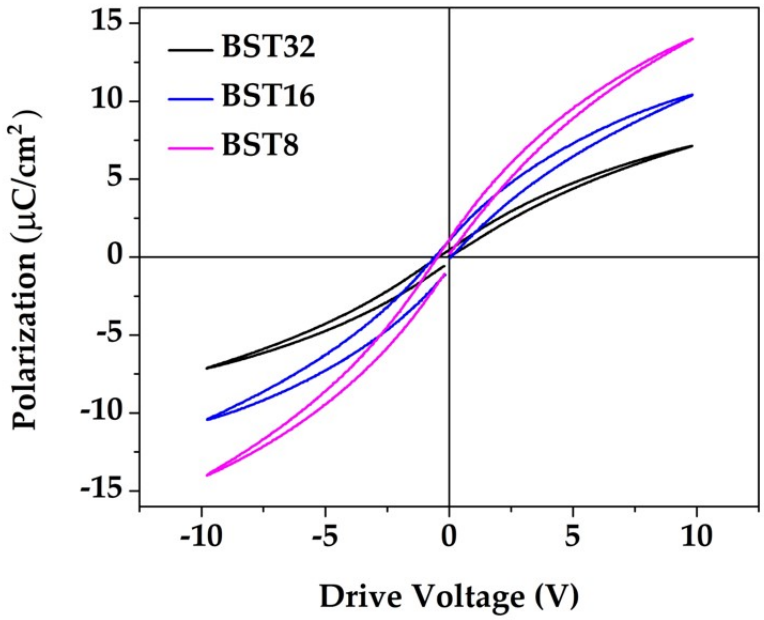

Figure 5.25: Polarisation vs tension pour les films BST à RT à 1 kHz.

Conclusion

Ce chapitre s'est concentré sur l'effet de la dilution de la solution sur les différentes propriétés des couches minces BST. Des films plus homogènes et plus denses ont été

obtenus avec l'augmentation de la dilution. Cette augmentation de la dilution affecte la morphologie des films minces en augmentant la taille des grains et en diminuant la rugosité de surface des colonnes. Une expansion du volume du réseau est observée avec une augmentation de la hauteur des grains. La permittivité des grains et des joints de grains diminue avec la dilution. Une conduction SCLC a été mise en évidence dans l'échantillon BST16 à des tensions moyennes à élevées. L'augmentation de la largeur des grains permet d'abaisser la tension de polarisation, ce qui est un résultat très prometteur pour faciliter le processus de polarisation. Enfin, les échantillons BST dilués présentent un comportement de relaxeur ferroélectrique avec des valeurs de P_S et P_r croissantes à mesure que la dilution augmente.

Conclusion générale et perspectives

Dans la plateforme PICTIC, le travail est essentiellement effectué avec des matériaux à base d'encre ou de solutions pour fournir des capteurs d'empreintes ou de la récupération d'énergie. On cherche des matériaux ferroélectriques performants, et pour le moment le PVDF est le plus adapté. Afin de développer une nouvelle génération plus performante de couches minces ferroélectriques, on s'intéresse à des élaborations par voie chimique d'autres matériaux. Dans cette thèse, des procédés d'élaboration à base de solution sont utilisées pour synthétiser les films minces souhaités. Les précurseurs à base de carboxylates sont choisis pour élaborer les solutions pour les films minces SBN et BST. Cette voie est bien adaptée pour la manipulation de précurseurs métalliques sensibles à l'humidité, il n'y a pas besoin de travailler sous une atmosphère riche en argon ou azote, ce qui simplifie fortement le procédé. Les solutions de SBN sont préparées dans notre laboratoire en utilisant des acides carboxyliques avec différentes ramifications. Des effets d'encombrement stérique sur les solutions et les films minces sont mis en évidence. On as obtenu des couches épaisses d'oxydes mixtes exemptes de carbonates mais qui nécessitaient un important travail sur le recuit pour atteindre les phases d'intérêt. C'est pourquoi des solutions commerciales à base de carboxylate de BST sont ensuite utilisées pour réaliser des couches montrant un effet ferroélectrique indéniable. Dans le chapitre 4, l'influence des conditions de dépôt et du traitement thermique sur la formation de couches minces est étudiée. Les études fondamentales dont les mesures GISAXS *in situ* et *ex situ* sont effectuées sur les films BST recuits à basse et haute température. Des études *in situ* à $\sim$ 150 °C ont montré la formation de domaines auto-organisés avec une distance préférentielle d'environ 14 nm. À des températures plus élevées (environ 600 °C), les domaines s'agrandissent pour devenir soit des nanoparticules, soit des pores avec une distance préférentielle de 85 nm. L'évolution de la croissance est expliquée par un modèle général basé sur les phénomènes de convection et d'évaporation. Ce modèle a permis d'expliquer qu'avec l'augmentation des températures de recuit, les longueurs caractéristiques parallèles à la surface augmentent à cause de la convection. Celles qui sont

perpendiculaires diminuent à cause de l'évaporation. Pour la première fois, la raison fondamentale de la croissance colonnaire a été mise en évidence. Il s'agit de l'élimination des espèces organiques dans les couches inférieures. Sinon, la croissance est granulaire. Afin d'obtenir un condensateur BST fonctionnel, le recuit de type 1 L a été adopté. Il a abouti à des films colonnaires et un cycle d'hystérésis ferroélectrique a été obtenu.
Dans le chapitre 5, les effets de la dilution de la solution sur les propriétés des films minces BST de type 1 L ont été étudiés. L'augmentation du taux de dilution engendre une diminution de la rugosité surfacique et colonnaire. Cette diminution de la rugosité permet la coalescence des grains, donnant des grains finalement plus gros. Les paramètres de réseau *a* et *c* varient avec l'augmentation de la dilution provoquant une expansion du volume du réseau. Un effet clair a été observé sur la permittivité des grains et des joints de grains qui diminue avec la dilution. On a réussi à baisser la tension de polarisation dû à l'augmentation de la largeur des grains. Ceci est un résultat très prometteur qui a facilité le processus de 'poling'. Les échantillons dilués de BST présentent un comportement ferroélectrique relaxeur avec des valeurs de P_S et P_r qui augmentent avec la dilution. En résumé, la ferroélectricité des couches minces BST est définitivement liée à l'élimination complète des constituants organiques. Dans cette thèse, nous avons pu adapter la nanostructure des couches minces à l'échelle nanométrique en comprenant les mécanismes physiques sous-jacents qui régissent la formation de couches minces par voie chimique. On a constaté que les films minces BST colonnaires étaient les relaxeurs ferroélectriques les plus appropriés. Des propriétés ferroélectriques améliorées ont été obtenues avec la dilution des solutions de précurseurs. Une diminution de la tension de polarisation avec l'augmentation de la largeur des grains a été observée, ce qui est extrêmement intéressant pour les applications qui nécessitent des basses tensions.

BST vs PVDF et composites

Des travaux de recherhce sur le PVDF et les composites inorganiques/polymères ont lieu dans notre laboratoire. Les couches minces BST étudiées dans cette thèse se révèlent avoir des propriétés relaxantes ou ferroélécriques prometteuses qui peuvent être intéressantes pour les applications de récupération d'énergie. La figure (5.26) montre les différentes boucles d'hystérésis ferroélectriques pour les films minces BST, PVDF, BTO / PVDF et PZT / PVDF films minces composites. Le tableau (5.7) indique les valeurs P_S et P_r pour ces matériaux ferroélectriques.

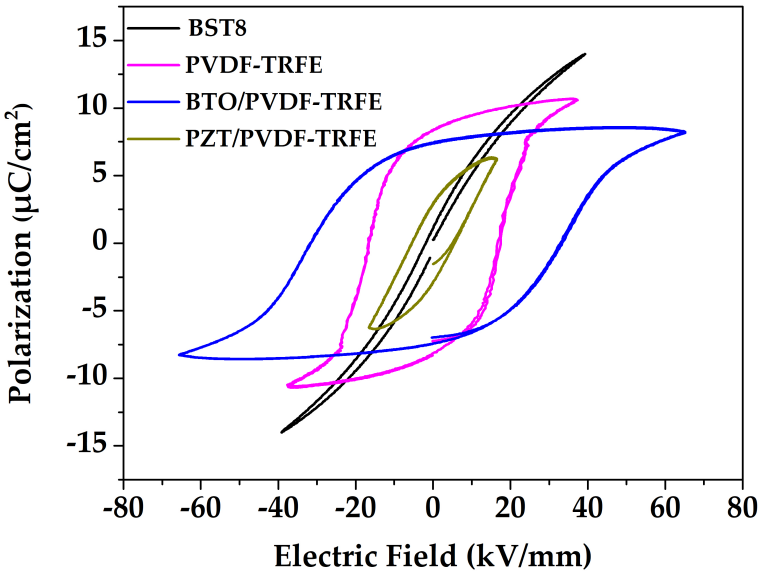

Figure 5.26: Différents cycles d'hystérésis P-E pour les matériaux BST et PVDF.

Echantillons	Epaisseur (μm)	P_S (μC/cm^2)	P_r (μC/cm^2)
BST8	0.25	13.97	1.16
PVDF	4	10.53	8.46
BTO/PVDF	10	8.28	7.44
PZT/PVDF	20	6.15	2.97

Table 5.7: Tableau représentant les valeurs de P_S et de P_r pour BST, PDVF et composites.

Indépendamment de la différence d'épaisseur entre les différents matériaux, les couches minces BST présentent les valeurs les plus élevées de P_S et nécessitent des tensions de polarisation inférieures par rapport au PVDF (> 150 V/μm).

Perspectives

Cette section présente le travail futur qui pourrait être effectué sur les deux matériaux SBN et BST. Dans le travail de recherche actuel, des solutions de précurseurs SBN à base de carboxylate ont été élaborées. On a pu réaliser des couches épaisses riches en métal en utilisant des solutions de carboxylates de métaux dont on peut ajuster la stoéchiométrie à volonté. De plus, le choix des précurseurs carboxylates a permis d'éviter la formation de carbonates d'alcalino-terreux. Des travaux supplémentaires seraient nécessaires pour une meilleure compréhension de la chimie en question. En particulier, il serait intéressant d'étudier les entités carbonatées dans le système en utilisant des méthodes de caractérisation adaptées telles que la Résonance Magnétique Nucléaire (RMN) ^{13}C. La diffraction des rayons X montre qu'il y a déjà du Nb_xO_y cristallisé autour du SrBaO. D'autres pistes d'élaboration par voie chimique pourraient être envisagées comme l'utilisation de solvants à base d'oxime au lieu d'acides carboxyliques afin de limiter la teneur en carbone, permettant ainsi une cristallisation à plus basse température. Une autre possibilité serait d'utiliser des germes de nanoparticules d'oxyde de niobium, de baryum ou de strontium pour favoriser la cristallisation et la formation de phase à plus basse température. Dans le cas de l'étude sur les couches minces BST, une poursuite des travaux sur l'origine du mécanisme de conduction pourrait être envisagée. Par exemple, les lacunes d'oxygène sont l'une des causes de la présence de fuite du courant électrique dans les films minces tels que BST. Pour cela, des mesures *I-V* en fonction de la température et du temps pourraient être effectuées et pourraient apporter des informations très utiles sur l'origine et la nature de la conduction dans les couches minces BST. De plus, des mesures ferroélectriques avancées pourraient être bénéfiques pour évaluer la capacité des couches BST dans le stockage d'énergie. Ces dernières années, les efforts de développement des sources d'énergie renouvelables ont été inspirés par l'évolution de l'économie, le changement climatique et la pollution atmosphérique. Cela a entraîné une demande plus élevée de systèmes de stockage d'énergie tels que les condensateurs diélectriques. De nouveaux matériaux sans plomb ont été récemment étudiés pour leurs bonnes propriétés de stockage d'énergie [1]. Je présente ci-dessous une étude préliminaire sur les propriétés de stockage d'énergie des échantillons dilués de couches minces BST discutées dans le chapitre 5.

Le cycle *P-E* peut être utilisé pour calculer les capacités de stockage d'énergie. La densité d'énergie récupérable *W* correspond à la zone au-dessus du cycle d'hystérésis c'est-à-dire l'intégrale de la zone comprise entre la courbe de décharge et l'axe y, notée (I) dans l'encart de la figure (5.27). La densité de perte d'énergie W_{loss} correspond à la zone à l'intérieur

de la boucle d'hystérésis i.e. l'intégrale de l'aire comprise entre les courbes de charge et de décharge, notée (II) en l'encart de la figure (5.27). L'efficacité de stockage d'énergie est $R = W / (W + W_{loss})$ [2].

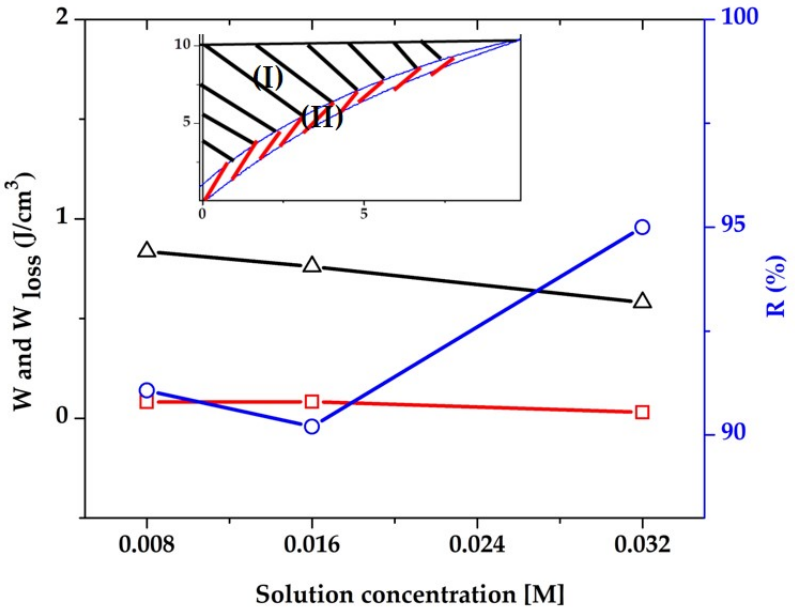

Figure 5.27: La densité d'énergie récupérable W (ligne noire), la perte d'énergie W_{perte} (ligne bleue) et l'efficacité de stockage d'énergie R (ligne rouge) tracées en fonction de la concentration de la solution de précurseurs. L'encart montre les zones ombrées du cycle d'hystérésis utilisées dans le calcul des densités d'énergie.

Les données calculées pour le stockage d'énergie sont représentées sur la figure (5.27). BST8 possède la plus grande densité de stockage d'énergie (W = 0,84 J /cm^3) et une bonne efficacité (R = 95,4%).
L'électronique flexible est en plein développement et suscite un fort intérêt pour de nombreuse applications notamment la récupération d'énergie et de capteurs d'empreintes. Pour cela, il faut baisser la température de recuit pour pouvoir déposer sur des substrats flexibles conformes. Bretos et al. montrent que la chimie de la solution peut être adaptée pour concevoir les précurseurs moléculaires souhaités par des méthodes chimiques par voie humide. Ils montrent également que la lumière peut être utilisée comme source d'énergie alternative pour induire la cristallisation de couches minces d'oxyde métallique par photochimie. L'abaissement de la température de cristallisation permet l'intégration des oxydes métalliques dans les dispositifs électroniques en particulier les systèmes flexibles [3].
De plus, les mesures pyroélectriques pourraient être prises en compte dans les futurs

travaux sur les condensateurs de couches minces. Le courant pyroélectrique peut être détecté par la mesure de la variation du courant avec la température.

General conclusion and prospects

In the PICTIC platform, the work is essentially carried out with materials based on inks or solutions to provide fingerprint sensors or energy recovery. We are looking for efficient ferroelectric materials, and for the moment PVDF is the best one. For that matter, we are interested in elaborating a new generation of thin films using chemical routes such as MOD and sol gel in order to synthesize high-performance ferroelectric capacitors. In this thesis, solution derived methods are employed to synthesize the desired thin films. Carboxylate based precursors are chosen to elaborate the solutions for SBN and BST thin films. This route is well adapted for handling moisture sensitive metal precursors, thus, there is no need to work under argon or nitrogen atmosphere, which simplifies the processing of the solutions. SBN solutions are prepared in our laboratory using carboxylic acids with different ramifications. Steric hindrance effects on the solutions and thin films are established. Thick layers of mixed oxides free of carbonates were obtained but required significant annealing work to reach the phases of interest. This is why commercial solutions based on BST carboxylate are then used to produce layers showing a ferroelectric effect. In chapter 4, the influence of the processing conditions on thin film formation is investigated. Fundamental studies included *in situ* and *ex situ* GISAXS measurements were performed on low and high temperature annealed BST thin films. *In situ* studies at $\sim$ 150 °C showed the formation of self-organized domains with a preferential distance of approximately 14 nm. At higher temperatures (600 °C), growing domains become either nanoparticles or pores with a preferential distance of 85 nm. The growth evolution is explained by a general model based on convection and evaporation. With the increase of annealing temperatures, the characteristic lengths parallel to the surface increase due to convection and the perpendicular ones decrease due to evaporation. For the first time, the fundamental reason of columnar growth is found to be the removal of organic species in the underneath layers. Otherwise, the growth is granular. In order to obtain a functional BST thin film capacitor, 1 L type annealing was adopted. It yielded columnar films and a ferroelectric hysteresis loop was obtained. In chapter 5, the effect of solution dilution

on the properties of 1 L BST thin films was investigated. The morphology of the thin films was strongly changed by the increase of dilution through the decrease in surface and columnar roughness. This roughness decrease enables grain coalescence, yielding finally larger grains. Lattice parameters *a* and *c* varied with the increase of dilution causing an expansion in lattice volume. A clear effect was seen on the permittivity of grains and grain boundaries that decreased with dilution. The poling voltage was successfully lowered due to the increase of grain width, contributing in the facilitation of the poling process which is a very promising result. The diluted BST samples exhibit ferroelectric relaxor behavior with increasing P_S and P_r values.
To sum up, the ferroelectricity of the sol-gel BST thin films is definitely linked to the complete removal of organic constituents. In this work, we were able to tailor the nanostructure of thin films at the nanoscale by understanding the underlying physical mechanisms that govern the formation of chemically derived thin films. Columnar grown BST thin films were found to be the most suitable ferroelectric relaxors. Enhanced ferroelectric properties were achieved with the increase of the precursor solution dilution. A decrease in the poling voltage with the increase of the grain width was observed which is extremely attractive for low voltage applications.

BST vs PVDF and composites

Research works on PVDF and inorganic/polymer composites are carried out in our laboratory. The BST thin films investigated in this thesis are found to have promising relaxor ferroelecric properties that could be used for energy recovery applications. Fig. (5.26) shows the different ferroelectric hysteresis loops for BST thin films, PVDF, BTO/PVDF and PZT/PVDF composite thin films. Table (5.7) shows the P_S and P_r values for the ferroelectric materials.

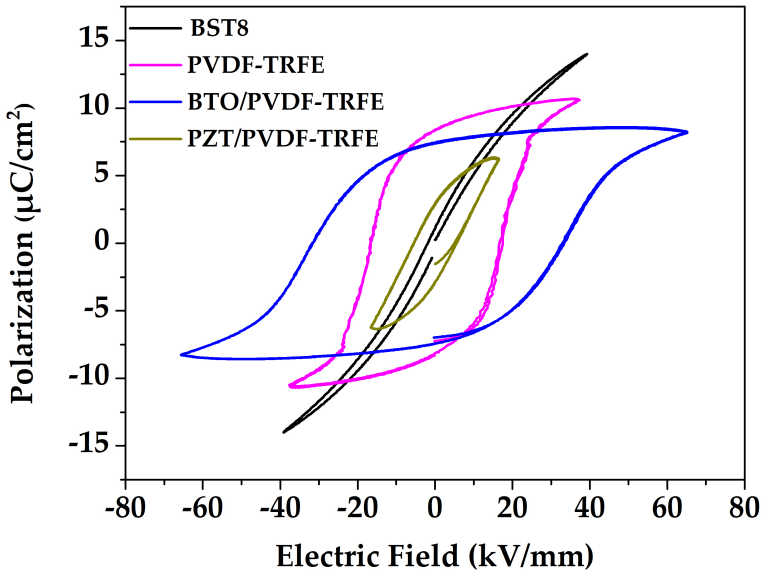

Figure 5.26: Different P-E hysteresis loops for BST and PVDF materials.

Samples	Thickness (μm)	P_S (μC/cm^2)	P_r (μC/cm^2)
BST8	0.25	13.97	1.16
PVDF	4	10.53	8.46
BTO/PVDF	10	8.28	7.44
PZT/PVDF	20	6.15	2.97

Table 5.7: Table representing the P_S and P_r values for BST, PDVF and composites.

Regardless of the thickness difference between the various materials, BST thin films show the highest values of P_S and require lower poling voltages in comparison with PVDF (> 150 V/μm).

Prospects and future work

This section presents the potential future work that could be done on both SBN and BST thin films.

In the present research, SBN carboxylate based precursor solutions were elaborated. Further investigations are needed to complete the path towards better understanding of the chemistry. It has been possible to produce thick layers rich in metal using the carboxylate solutions with an adjustable stoichiometry. In addition, the choice of carboxylate precursors made it possible to avoid the formation of alkaline earth carbonates. In particular, it would be beneficial to investigate the carbonate entities in the system using adapted characterization methods such as ^{13}C Nuclear Magnetic Resonance (^{13}C-NMR). Preliminary X-ray diffraction results show that there is already Nb_xO_y crystallized around SrBaO.
Other possible chemistry paths are open to debate such as using oxime based solvents instead of carboxylic acids in order to limit the carbon content, allowing crystallization at low temperature annealing. Another possibility is to use nanoparticle seeds of niobium, barium or strontium oxide to enhance the crystallization and phase formation at lower temperatures.
In the case of the study on BST thin films, further work on the conduction mechanism origin could be undertaken. For instance, oxygen vacancies is one of the known causes for leakage current in thin films such as BST. For that matter, *I-V* measurements as a function of temperature and time could be conducted and could bring valuable insights about the origin and the nature of conduction in BST thin films.
In addition, advanced ferroelectric measurements could be beneficial to assess the energy storage capacities of BST thin films. In recent years, efforts to develop renewable energy sources have been inspired by the evolution of the economy, climate change and air pollution. This led to a higher demand for energy-storage systems such as dielectric capacitors. Novel lead-free materials have been recently investigated for their good energy-storage properties [1]. Below is a preliminary study on the energy storage properties of the diluted samples of BST thin films discussed in chapter 5.
The *P-E* loop can be used to calculate the energy-storage capacities. The recoverable energy density *W* corresponds to the area above the hysteresis loop i.e. the integral of the area comprised between the discharge curve and the y-axis, noted (I) in the inset of Fig. (5.27). The energy-loss density W_{loss} corresponds to the area inside the hysteresis loop i.e. the integral of the area comprised between the charge and discharge curves, noted (II) in the inset of Fig.(5.27). The energy-storage efficiency is $R=W/(W+ W_{loss})$ [2].

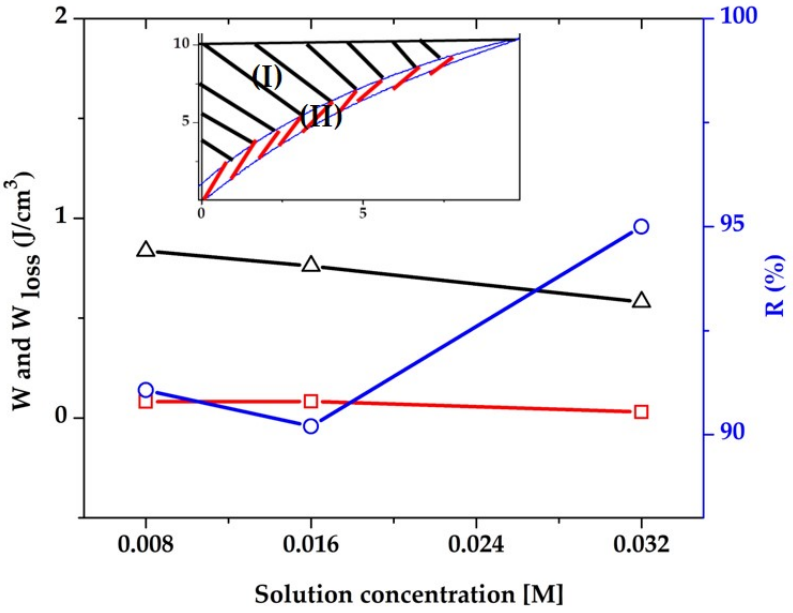

Figure 5.27: Recoverable energy density W (black line), energy loss W_{loss} (blue line) and energy storage efficiency R (red line) plotted as a function of the precursor solution concentration. The inset shows the shaded areas of the hysteresis loop used in the calculation of the energy densities.

The calculated data for the energy-storage are plotted in Fig. (5.27). BST8 exhibits the largest energy-storage density (W = 0.84 J/cm^3) in comparison to the other samples and good efficiency (R = 95.4 %).

Flexible electronics are in full development and arouse a strong interest for many applications including energy recovery and fingerprint sensors. It is necessary to lower the annealing temperature of the metal oxide thin films in order to work with flexible substrates. Bretos et al. show that the solution chemistry can be tailored for designing the desired molecular precursors through wet chemical methods. They also show that light can be used as an alternative energy source to induce crystallization of metal oxide thin films by photochemistry. The lowering of the crystallization temperature allows the integration of metal oxides in electronic devices especially flexible systems [3].

Moreover, pyroelectric measurements are considered in the future work on the BST thin film capacitors. The pyroelectric current can be detected by measuring the current variation with temperature.

References

[1] Zou, K., Dan, Y., Xu, H., Zhang, Q., Lu, Y., Huang, H., and He, Y. *Materials Research Bulletin* **113**, 190–201 (2019).

[2] Sun, J., Yang, C., Song, J., Zhou, Y., Yao, Q., and Sun, X. *Ceramics International* **43**(2), 2033–2038 (2017).

[3] Bretos, I., Jiménez, R., Ricote, J., and Calzada, M. L. *Chemical Society Reviews* **47**(2), 291–308 (2018).

Appendices

Appendix A

Clean room equipments and materials

A.1 Spin coater

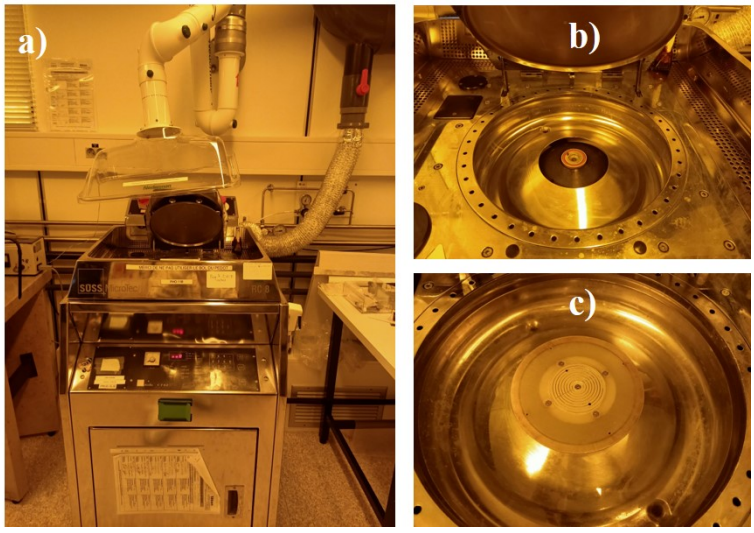

Figure A.1: Spin coater scheme showing (a) the full spin coating equipment under ventilation, (b-c) a close-up on the spin coater vacuum with and without a chuck.

The spin coater used for the solution deposition is a RC 8 model from SUSS MicroTec, Fig.A.1 (a) shows the entire equipment with the extraction system located in the clean room. Figs.A.1 (b-c) focuses on the spin vacuum chuck area of the machine.

A.2 Hot plate

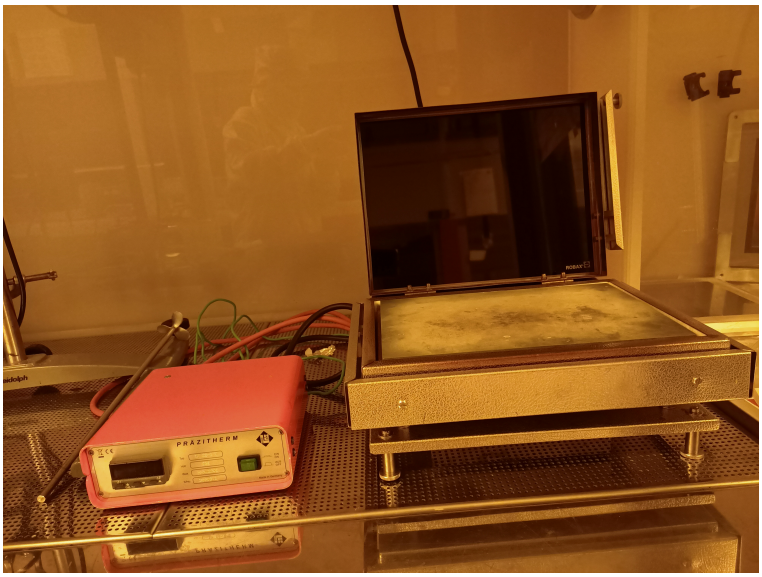

Figure A.2: Hot plate used for the pre-annealing of the thin films placed on a bench under a hood in the clean room.

A.3 Platinized silicon wafers

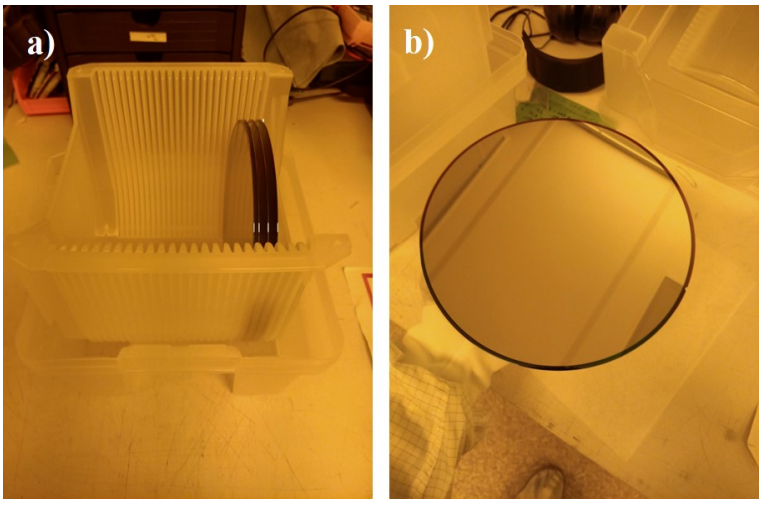

Figure A.3: (a) silicon wafers in their box, (b) a platinized silicon wafer

Appendix B

Electrical characterization setup

B.1 LCR meter

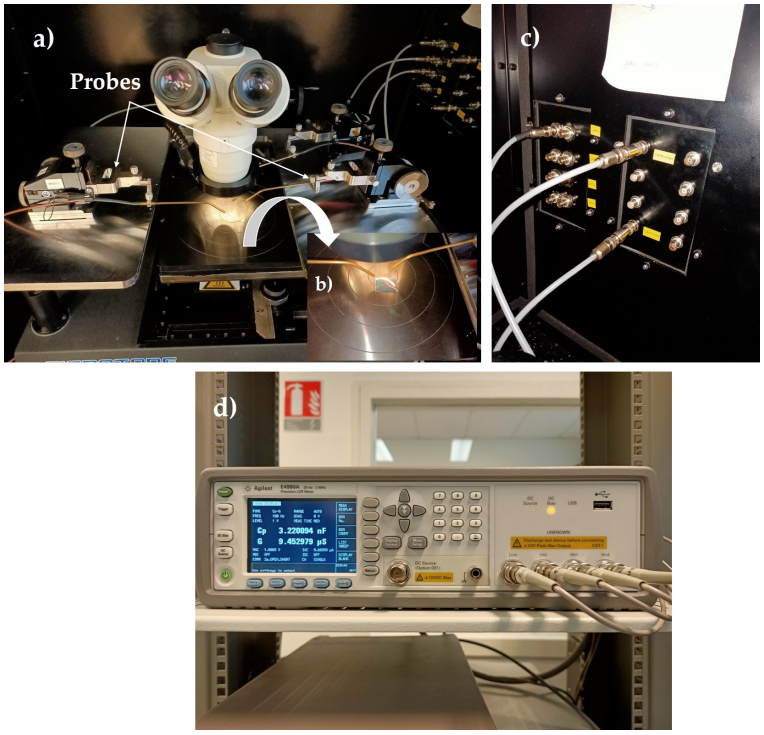

Figure B.1: Image showing :(a) The setup for the dielectric measurements with the probing system and the microscope, (b) a close-up on the sample holder and the probes, (c) a close-up on the coaxial cables and (d) the LCR meter.

B.2 Setup for the hysteresis loop measurements

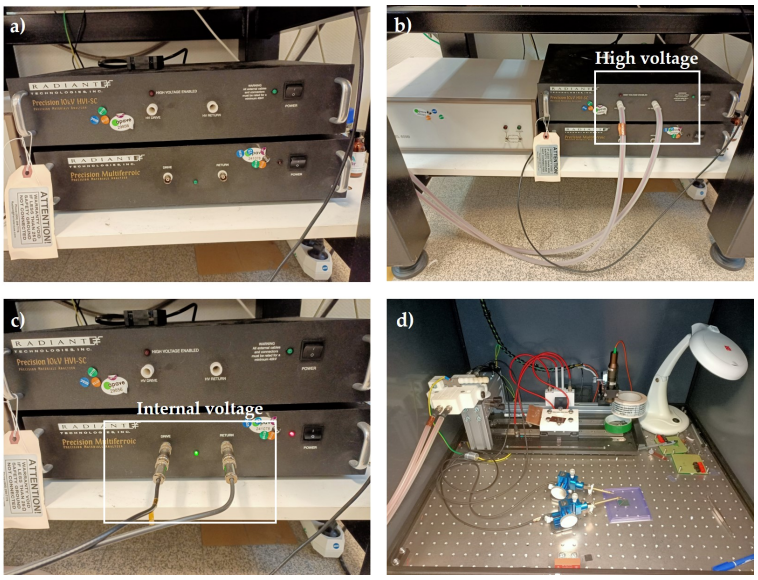

Figure B.2: Images of the ferroelectric measurements setup:(a) Precision 10 kV HVI-SC from Radiant Technologies , (b) External high voltage probe connectors, (c) Internal low voltage probe connectors and (d) characterization test bench with two probes set on the sample.

Vision software was used to perform the different polarization measurements on the ferroelectric thin film capacitors.

Appendix C

GISAXS equipment

C.1 GISAXS setup

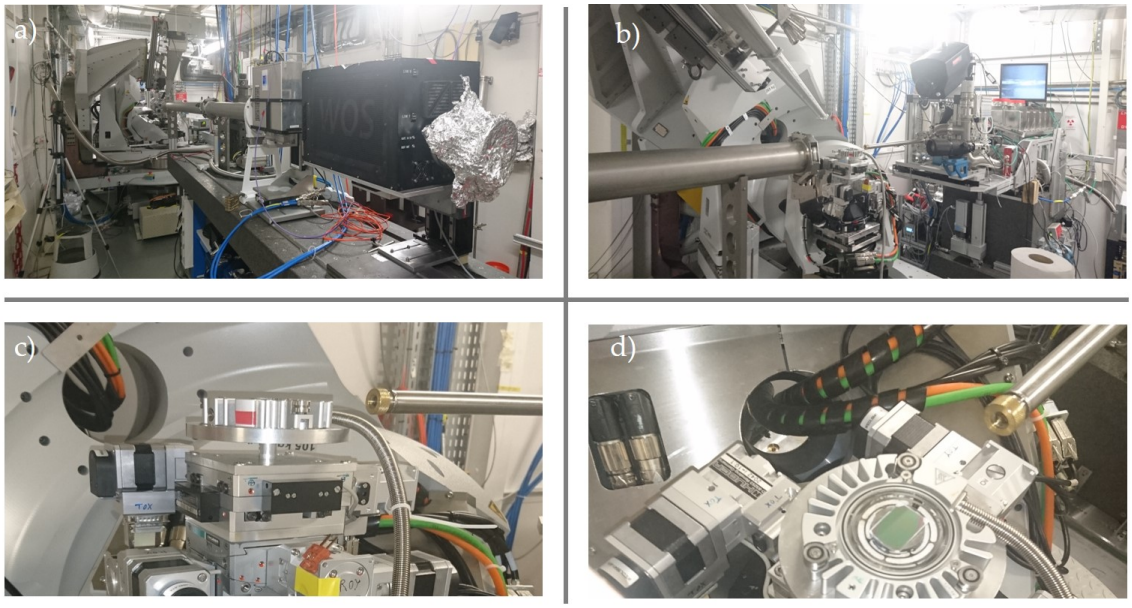

Figure C.1: GISAXS setup images : (a) Overview on the whole setup, (b) detectors and cameras, (c) close-up on the sample holder and (d) close-up on the sample.

C.2 Anton Paar

Figure C.2: Anton Paar furnace used for heating up to 200°C in the *in situ* GISAXS measurements.